Expanding The Capabilities of Sum-frequency Generation Vibrational Spectroscopy

by

Kyle Vine

B.Sc., Simon Fraser University, 2018

Thesis Submitted in Partial Fulfillment of the
Requirements for the Degree of
Master of Science

in the
Department of Chemistry
Faculty of Science

SIMON FRASER UNIVERSITY
Fall 2022

Declaration of Committee

Name:	**Kyle Vine**
Degree:	**Master of Science (Chemistry)**
Title:	**Expanding The Capabilities of Sum-frequency Generation Vibrational Spectroscopy**
Committee:	**Chair: Corina Andreoiu** Professor, Chemistry
	Krzysztof Starosta Supervisor Professor, Chemistry
	Jeffrey Warren Committee Member Associate Professor, Chemistry
	Loren Kaake Committee Member Associate Professor, Chemistry
	Byron Gates Examiner Professor, Chemistry

Abstract

Sum-frequency generation vibrational spectroscopy (SFG-VS) is a nonlinear optical spectroscopy used to probe the vibrations of molecules at interfaces. SFG-VS can be applied to study a vast number of interfacial systems to gain information which could not be obtained through other means. Methods of acquiring phase-sensitive sum-frequency generation (PS-SFG) and two-dimensional sum-frequency generation (2D SFG) measurements were developed for use in SFU Chemistry.

PS-SFG measurements were enabled through phase-shifting interferometry, allowing for the extraction of complex PS-SFG spectra revealing the orientations of molecular groups at interfaces. Phase-shifting was accomplished by rotating dispersive optics in the beam path of a secondary SFG source used to interfere with the SFG of the sample.

2D SFG measurements were enabled through the use of a novel implementation of the Michelson interferometer. A custom motion controller was designed and implemented for precise control over the interferometer arm lengths. A calibration procedure was developed for the interferometer which uses spectral interferometry. The ability of the interferometer to produce a 2D SFG spectrum is demonstrated with reference measurements. The ability to produce a 2D SFG spectrum of a vibrationally-resonant sample was not demonstrated due to insufficient laser power.

Keywords: Phase-sensitive sum-frequency vibrational spectroscopy; Phase-shifting interferometry; Two-dimensional sum-frequency generation vibrational spectroscopy

Table of Contents

List of Figures

List of Tables

List of Acronyms

CAD	Computer-aided Design
DAC	Digital-to-analog Converter
DFT	Density functional theory
EDA	Electronic Design Automation
FFT	Fast Fourier Transform
FPGA	Field Programmable Gate Array
IFFT	Inverse Fast Fourier Transform
IR	Infrared
LO	Local Oscillator
MDK	Microcontroller Development Kit
OPA	Optical Parametric Amplifier/Amplification
PS-SFG	Phase-sensitive Sum-frequency Generation
PSU	Phase-shifting Unit
SFG	Sum-frequency Generation
SFG-VS	Sum-frequency Generation Vibrational Spectroscopy
SFU	Simon Fraser University
TR-SFG	Time-resolved Sum-frequency Generation
UV-Vis	Ultraviolet-visible
VIS	Visible

1 Introduction

1.1 Sum-frequency Generation Vibrational Spectroscopy (SFG-VS)

Sum-frequency generation vibrational spectroscopy (SFG-VS) is a nonlinear optical spectroscopy used to probe the vibrations of molecules at interfaces. Sum-frequency generation is second-order nonlinear optical process, which can only occur in non-centrosymmetric media such as interfaces. Sum-frequency generation can be resonantly enhanced by vibrational modes as illustrated in Figure 1.1.[1–3] This property allows for the collection of a vibrational spectrum of an interface without contributions from a centrosymmetric bulk. SFG-VS can be applied to study a vast number of interfacial systems to gain information which could not be obtained through other means. Numerous examples exist in literature.[4–6]

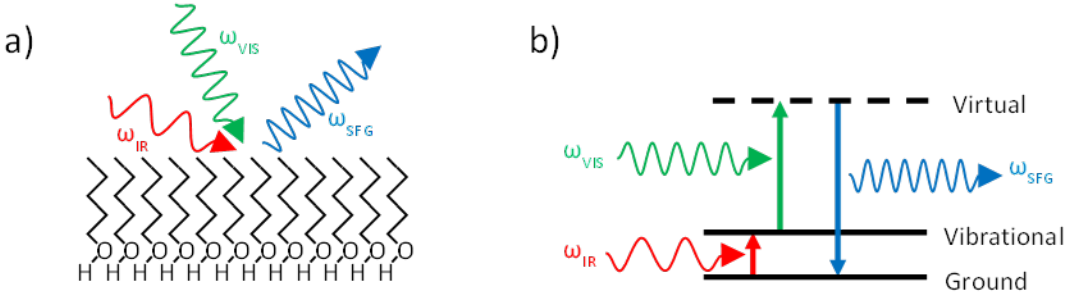

Figure 1.1. a) Illustration of IR and visible (VIS) fields incident on monolayer of 1-pentanol producing a reflected SFG field. b) Corresponding energy level diagram for vibrationally-enhanced SFG when ω_{IR} matches the resonant frequency of a vibrational mode. The SFG field satisfies the condition $\omega_{SFG} = \omega_{IR} + \omega_{VIS}$. Additional information about SFG can be found in Appendix C.

The intensity of the SFG field $I_{SFG}(\omega_{IR} + \omega_{VIS})$ is proportional to the intensities $I_{IR}(\omega_{IR})$ and $I_{VIS}(\omega_{VIS})$ of the IR and visible light incident on a sample:

$$I_{SFG}(\omega_{IR} + \omega_{VIS}) \propto \left|\chi^{(2)}(\omega_{IR}, \omega_{VIS})\right|^2 I_{IR}(\omega_{IR})\, I_{VIS}(\omega_{VIS}) \;, \qquad (1.1)$$

where $\chi^{(2)}(\omega_{IR}, \omega_{VIS})$ is the second-order non-linear susceptibility, while ω_{IR} and ω_{VIS} are the frequencies of the IR and visible light respectively.

Although SFG-VS does not suffer from the background signal of the bulk, it is still difficult to detect signal from the relatively small number of molecules at the interface compared to the bulk. It requires the use of ultrafast laser pulses to provide sufficient field strength of visible and IR light simultaneously to produce enough SFG to be detected.

Previous research at SFU Chemistry has demonstrated the ability of SFG-VS to probe single monolayers of Langmuir-Blodgett films of cadmium stearate.[7,8] The SFG produced depends on both the ordering and orientation of molecules at an interface. By applying different combinations of polarization for the visible and IR fields, the orientation of molecules can be determined based on the intensity of the resulting SFG.[7]

The use of ultrashort laser pulses enables for broadband IR fields that are capable of producing resonantly-enhanced SFG over multiple vibrational modes. This is desirable because the narrowband resonant peaks can be resolved on a UV-Vis spectrometer when paired with a narrowband VIS field. As illustrated in Figure 1.2, the resolution of the underlying resonant IR peaks in the SFG spectrum is determined by the bandwidth of visible light used.

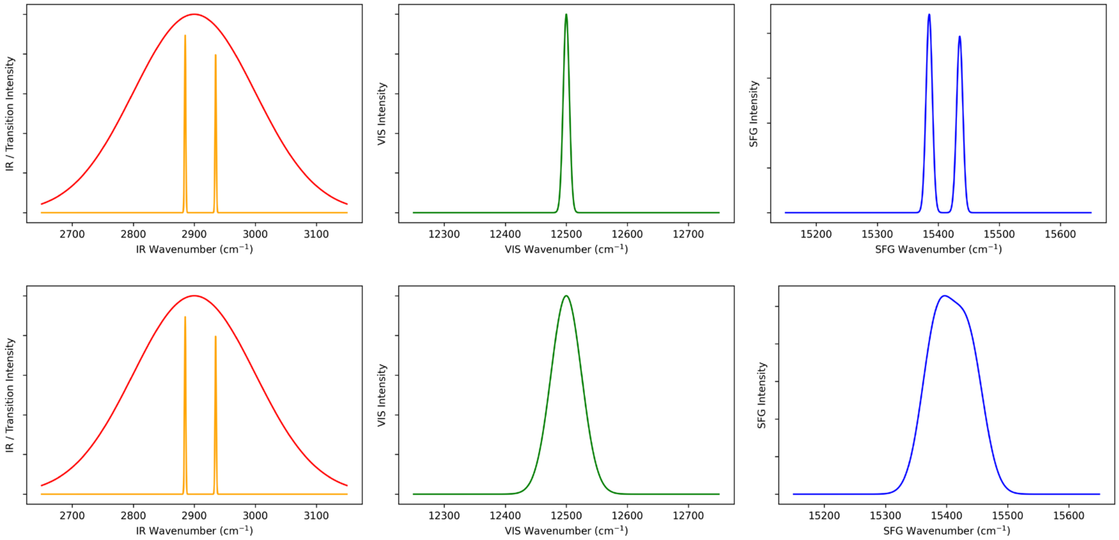

Figure 1.2. Comparison of the SFG spectrum produced from a broadband VIS field (top) and narrowband VIS field (bottom) when the signal is resonantly enhanced at narrowband IR transitions. The IR transition and excitation intensities are plotted in red and orange respectively.

1.2 Phase-sensitive SFG (PS-SFG)

Phase-sensitive SFG (PS-SFG) provides a means of determining the orientation of molecules at a surface. PS-SFG spectra contain both the phase and amplitude of the sample signal, rather than just the intensity which is collected in typical SFG measurements. It is convenient to plot PS-SFG spectra in terms of the real and imaginary components of the complex field amplitude of the sample signal as they can be plotted together with the same units on the y-axis. The complex field amplitude E_{SFG} satisfies the proportionality:

$$E_{SFG}(\omega_{IR} + \omega_{VIS}) \propto \chi^{(2)}(\omega_{IR}, \omega_{VIS})E_{IR}(\omega_{IR})\, E_{VIS}(\omega_{VIS}) \,, \qquad (1.2)$$

where $\chi^{(2)}(\omega_{IR}, \omega_{VIS})$ is the complex-valued second-order non-linear susceptibility, while $E_{IR}(\omega_{IR})$ and $E_{VIS}(\omega_{VIS})$ are the complex field amplitudes of frequencies ω_{IR} and ω_{VIS} of the IR and visible light respectively, carrying the amplitudes and phases of the individual light pulses. PS-SFG reveals the magnitude and phase of $\chi^{(2)}$, which can be used to determine the orientation of molecules at a surface, as opposed to typical SFG measurements which only reveal the magnitude.[9] Figure 1.3 shows a comparison between the information that is expected from typical SFG measurements and PS-SFG measurements.

Generally, the signal that comes from the resonant enhancement of vibrational modes has a signal that is 90 degrees out of phase with respect to the non-resonant signal.[10] This phase shift can be attributed to adsorption of the IR light. Molecular groups that are oriented towards the interface generate signal that is 180 degrees out of phase as compared to the case of molecular groups that are oriented away from the interface. This can be attributed to the sign the second-order nonlinear response of the groups being orientation-dependent, which is desirable in the determination of the orientation of molecules at an interface.

While there are different methods for obtaining HD-SFG spectra, they are all inherently interferometric. This involves generating a second source of SFG, called the local oscillator (LO), which interferes with the sample. The total intensity I_{total} of the two sources combined at a given SFG wavelength can be described in terms of the individual complex field amplitudes E_{LO} and E_{Sample}, and the difference in phase between them $\Delta\varphi$ by,

$$I_{total} = \left|E_{LO} + E_{Sample}\right|^2 = |E_{LO}|^2 + \left|E_{Sample}\right|^2 + 2|E_{LO}|\left|E_{Sample}\right| \cos\Delta\varphi . \quad (1.3)$$

The total intensity can be divided into a phase-independent term I_{PI} and phase-dependent term I_{PD} given by

$$I_{PI} = |E_{LO}|^2 + \left|E_{Sample}\right|^2 , \quad (1.4)$$

$$I_{PD} = 2|E_{LO}|\left|E_{Sample}\right| \cos\Delta\varphi . \quad (1.5)$$

The phase of the sample signal with respect to the LO signal is somewhat arbitrary; it has significant contributions from the dispersion of air and other optics. It does not provide useful information on its own. A reference must be used at the same place as the sample in order to find the phase shift specific to the particular experimental arrangement, allowing for the extraction of the absolute phase of the sample with respect to the reference. Gallium arsenide has been chosen as a reference for the HD-SFG implementation presented in this thesis, as it produces a strong SFG signal that is non-resonant with the frequency of IR light used, which should not produce a phase shift from the sample absorbing the IR light.

Various methodologies exist for extracting the phase and amplitude from SFG intensity measurements, all of which fall into two categories: spectral-interferometric and phase-shifting. The spectral-interferometric type involves imparting a systematic phase shift across frequencies within the same measurement, while the phase-shifting type involves imparting a systematic phase shift between different measurements irrespective of the phase between frequencies. Only the phase-shifting type will be described in detail in this section, as it is the type that was implemented in this thesis. A detailed description of the spectral-interferometric type is given in Appendix A.

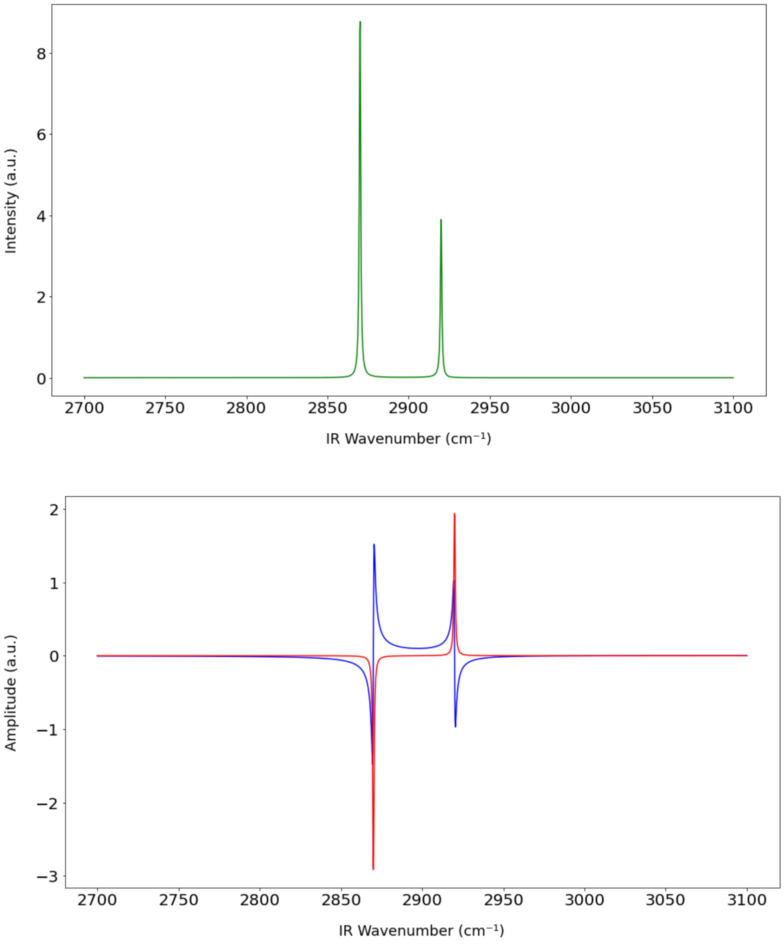

Figure 1.3. Example of a broadband SFG-VS intensity spectrum (top). Example of a PS-SFG spectrum with real and imaginary components of the complex field amplitude plotted in blue and red respectively (bottom). Both spectra are produced from the same simulated data. The two peaks are simulated with $\chi^{(2)}$ of opposite sign, which might be expected of two modes pointed in opposite directions. $\chi^{(2)}$ is entirely imaginary at the center frequencies due to the 90-degree phase shift caused by the absorption of the IR light. The peaks were simulated with a Lorentzian lineshape, resulting in the real component of each peak having opposite signs about their centers. The PS-SFG spectrum would be the result of using the local oscillator to extract the phase of the sample signal relative to the phase of a reference signal produced from a reference placed in the same position as the sample. The resulting spectrum should not be heavily influenced by the particular implementation of LO used.

Phase-shifting PS-SFG involves imparting a systematic phase shift between measurements irrespective of the phase between frequencies, which can be accomplished using a phase-shifting unit (PSU) placed between the sample and LO. The implementation of the PSU presented in this thesis is described in Chapter 2. A diagram of a typical spectral-interferometric PS-SFG setup is shown in Figure 1.4.

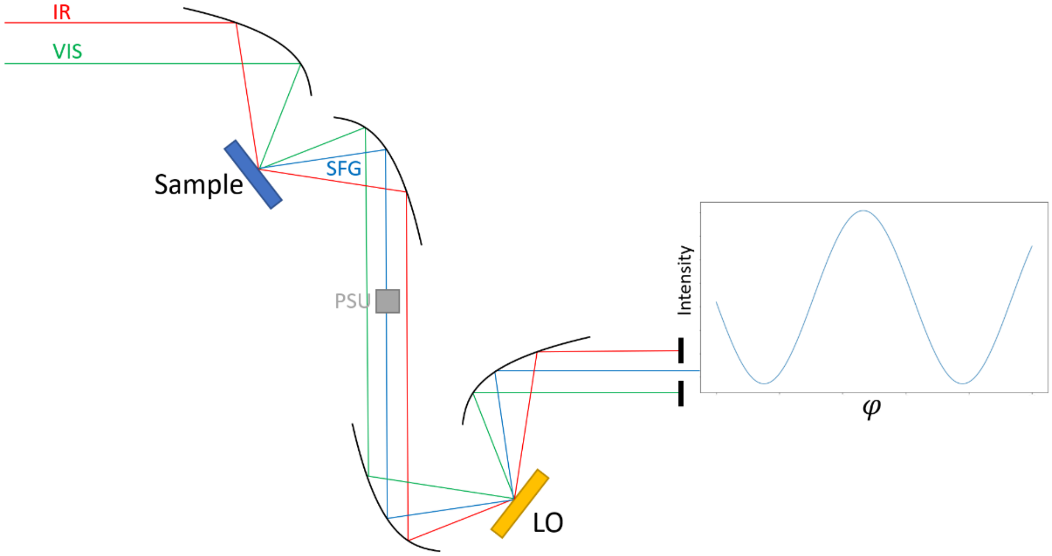

Figure 1.4. Diagram of a typical phase-shifting PS-SFG setup. IR and VIS beams are focused on the sample by a parabolic mirror to produce SFG which is then collimated (along with the IR and VIS beams) by a second parabolic mirror. A variable phase shift is added to the SFG produced by the sample by phase-shifting unit PSU. All beams are then focused onto the LO to produce a second source of SFG which interferes with the SFG produced from the sample, producing an intensity that is a function of PSU phase shift φ. The intensity is captured at all SFG frequencies simultaneously on a UV-Vis spectrometer. The value of φ is specific to the individual SFG frequencies.

In contrast to the complicated signal extraction method used with spectral-interferometric measurements, described Appendix A, the complex amplitude of the sample signal E_{Sample} can be determined at each SFG frequency independently. For a given SFG frequency, the intensity as a function of phase shift φ can be given by

$$I(\varphi) = \left|E_{LO} + E_{Sample}\, e^{i\varphi}\right|^2, \tag{1.6}$$

where E_{LO} is the amplitude of the LO signal made to be real and positive.

The intensity only needs to be measures with 3 values of φ to determine the three unknowns: E_{LO}, $Re(E_{Sample})$ and $Im(E_{Sample})$; however, in practice it best to take more measurements so that the unknowns are over-determined and can be fit to data, ensuring that the change in intensity is due to a phase shift and not fluctuations in laser intensity between measurements. Figure 1.5 illustrates how the intensity could be fit to 4 points.

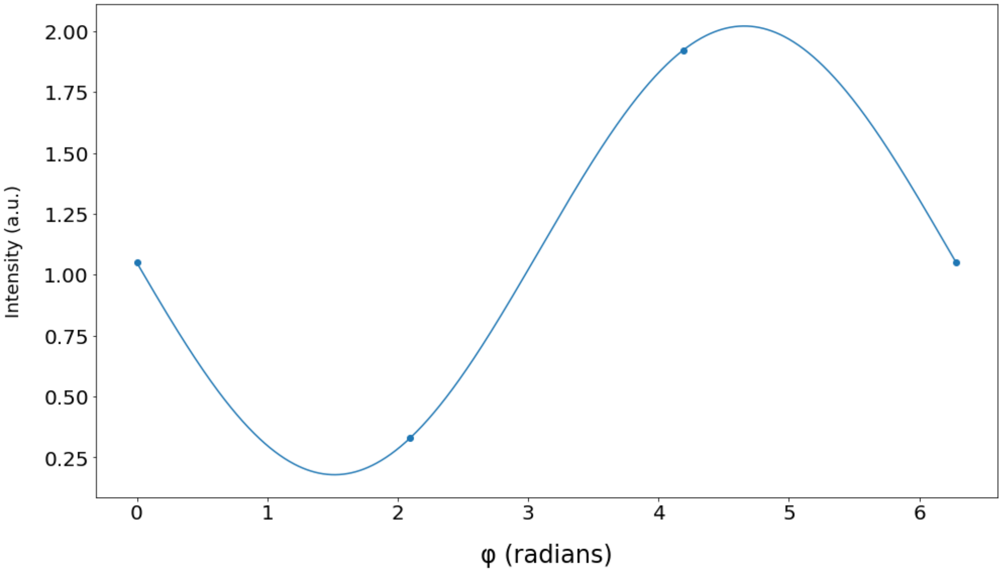

Figure 1.5. Theoretical SFG intensity at some wavelength as a function of PSU phase shift φ. The theoretical measured points are plotted with circles and the corresponding fit is plotted with a line. The ability to fit more than 3 data points is an indication of self-consistency.

Because the complex amplitude of the sample signal is extracted at each SFG frequency independently, the resolution of phase-shifting measurements matches the resolution of the UV-Vis spectrometer used to take them, in contrast to spectral-interferometric measurements. Phase-shifting measurements also do not suffer from the measurement error of spectral-interferometric measurements discussed in Appendix A. The only drawbacks to phase-shifting measurements are an increased acquisition time (due to taking multiple measurements) and the measurement error caused by variations in laser intensity between measurements. By taking a large number of redundant measurements with different phase shifts, the laser intensity fluctuations can be averaged out by fitting all of the measurements.

1.3 Two-dimensional SFG (2D SFG)

1.3.1 One-dimensional Pump-probe SFG

Two-dimensional SFG (2D SFG) is a form of pump-probe SFG. Before introducing 2D SFG, one-dimensional pump-probe SFG will be introduced. Pump-probe SFG can be viewed as an analogue to transient absorption measurements[♦], except that SFG spectra are taken in place of UV-Vis absorption spectra. A diagram of the pulses involved in a typical pump-probe SFG measurement is shown in Figure 1.6.

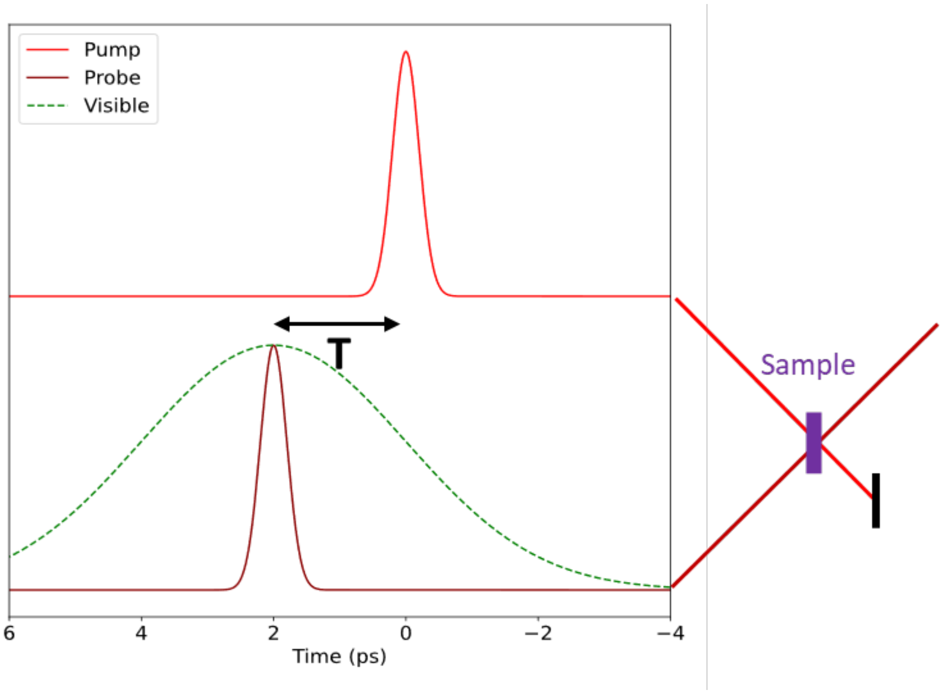

Figure 1.6. Diagram of the pulses involved in a pump-probe SFG measurement. Only the SFG produced from the probe in analyzed; the signal from the pump is blocked after being exposed to the sample. Focusing optics are not shown. The y-axis of the plot is field amplitude, which is not shown due to the y-offset used to depict spatial separation between pulses.

The principle of pump-probe measurements is that the pump pulse induces some change in the sample, such as a vibrational or electronic excitation, which can be observed as a change in the SFG probe signal. The change can be observed as a function of pump-probe time delay T to study how the excitation decays in time, which falls under the

---

[♦] Transient absorption spectroscopy is a technique used to measure excited-state absorption energies and lifetimes in molecules.

category of time-resolved SFG (TR-SFG). Various examples exist in literature where the pump pulse is in the visible spectrum and electronically excites the sample; however, the pump-probe measurements discussed in this thesis exclusively use a pump pulse in the IR spectrum, which vibrationally excites the sample. An energy level diagram showing the states involved in these measurements given a single vibrational mode is shown in Figure 1.7.

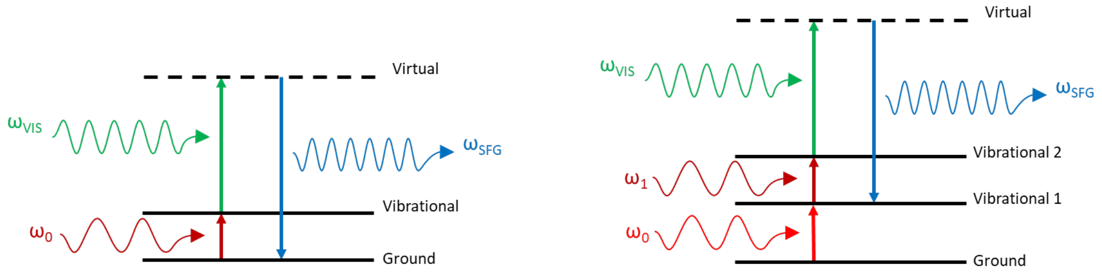

Figure 1.7. Energy level diagram of the states involved in a typical 1D SFG measurement (left). Energy level diagram of the states involved in a typical pump-probe SFG measurement (right). The reduced spacing between the first and second vibrationally excited state can be attributed to the anharmonicity of the underlying mode.

The effect of the pump pulse on the SFG probe can be seen by subtracting the SFG probe spectrum with the pumped blocked from the SFG probe spectrum after the sample is exposed to the pump pulse. The resulting ΔSFG spectrum should have a negative peak at the ground-state excitation frequency ω_0, known as the ground-state bleach, and a positive peak at the lower excited-state excitation frequency ω_1 corresponding to molecules being transferred to the exited state by the pump pulse. The ΔSFG spectrum corresponding to Figure 1.7 is illustrated in Figure 1.8 (bottom).

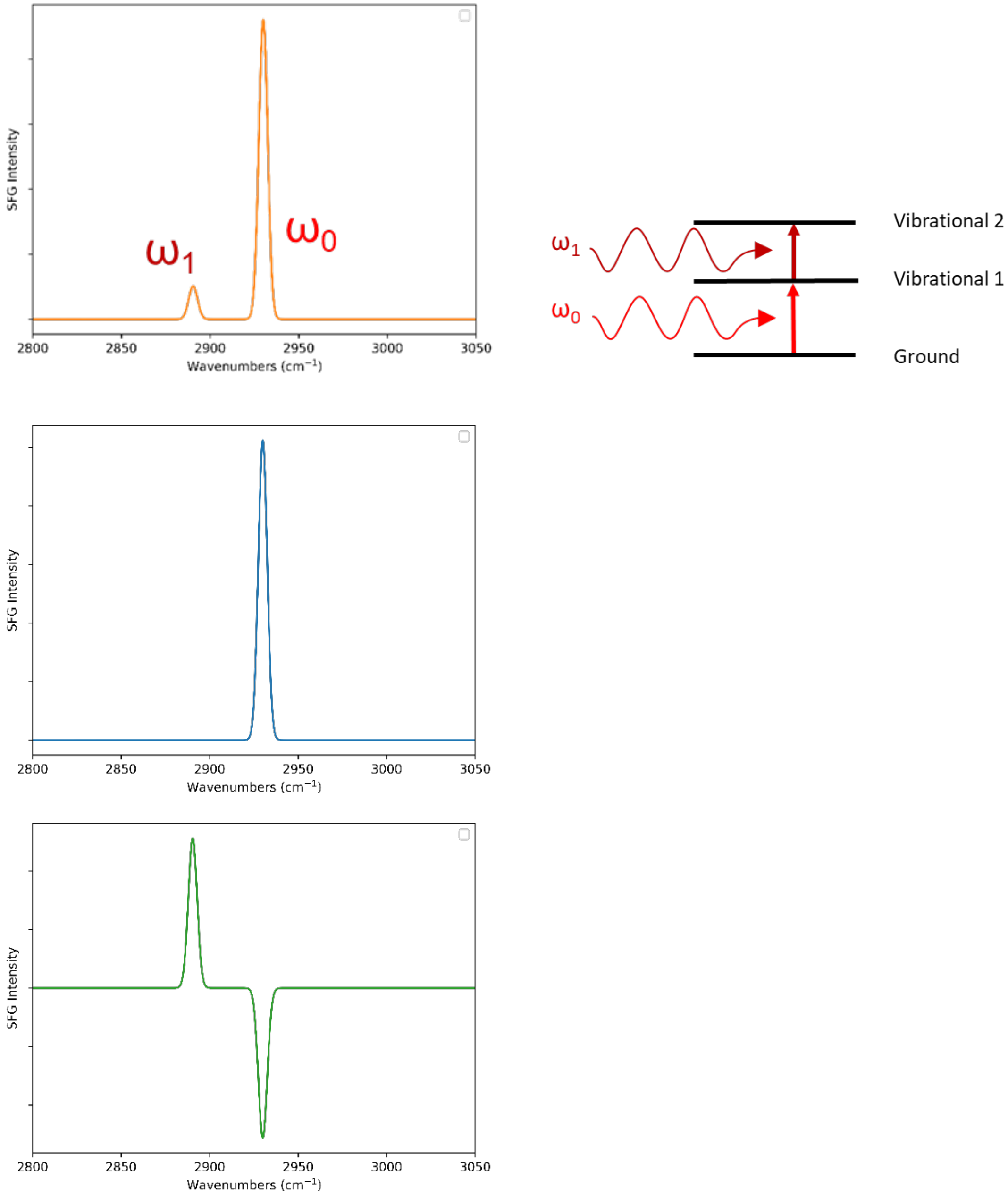

Figure 1.8. SFG spectrum of sample after being exposed to pump pulse (top-left), with associated energy levels (top-right). SFG spectrum of sample without being exposed to pump pulse (middle). Difference between SFG spectra with pump pulse exposed and not exposed (bottom), which is attributed to the population of molecules that are transferred to the excited state by the pump pulse.

By observing the ΔSFG spectrum of the probe at different pump-probe time delays, the lifetime of the vibrationally excited state can be determined. This is illustrated in Figure 1.9.

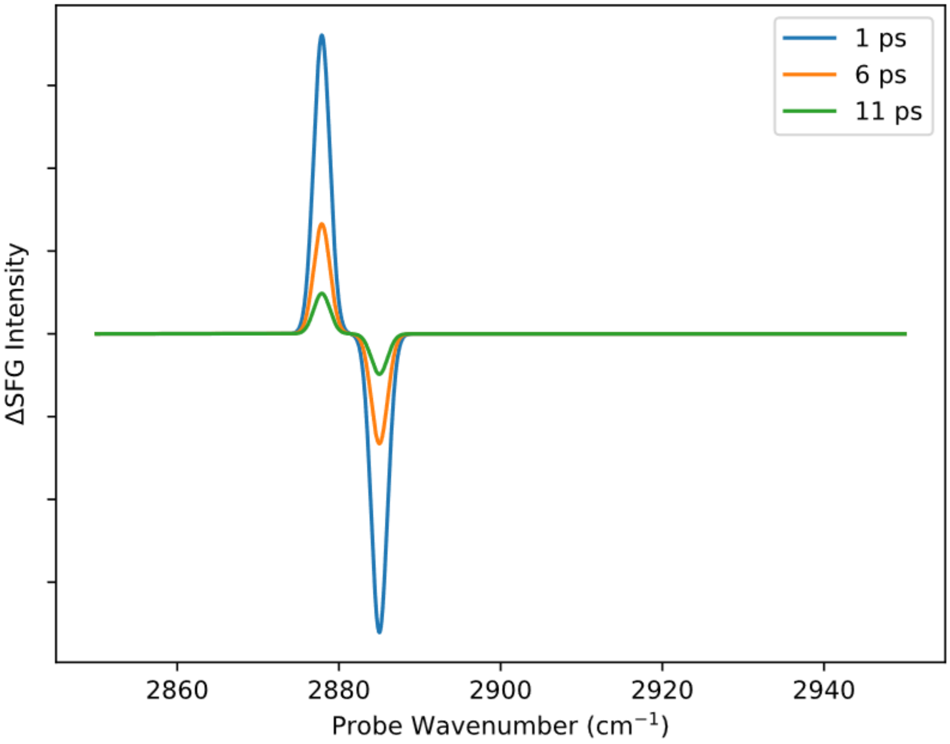

Figure 1.9. Simulated ΔSFG spectra at various pump-probe time delays. The decay of the peaks corresponds to molecules relaxing back to the ground state from the excited state (“Vibrational 1” in Figure 1.7). The simulation was performed using a typical CH3 stretching frequency and anharmonic shift, as well as an exponential decay with a time constant corresponding to the expected typical lifetime of a CH3 stretching excitation.

The figure above was made to illustrate the simple case where the pump pulse excites one vibrational mode and the probe pulse shows changes in the spectrum of the same mode. The next figure illustrates what would be expected if the pump pulse excites two vibrational modes and the probe pulse shows changes in the spectrum of both modes.

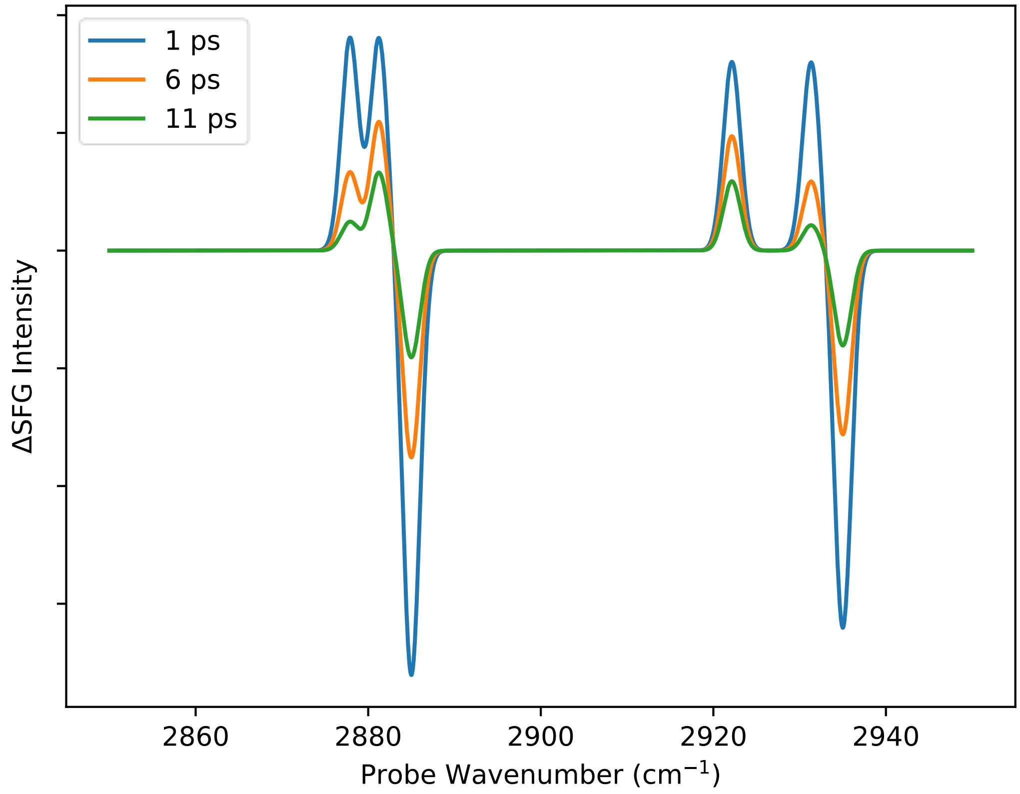

Figure 1.10. Simulated ΔSFG spectra with two vibrational modes being excited from the pump pulse and two modes being probed at various pump-probe time delays. There is ambiguity in which vibrational mode being excited by the pump is responsible for each positive peak. The excited states of each mode have different decay rates. The excited states correspond to real vibrationally-excited states in the molecules and are expected to have much longer lifetimes than the virtual state shown in Figure 1.7.

Exciting one vibrational mode can lower the frequency required to excite other modes. This is known as anharmonic coupling. The amount of coupling is specific to the combination of modes. This is illustrated in Figure 1.10, where two positive peaks are seen for each negative peak, indicating that two modes are being excited, each with their own anharmonic shift. This presents some ambiguity in interpreting the spectrum, as there is no way of determining which mode is responsible for each shift. The figures above were just for illustration; in practice the broadband pump pulse is capable of exciting several vibrational modes, which furthers the ambiguity in interpreting the spectrum.

1.3.2 Two-dimensional Measurements

The previous subsection was meant to motivate the need for 2D SFG-VS, which is a form of pump-probe SFG where the pump wavenumbers are spectrally resolved along another axis, revealing which pump excitation frequencies are responsible for changes in the probe spectrum. The type of data expected from 2D SFG-VS is illustrated in Figure 1.11.

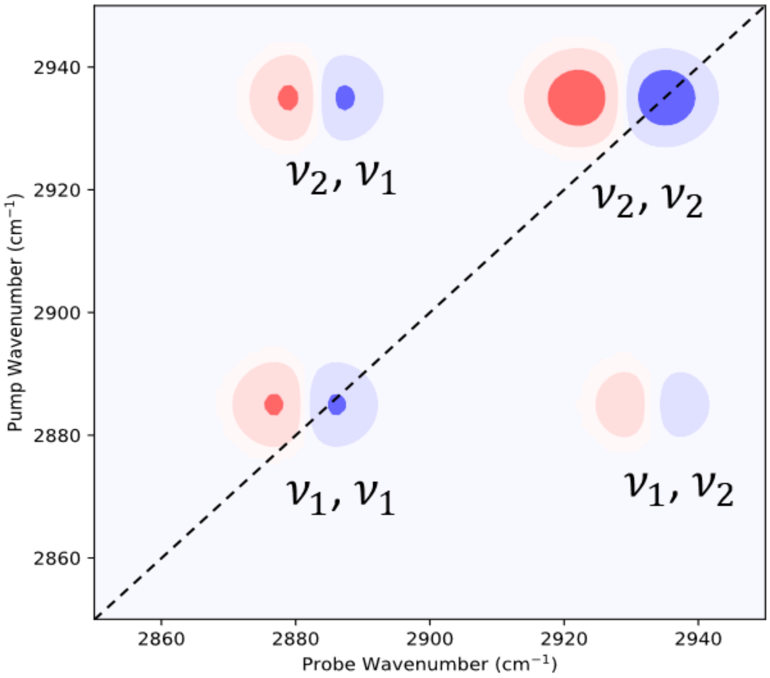

Figure 1.11. Simulated 2D SFG-VS spectrum with two vibrational modes v_1 and v_2 being excited from the pump pulse and the same modes being probed. The first mode in the peak-pair labels corresponds to the mode being pumped, while the other corresponds to the mode being probed.

The ability to resolve pump wavenumbers enables for the decay mechanisms of each vibrational mode to be studied more closely when the spectrum is time-resolved over the pump-probe delay. Although Figure 1.12 illustrates simple exponential decay of the vibrational excited population of molecules, other time-dependent phenomena could potentially be observed with these measurements.

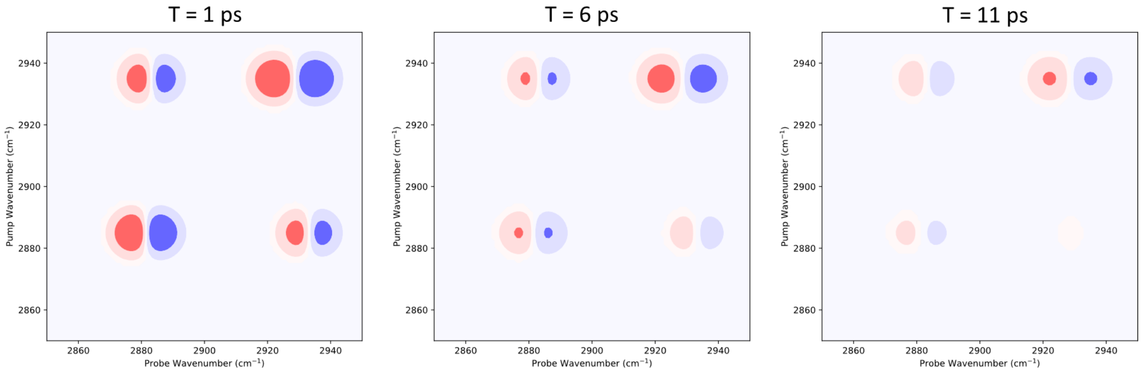

Figure 1.12. Simulated time-resolved 2D SFG-VS spectrum of the same vibrational modes featured in Figure 1.11. The two modes exhibit exponential decay with different lifetimes.

Just as with 2D IR spectroscopy, 2D SFG-VS probes molecules after being excited with a different vibrationally-resonant pump frequencies, but with the added ability to probe monolayer-thin samples at interfaces.[11] The technique can be applied to a vast amount of interfacial systems ranging from biological interfaces to CO_2 reduction catalysts.[12,13] However, it poses many experimental challenges; only a few groups in the world have demonstrated the ability to acquire 2D SFG spectra. Some of these challenges include precise control over the timing of the laser pulses involved, analysis of the data to produce 2D spectra that are readily interpretable and sample preparation

Bonn et al used it to study the vibrational coupling of water molecules at the air/H_2O interface.[14] They were not able to resolve separate peaks due to the broadness in the IR absorption of water. Instead, they analyze how the populations within a single peak change after being excited by different frequencies of an IR pump pulse. They observe a shift in the frequency the SFG peak at different time delays. This shift is attributed to spectral diffusion. By comparing the observed spectral diffusion timescale to that obtained from bulk-phase 2D IR spectroscopy of H_2O in literature, they found that there is more inhomogeneity at the air/H_2O interface compared to the bulk. Tahara et al did a similar study on HOD-D2O at a charged interface.[15] They found that there was not a significant difference in the spectral diffusion timescales of the interfacial 2D SFG signal compared to bulk-phase 2D IR signal, which suggests there may be some fundamental difference between the two cases.

Peterson et al used it to study the structure of a CO_2 reduction catalyst on nanostructured TiO_2 to better understand the binding geometry and energy redistribution of the catalyst on the TiO_2 nanostructures.[13] They demonstrate their ability to obtain a 2D SFG spectrum and suggest the information that could be extracted, but there still remains challenges in the interpretation of the data.

Zanni et al used 2D SFG-VS to study DNA and peptides at interfaces.[12,16] They attempted to demonstrate agreement between their experimental spectra and spectra that were simulated using DFT. While it is unclear from the publication how one could use the simulations to interpret the experimental spectra if the structures were not already known, the simulations do show that the group has made some progress towards understanding the structural dependence of the 2D SFG signal and provides some insights to build a model that could be used to interpret 2D SFG spectra in the future, and possibly elucidate interfacial structures.

The Zanni Group has other publications about 2D SFG,[17–19] most of which are primarily focused on the theory behind 2D SFG. There is no shortage of useful references for understanding 2D SFG; many include textbooks explaining the theory behind vibrational Raman, IR and 2D IR spectroscopy; which summarize a vast amount of literature and present concepts that can be applied to 2D SFG spectroscopy. There are also references for more advanced theories such as those used in the anharmonic DFT calculations in Gaussian 16,[20,21] none of which actually mention SFG. These calculations have been shown to accurately predict IR and vibrational Raman spectra and may be key to predict 2D SFG spectra with enough accuracy to be useful in interpreting experimental results.

1.4 Thesis Overview

In effort to expand the capabilities of SFG-VS at SFU Chemistry, methods of acquiring PS-SFG and 2D SFG measurements have been developed. The two forms of measurement are independent of each other and reveal different information about a sample. Both methods use a type of interferometry. Although the methods were not demonstrated on the study of a chemical system of research interest, the measurements presented in this thesis suggest that they could be.

Chapter 2 details how phase-shifting interferometry was used to enable PS-SFG measurements. The phase-shifting was implemented by rotating dispersive optics in the beam path, which is shown to be effective in the measurements presented. It was found that the phase shifts were best to be determined experimentally through reference measurements on the setup itself, rather than with the theoretical predictions presented in Chapter 2.

Chapter 3 details how 2D SFG measurements were enabled through the use of a novel implementation of the Michelson interferometer commonly used in FTIR spectrometers. Although a pump-probe 2D SFG measurement of a sample was not demonstrated due to failure to observe population transfer in a sample, a 2D SFG spectrum produced directly from the pump pulse is presented to demonstrate the methods ability to resolve pump frequencies.

Chapter 4 details the challenges that still need to be overcome and some possible chemical systems to be studied with the methods developed in this thesis.

2 Phase-sensitive Measurements

This chapter describes the work that was done to enable the measurement of phase-sensitive SFG-VS spectra. Although the extraction of meaningful chemical information is not demonstrated, the working of the measurement methodology is.

2.1 Phase-shifting Unit (PSU)

For the reasons discussed in the introduction chapter, phase-shifting was chosen as the means of phase-sensitive measurement. A previous implementation of this method is described in literature.[22] To control the phase with respect the sample, a phase-shifting unit (PSU) was used. A diagram of the PSU implemented in this work is shown in Figure 2.1.

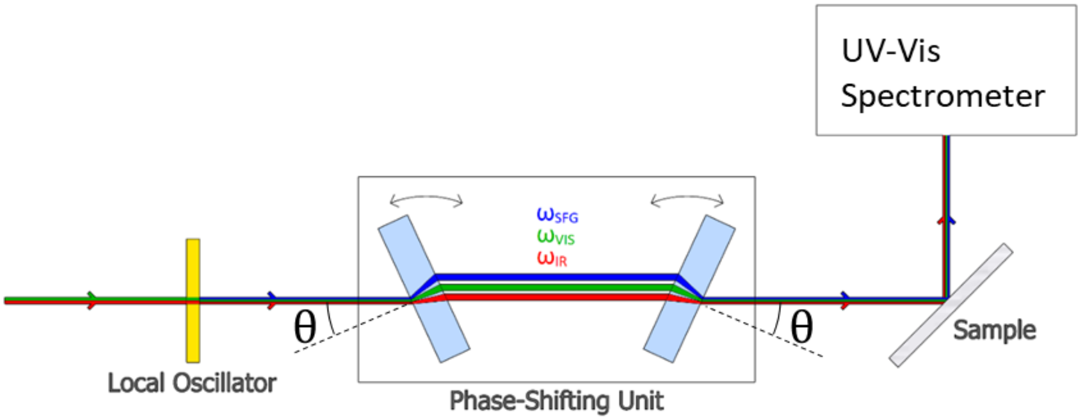

Figure 2.1. Diagram of the phase-shifting unit (PSU) placed in the beam path of a SFG spectrometer. Visible (VIS) 800 nm and infrared pulses are passed through a non-linear crystal (e.g., lithium niobate), called the local oscillator (LO), to produce the LO SFG signal. The LO SFG signal, as well as the visible 800 nm and infrared pulses, are passed through the PSU. The PSU is composed of two dispersive windows mounted on rotation stages. The angles of the windows are controlled to be opposite to each other to compensate for the beam displacement caused by refraction. The phases of all the wavelengths involved are shifted with PSU angle θ. The sample is then exposed to the phase-shifted beams to produce an additional SFG signal, which interferes with the local oscillator SFG signal, with the interference observed on the UV-Vis spectrometer as a function of PSU angle θ.

The distinct feature of the PSU presented here from the one presented in literature is that it contains a second dispersive window to compensate for the beam displacement caused by refraction. This allows for thicker IR-transparent windows to be used in place of the single thin IR-absorbing window used in literature, producing greater sample signal intensity with less variation due to beam displacement.

2.1.1 Simulations

Before the phase-shifting unit (PSU) was designed and constructed, its ability to shift the phase was simulated with various window materials and thicknesses. The phase shift of the SFG from the local oscillator φ_{SFG}, after propagating through the PSU, can be given by

$$\varphi_{SFG} = 2\pi \frac{2\, d\, n_{\lambda_{SFG}}}{\lambda_{SFG}}, \tag{2.1}$$

where d is the distance propagated through one window, $\lambda_{SFG}$is the wavelength of SFG, and $n_{\lambda_{SFG}}$is the refractive index of the window at λ_{SFG}. While this is the phase shift of the SFG, it is not the only phase shift caused by the PSU; the visible and infrared light also propagate through the PSU, shifting the phase of the SFG produced by the sample by the sum of their phase shifts. Taking this into account the net phase shift φ_{net} can be given by

$$\varphi_{net} = 4\pi \left(\frac{d\, n_{\lambda_{SFG}}}{\lambda_{SFG}} - \frac{d\, n_{\lambda_{VIS}}}{\lambda_{VIS}} - \frac{d\, n_{\lambda_{IR}}}{\lambda_{IR}} \right), \tag{2.2}$$

where λ_{VIS} and λ_{IR} is the wavelengths of visible and infrared light respectively, $n_{\lambda_{VIS}}$ and $n_{\lambda_{IR}}$ are the refractive indices of the window at λ_{VIS} and λ_{IR} respectively.

While the equation above shows that φ_{net} has some dependence on the difference in refractive index of the windows at the difference wavelengths, an additional dependence on the refractive indices comes from its dependence on the distance propagated through one window d, which is a function of wavelength at non-zero incident angles due to refraction.

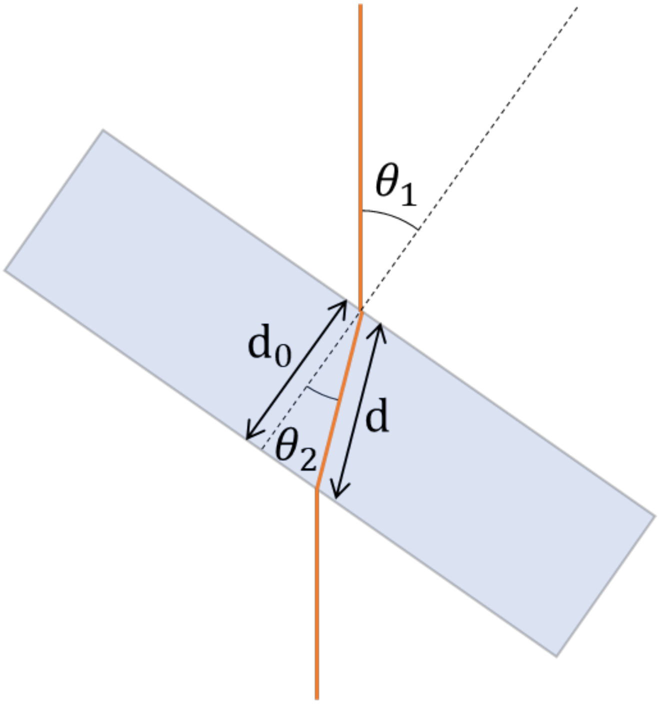

Figure 2.2. Diagram illustrating how d changes due to refraction

Using to Snell's law ($n_1 \sin\theta_1 = n_2 \sin\theta_2$), accounting for refraction, assuming air has an index of refraction of 1, d as a function of PSU angle θ can be given by

$$d(\theta) = \frac{d_0}{\sqrt{1 - \frac{\sin^2\theta}{{n_\lambda}^2}}}, \tag{2.3}$$

where d_0 is the thickness of the window, and n_λ is the refractive index for light with wavelength λ. Although the refractive index could have an imaginary component due to the absorption of light, materials with a significant amount of absorption at the wavelengths of light used would not be used for the phase-shifting unit.

The refractive indices at all the wavelengths involved were determined using Sellmeier equations published in literature[23] for various window materials, and the phase shift as a function of θ were predicted for various window thicknesses according to the equations above. As a precaution, the phase shift due to the path length change in air was also incorporated, but was found to have an insignificant effect. The result of a simulation with 5 mm thick CaF_2 windows is shown in Figure 2.3. The effects of reflectance were not incorporated into the simulations. It is recognized that the angle-dependent reflection losses could be calculated at each interface using the refractive indices and the Fresnel equations, and incorporated into the model; however, this did not present itself as an issue in determining if a material was viable to use in the PSU, as the reflection losses could be accounted for in fitting the model. It is also recognized that these reflections could be accounted for in the model when fitting the data to extract the complex spectrum, if the need presented itself. Absorption could not be accounted for in the model because the extinction coefficient of CaF_2 could not be found for the wavelengths of light used, presumably because it is too small to be accurately measured.

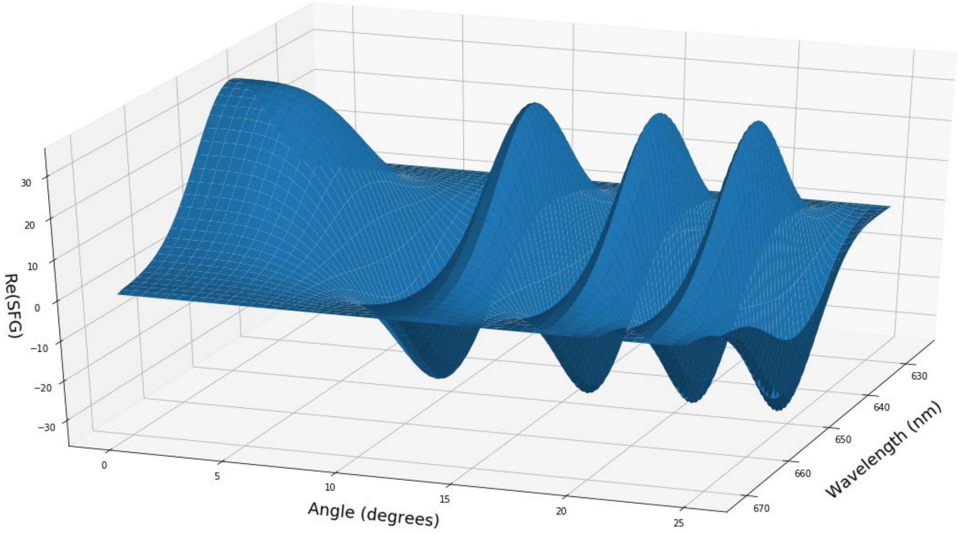

Figure 2.3. Simulated real part of the complex field amplitude of SFG from a sample with a phase relative to the local oscillator as a function of the PSU angle θ and SFG wavelength. The phase of the sample is set arbitrarily to zero at $\theta = 0$ for the purpose of illustration. The windows are made of CaF_2 and have a thickness of 5 mm in the simulation.

It was found that many materials make a suitable choice for the windows so long as an appropriate thickness is chosen for the dispersion of the material. CaF_2 was chosen for both its low cost and low optical density for all the wavelengths involved. A thickness of 5 mm was chosen as a trade-off between the requirement to accurately control the window angle with a large window thickness, and the loss off optical cross-section available to the incident light at the sharp incident angles required to shift the phase with a small window thickness.

2.1.2 Design and Construction

The addition of the phase-shifting unit (PSU) to existing SFG spectrometers presents an obstacle due the required space. In order to demonstrate the viability of adopting this means of measurement, the PSU was designed to be compact as possible, while still having a simple construction. The rotation stages chosen to rotate the windows were high-precision (400 steps/revolution) stepper motors with optical post holders mounted to their shafts. This cube-like shape of the stepper motors allowed for them to be mounted against each other and their bases mounted directly against the optical table using 3D-printed brackets, allowing for metal-to-metal construction without custom-made metal parts. A picture of the PSU is shown in Figure 2.4.

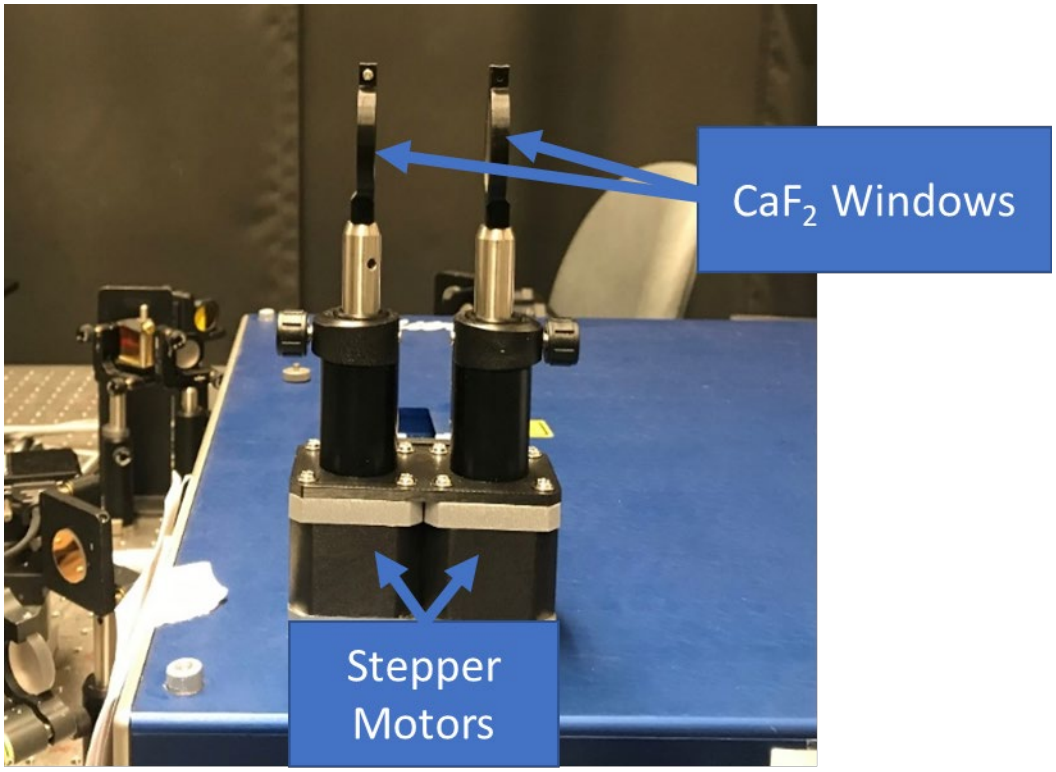

Figure 2.4. Picture of PSU without control board or mounting brackets. Custom optical mounts were designed and 3D-printed to prevent obstruction of the beam path at sharp PSU angles. The centers of the windows were offset from the centers of rotation to maximize the usable optical cross-section available to the beams across all PSU angles.

In order to allow for such a simple design, the stepper motors had to be homed using stall detection at their limits of travel without the use of limit switches. The Trinamic TMC5041 motion controller IC was chosen to satisfy this requirement. The motion controller IC uses an SPI interface to command the motors. To provide an interface to a computer, a PCB was designed and assembled to provide a USB-to-SPI interface as well as connections for the motors and power supply. The PCB is shown in Figure 2.5 and Figure 2.12.

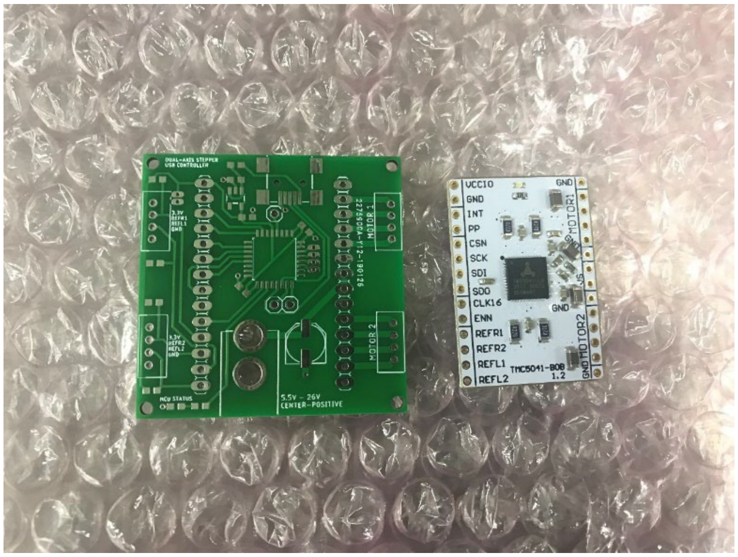

Figure 2.5. Picture of custom-made USB-to-SPI PCB (left) and Trinamic TMC5041 motion controller IC breakout board (right). The custom-made PCB was designed using Eagle EDA software[24] and fabricated by JLCPCB[25] PCB fabrication house.

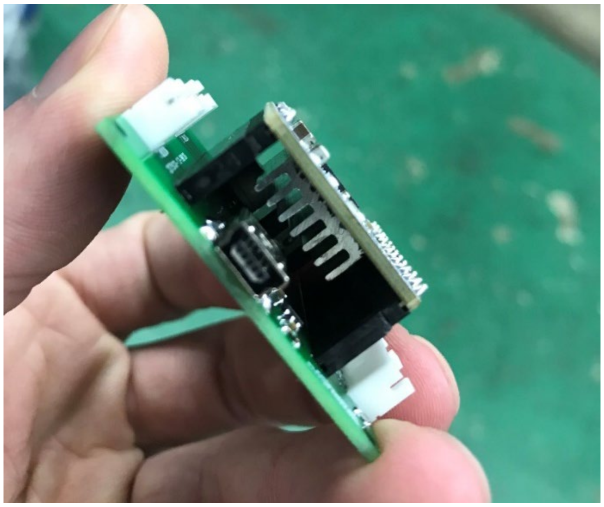

Figure 2.6. Picture of assembled PSU control board with heatsink installed on the underside of the motion controller to prevent the integrated motor drivers from overheating. The heatsink used passive cooling.

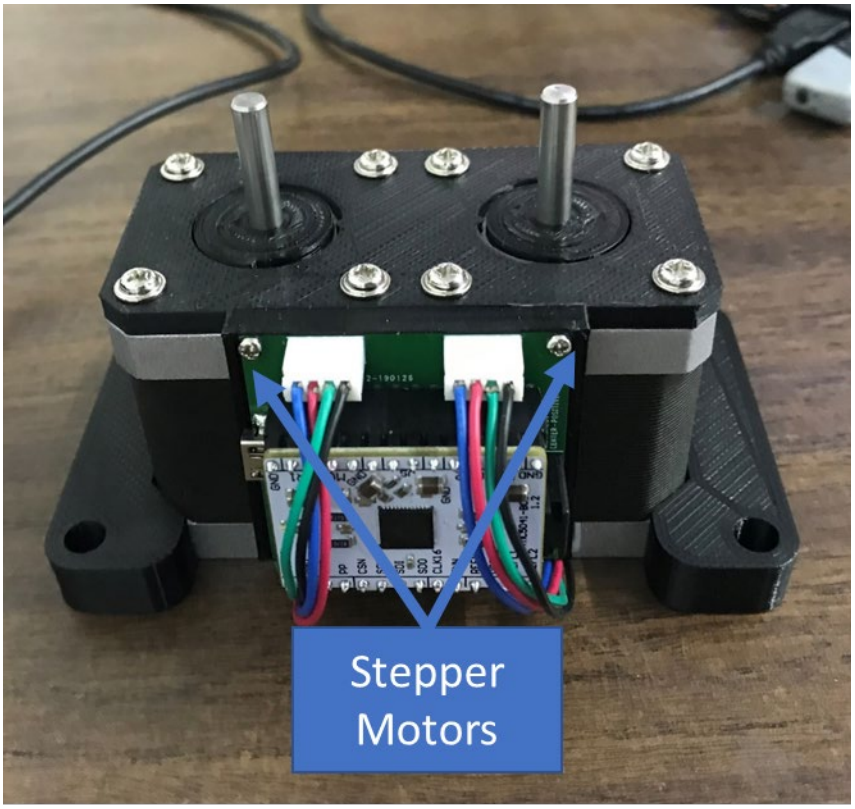

Figure 2.7. Picture of PSU without optical post holders installed on the stepper motor shafts. Plastic stoppers were mounted onto the bases of the stepper motor shafts, with notches to restrict the range of motion of the stepper motors to 180° and to provide a physical limit to home against. The original stoppers were printed using PLA plastic, which was found to be too stiff to grip the shafts enough to stop the motors from rotating. Flexible PETG plastic was used in its place. Distortion of the PETG plastic was not visible when stopping the motors.

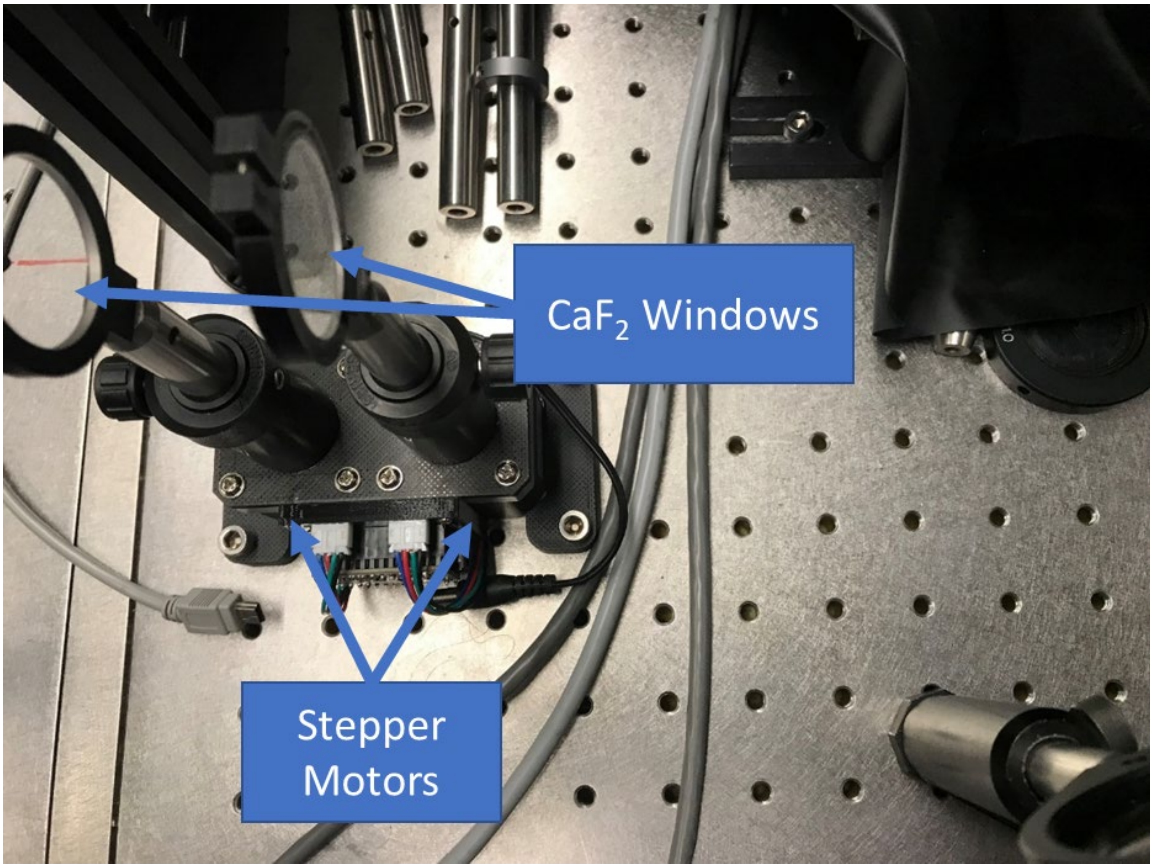

Figure 2.8. Picture of PSU installed in the SFG spectrometer.

2.2 Data and Analysis

The data presented in this section was collected using a 0.5 mm lithium niobate window (single crystalline, θ=51.3°, polished) as the local oscillator and a piece of gallium arsenide wafer (single crystalline, polished) as the sample. The purpose of this data is only to demonstrate the ability to extract a complex field amplitude spectrum from the phase-shifting measurements acquired using the phase-shifting unit (PSU). The complex field SFG amplitude spectrum of gallium arsenide is not of research interest as it is a non-resonant signal and expected to be the direct result of the phase of light it is exposed to. It does, however, present itself as a viable reference for the phase of light a resonant sample is exposed to, allowing for the uninteresting phase shift related to the layout of the spectrometer, to be separated from the interesting phase shift caused by resonance in the sample. The phase of the complex spectra presented in this section is purely the uninteresting phase shift related to the layout of the spectrometer.

2.2.1 Fitting of Physical Model

The purpose of this subsection is to show the attempt that was made to extract a complex field amplitude spectrum through fitting the physical model presented in the previous section to experimental data. The goal is to demonstrate the inability of the physical model to fit the data with the fitting methods used. If reading this subsection casts doubt the fitting methods used, it is advised to skip to the next subsection, where the same fitting methods are used with an alternative empirical model.

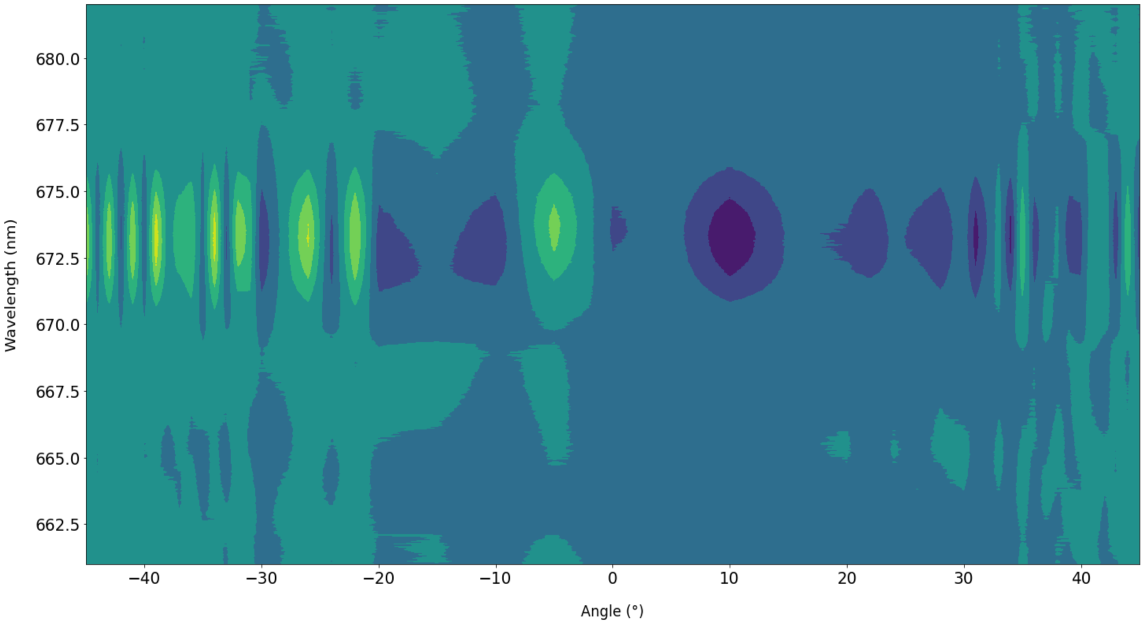

Figure 2.9. Contour plot of SFG intensity as a function of PSU angle and wavelength. The average intensity at each wavelength was subtracted over all PSU angles to better show the oscillations in intensity rather than the absolute intensity that does not change with PSU angle.

The data shown in Figure 2.9 was attempted to be fit to the physical model presented in the previous section. The expected SFG intensity as a function of the PSU angle θ can be given by

$$I(\theta) = \left|E_{LO}\, e^{i(\varphi_{net}(\theta)-\varphi_{net}(0))} + E_{Sample}\right|^2, \tag{2.4}$$

where $E_{LO}$is the field amplitude of the SFG produced by the local oscillator (made to be positive and real), $E_{Sample}$is the complex field amplitude of the SFG produced by the sample (with a phase that is relative to the SFG produced by the local oscillator when $\theta =$

0), and $\varphi_{net}(\theta)$ is the phase shift as defined from the equations 2.2 and 2.3 in the previous section.

The physical model was found to be too constrained to allow for a good fit of the predicted phase shifts to the experimental ones. To provide more flexibility to the model, the thickness of the window was allowed to change to better fit the data. In addition a PSU offset angle was also optimised to accomodate for misalignment of the setup. The results of the fit are shown in Figure 2.10-Figure 2.12.

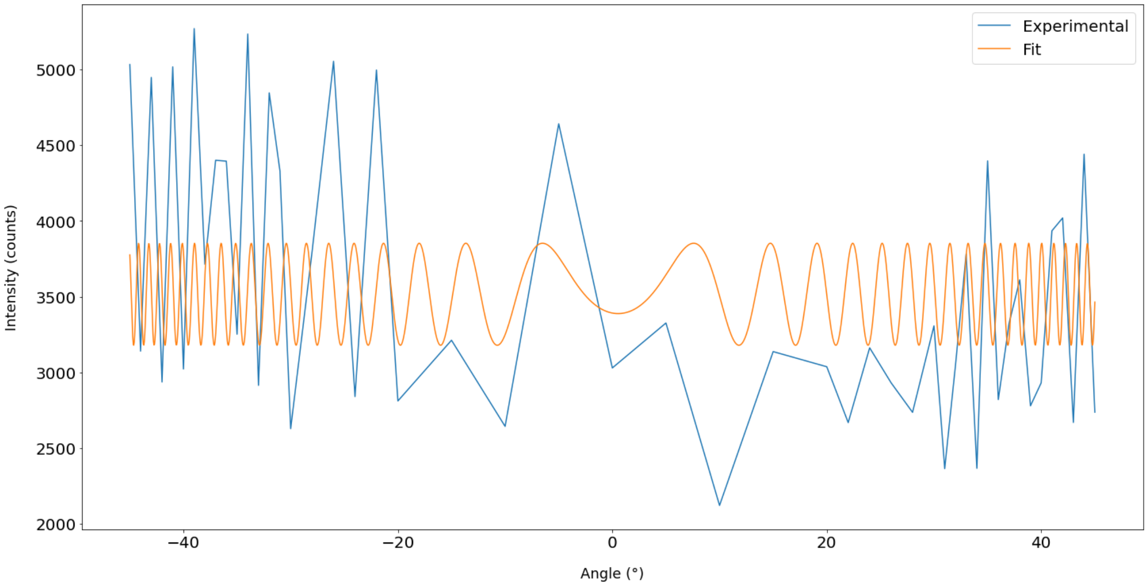

Figure 2.10. Experimental data (blue) with a wavelength of 673 nm with fit (orange). To better show the transition between data points, the experimental data was plotted with a line rather than with scatter points.

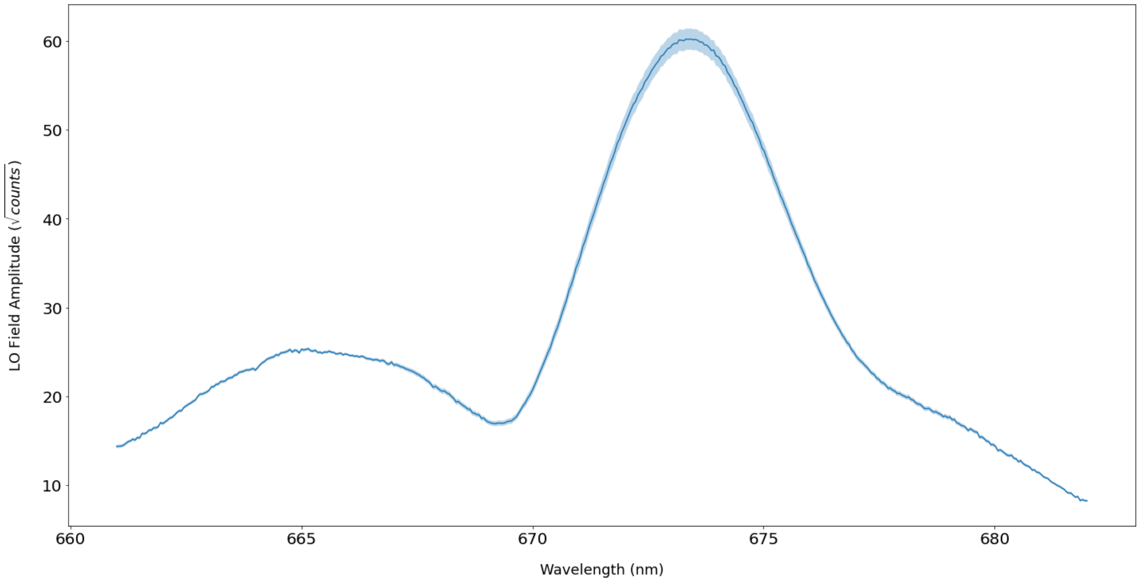

Figure 2.11. Fitted LO field amplitude spectrum. The shaded region shows 1-sigma error estimates.

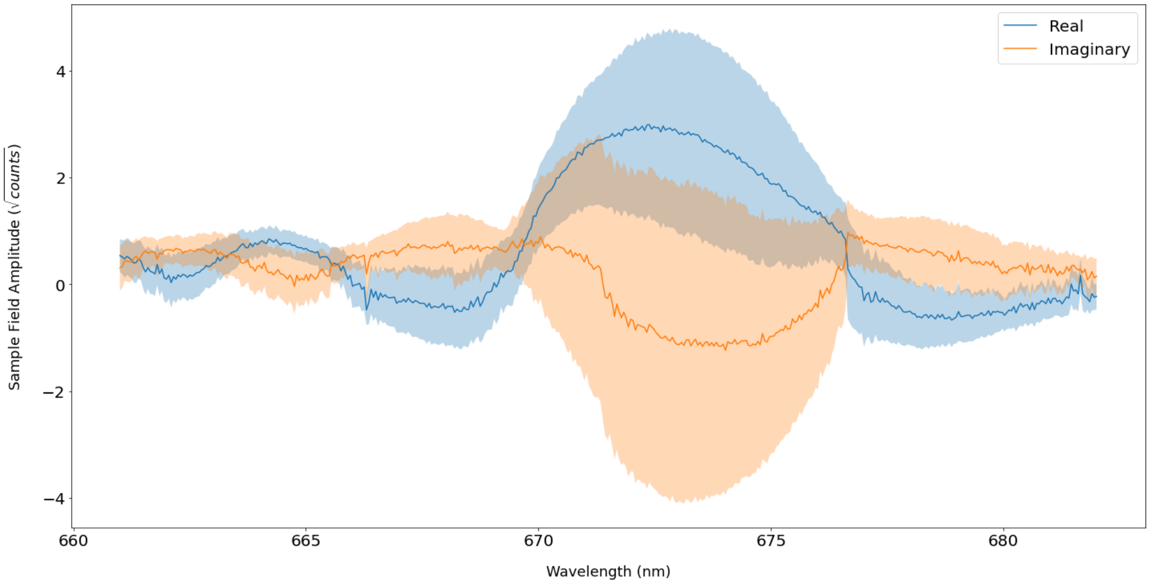

Figure 2.12. Fitted sample complex field amplitude spectrum. The shaded regions show 1-sigma error estimates.

As shown in Figure 2.10, the result of the fit does not show good agreement with the experimental data, resulting in the large relative error estimates seen in Figure 2.12. If nothing else, the fit of this data demonstrates the need to calclulate error estimates before attempting to make sense of the fit.

In order to avoid the aliasing seen in the experimental data in Figure 2.10, new data was collected at a higher sampling rate (in terms of PSU angle). The data along with the fit of the physical model is shown in Figure 2.13.

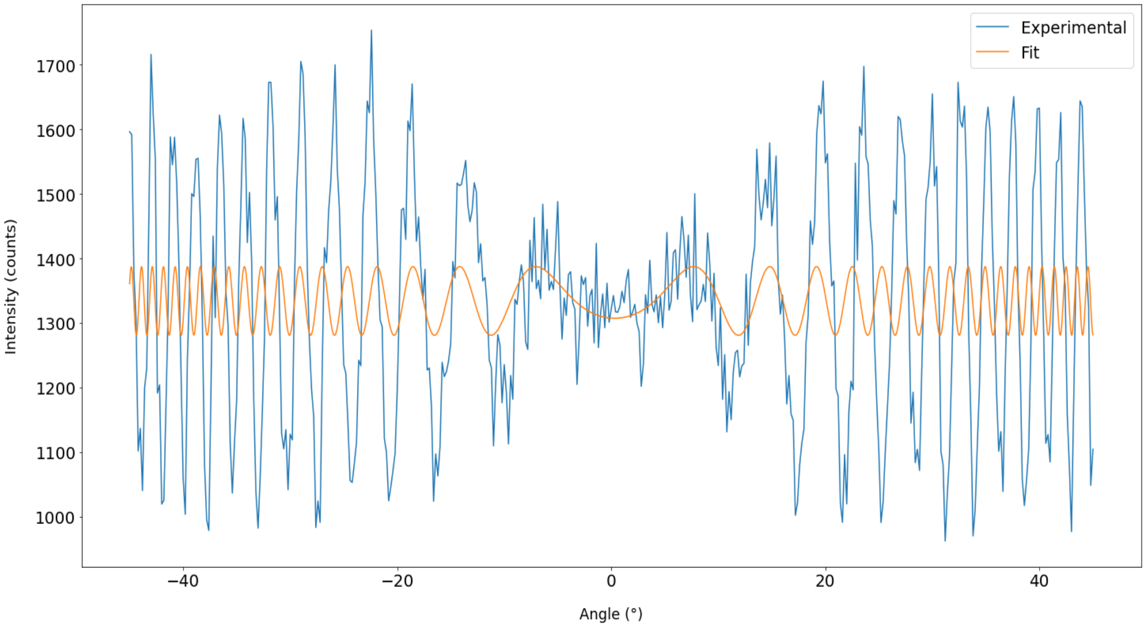

Figure 2.13. Experimental data (blue) at wavelength of 673 nm with fit (orange). The data shown is a slice of the data shown in Figure 2.15.

Even with sufficiently sampled data, the physical model still fails to show agreement with the phase shifts observed. In attempt to demonstrate the physical model showing some agreement to the experimental data, the data of Figure 2.13 was truncated to small angles and fit. The result is shown in Figure 2.14.

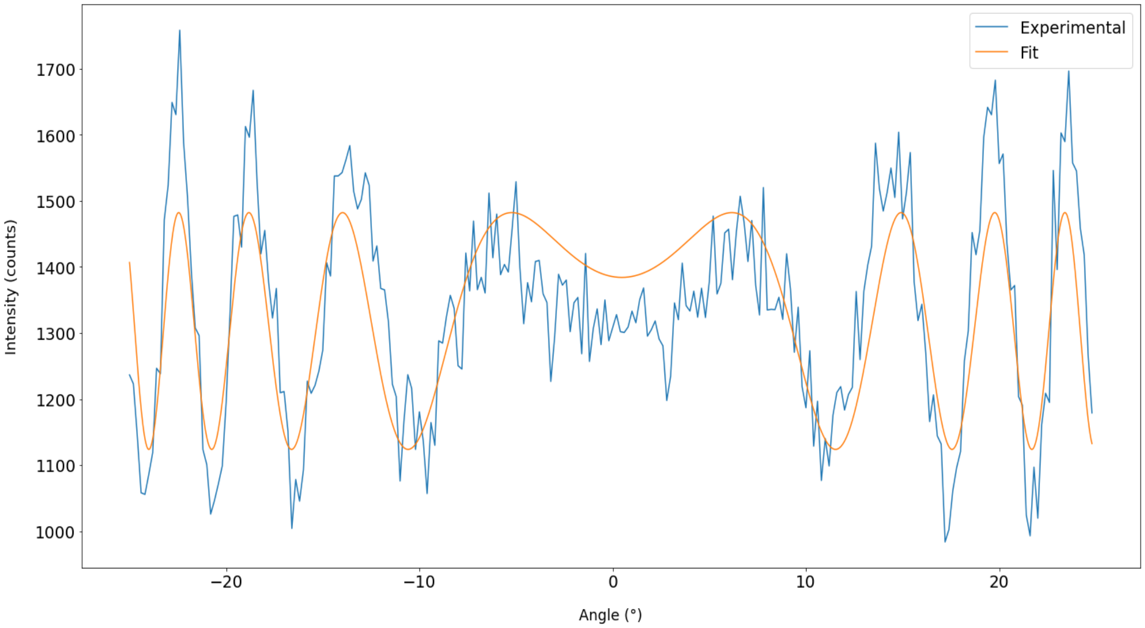

Figure 2.14. Truncated experimental data from Figure 2.13 (blue) with fit (orange). The fitted window thickness was 5.25 mm, comparable to the true value of 5 mm.

While the fit in Figure 2.14 shows better agreement, it still produces large relative error estimates in the sample complex field amplitude spectrum, even more so than with the under-sampled data. The level of agreement seen in Figure 2.14 does inspire some confidence in the physical model, but not to the extent where it could be used to extract the complex spectrum of the sample within an acceptable level of uncertainty.

2.2.2 Improved Fitting with Empirical Model

The physical model used in the last sub-section was found to be overly constrained to fit to data that was collected over a large range of PSU angles. An example of such data is shown in Figure 2.15 and Figure 2.16.

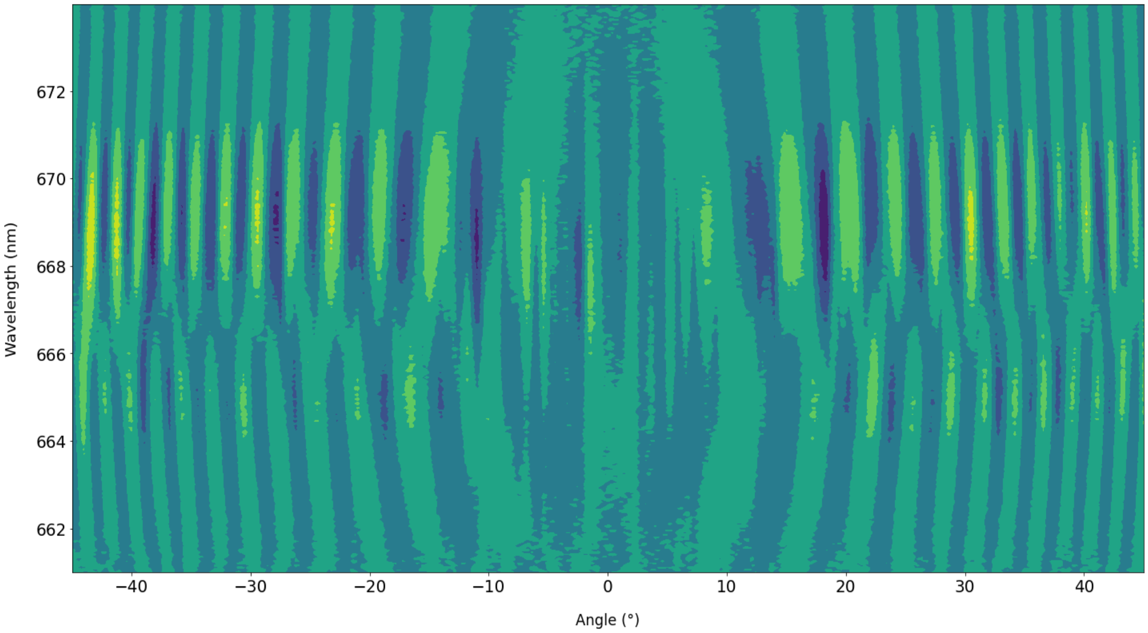

Figure 2.15. Contour plot of SFG intensity as a function of wavelength (y-axis) and PSU angle (x-axis) over the range of data fit. The average intensity at each wavelength was subtracted over all PSU angles to better show the oscillations in intensity rather than the absolute intensity that does not change with the PSU angle.

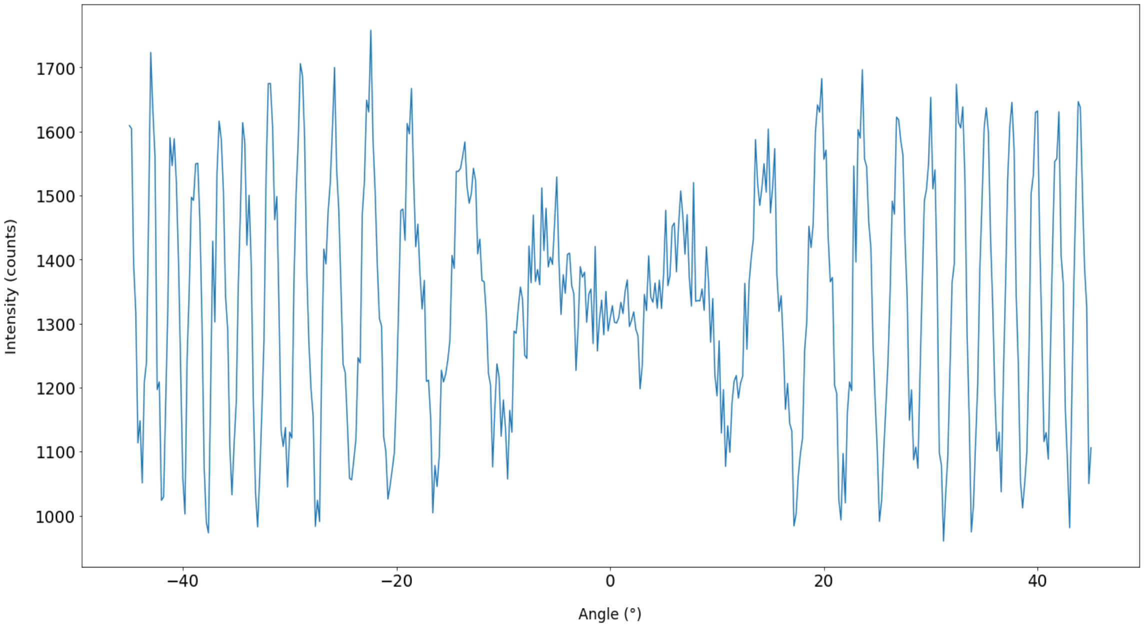

Figure 2.16. SFG intensity at 673 nm as a function of PSU angle.

The quality of the data in Figure 2.16, in particular the observation of multiple oscillations, allows to extract the phase shift as a function of the PSU angle theta without application of a physical model. At $\theta = 0$, the oscillation starts with some phase which changes symmetrically about $\theta = 0$. The derivative of the phase with respect to θ appears to be proportional to theta as well. An equation that satisfies these observations is

$$\varphi(\theta) = a\theta^2, \tag{2.5}$$

Where φ is the apparent phase shift from $\theta = 0$, and *a* is a coefficient to be fitted, which relates the rate of the phase change to the magnitude of the PSU angle θ. The SFG intensity $I(\theta)$ at a given wavelength can then be given by

$$I(\theta) = \left|E_{LO}\, e^{i\varphi(\theta)} + E_{Sample}\right|^2, \tag{2.6}$$

Where $E_{LO}$is the field amplitude of the SFG produced by the local oscillator (made to be positive), while E_{Sample} is the complex field amplitude of the SFG produced by the sample (with a phase that is relative to the local oscillator when $\theta = 0$). The equation above was used to fit the 451 data points of the data shown in Figure 2.16 to just 4 parameters: E_{LO}, Re(E_{Sample}), Im(E_{Sample}) and *a*; however, a fifth parameter, θ_{offset}, had to be added to accommodate for misalignment of the setup, giving

$$\varphi(\theta) = a\left(\theta + \theta_{offset}\right)^2. \tag{2.7}$$

Figure 2.17 shows the ability of the equations above to predict the phase of oscillations seen at different wavelengths.

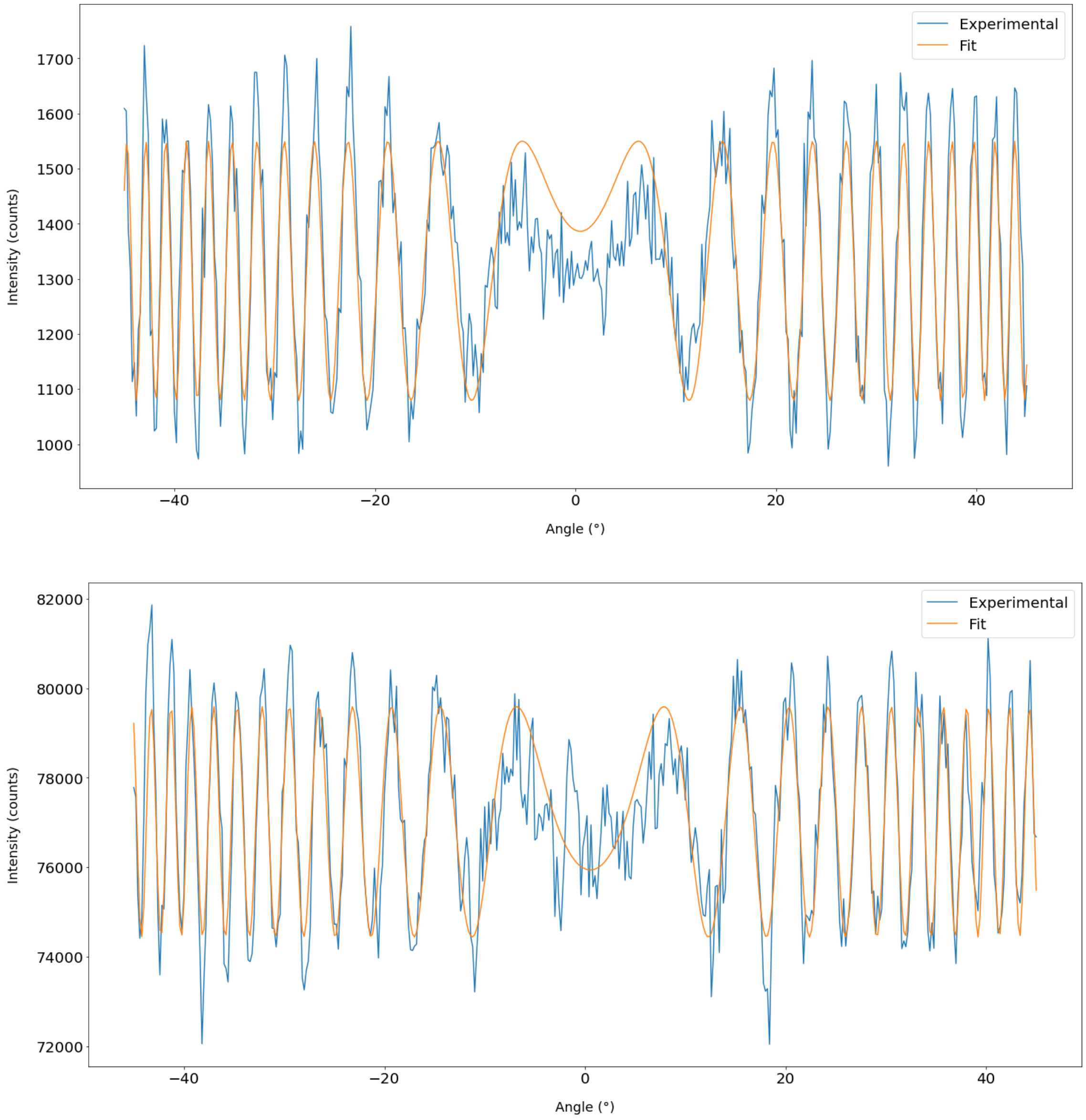

Figure 2.17. Experimental data (blue) with wavelengths of 673 nm (top) and 669 nm (bottom), with corresponding fit (orange). The fits at each wavelength were performed independent of the others. To better show the transition between data points, the experimental data was plotted with a line rather than with scatter points.

The equations presented above were fit to all of the wavelengths shown in Figure 2.15. The results are shown in Figure 2.18-Figure 2.20.

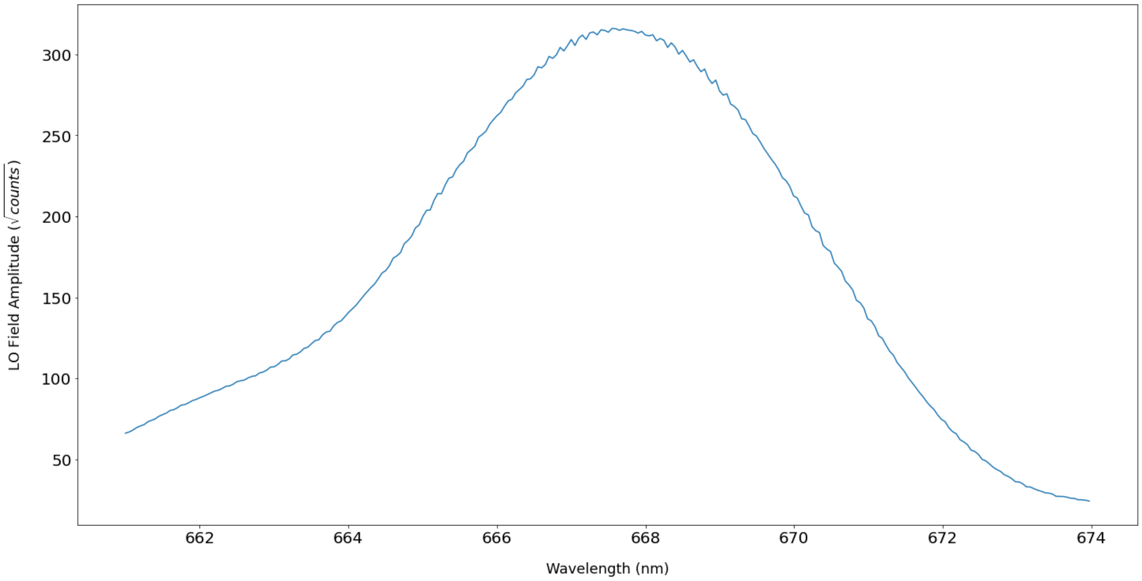

Figure 2.18. Fitted LO field amplitude spectrum. The shaded region showing error estimates cannot be seen due to their small values.

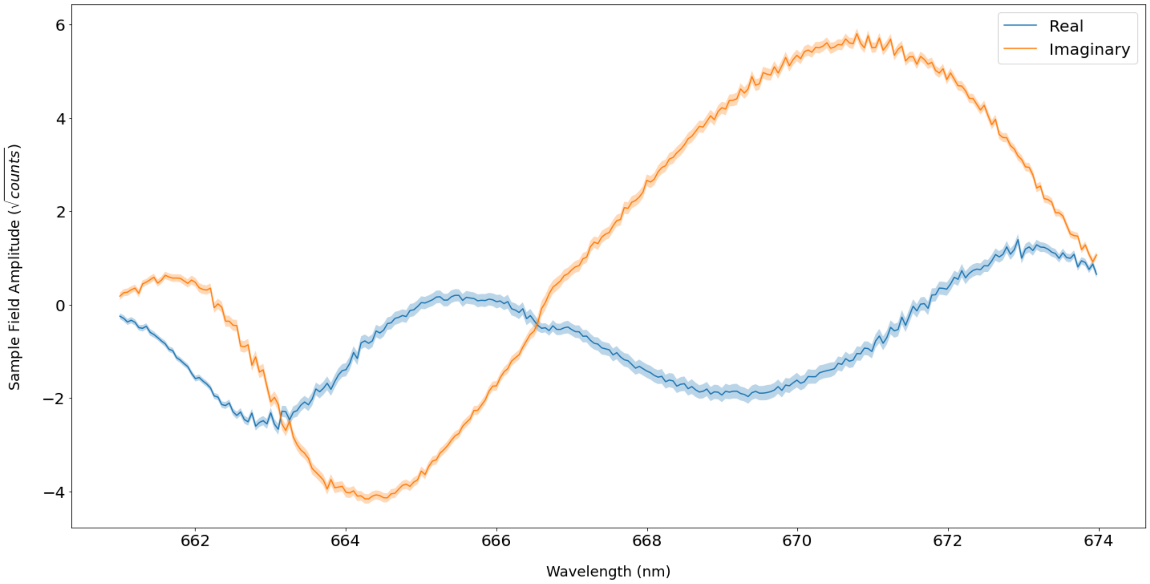

Figure 2.19. Fitted sample complex field amplitude spectrum. The shaded regions show 1-sigma error estimates.

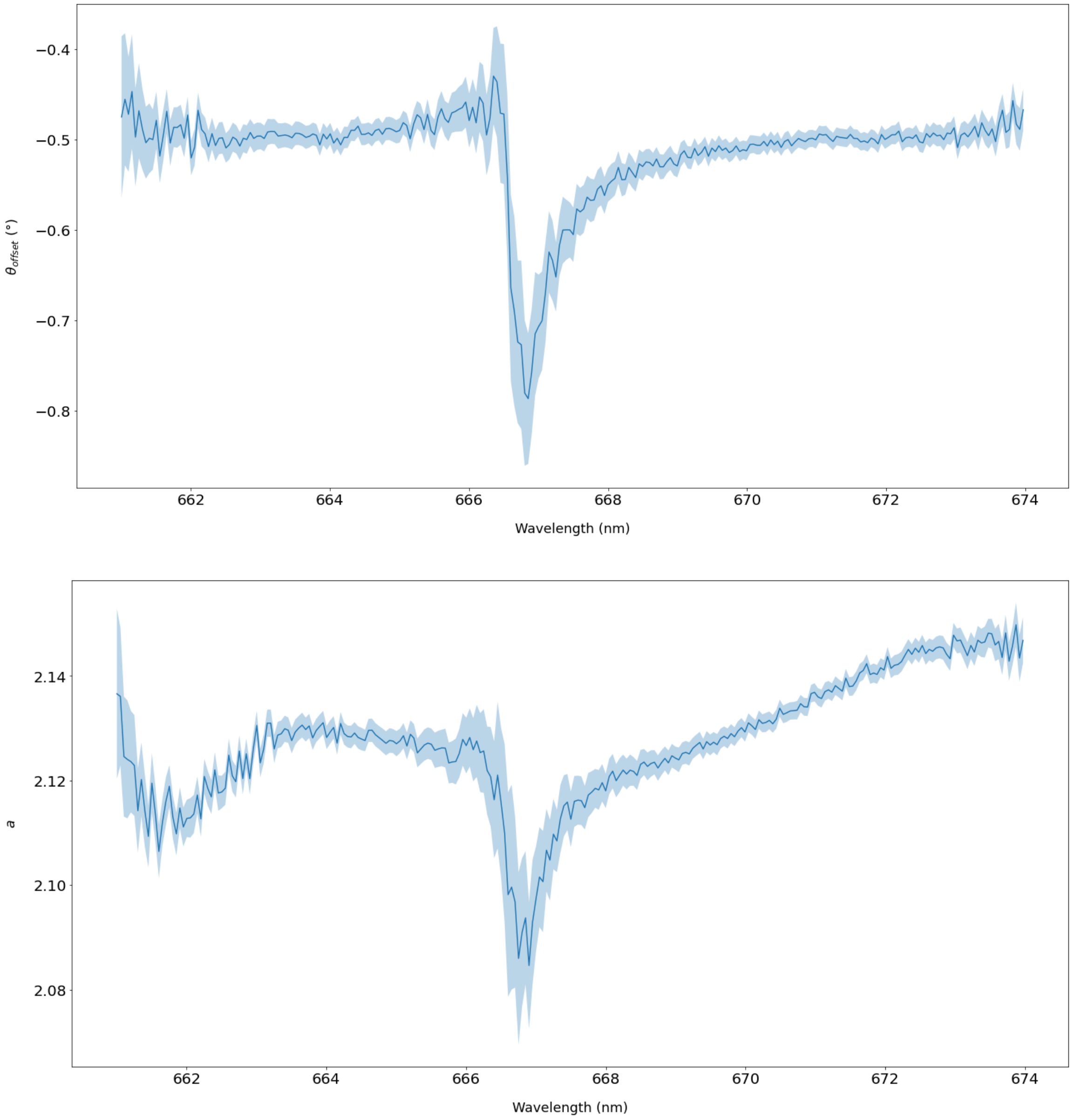

Figure 2.20. Fitted θ_{offset} (top) and coefficient *a* (bottom) as a function of wavelength. The shaded regions show 1-sigma error estimates. The distinct feature at 666.8 nm is discussed in the next subsection.

2.2.3 Discussion

The distinct features observed in the fitted parameters shown in Figure 2.20 could be a topic of discussion; however, no repeat measurements were preformed to confirm whether these features are reproducible. While the features are not expected to inhibit the ability to extract a complex spectrum, they may be an indication of deficiencies in the measurement technique. More data would have to be acquired to confirm this.

While the fit with the physical model shows some agreement with the experimental data, providing validation of the simulations performed in preparation for the construction of the phase-shifting unit (PSU), the empirical model presented in this section is the preferred method for extracting the complex sample spectrum from the phase-shifting measurements acquired with the PSU. It is recognized that the disagreement with the physical model may be the result of setup misalignment; however, the empirical model appears to accommodate for setup misalignment while not presenting any disadvantage in the absence of it. Setup misalignment is suspected due to the fact that the empirical model would show the best agreement when an angle offset was included in the model, as well the data not being symmetric about $\theta=0^\circ$ but rather $\theta=0.5^\circ$. There were no coatings on the optics in the PSU, so this is not suspected to be the source of disagreement with the physical model. The success of the empirical model exemplifies the importance of not constraining the treatment of the data to how it should be, but rather to how it is. A requirement of phase-shifting measurements is to shift the phase by some predictable amount. The results in this section suggest it is more effective to predict the amount of phase shift through experimental observation rather than theoretical models.

3 Two-dimensional Measurements

3.1 Introduction

This chapter describes the work that was done to design and construct a spectrometer capable of acquiring a 2D SFG-VS spectrum. For brevity, the spectrometer described in this chapter will be referred to as the “2D spectrometer,” not to be confused with the UV-Vis spectrometer used to measure the 1D SFG spectrum, which is only a component of the 2D spectrometer. A simplified schematic of the 2D spectrometer is shown in Figure 3.1.

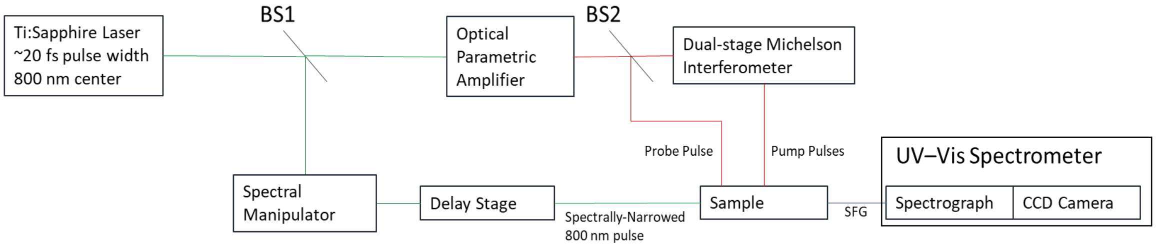

Figure 3.1. Simplified schematic of the 2D spectrometer. Ti:Saphhire laser is a Coherent Legend Elite Duo, pumped by a Coherent Evo laser, seeded by a Coherent Micra laser, with a pulse energy of 6 mJ and repetition rate of 1 kHz. Only a 4.5 mJ total pulse energy is used in the spectrometer which is split by beamsplitter BS1; 3 mJ is used to pump the optical parametric amplifier (OPA) and 1.5 mJ is spectrally-narrowed by the spectral manipulator. The OPA (described in Section 3.2) is built in-house. The output of the OPA is split by beamsplitter BS2 to produce probe and pump infrared pulses used to excite the vibrational modes of the sample. The dual-stage Michelson interferometer (described in Section 3.4) splits the pump pulse into two pulses and controls their relative and absolute time delays. The UV-Vis spectrometer is the means of SFG signal detection and is composed of a Newport MS260i imaging spectrograph, with 300 and 1200 grooves/mm gratings installed, and an Andor Newton 970 EMCCD camera.

While the 2D spectrometer is largely based on a previous implementation of a 1D SFG spectrometer used at SFU[7], several improvements to the existing 1D SFG spectrometer were made or attempted in consideration of taking 2D measurements. A new optical parametric amplifier (OPA) was designed and constructed to produce pump pulses of sufficient intensity to observe population transfer of molecules to the excited state. A new spectral manipulator was constructed to improve the resolution of the SFG measurements and increase SFG signal intensity. A wavelength calibration procedure was developed for the UV-Vis spectrometer which measures the SFG signal. Although these improvements are described in this chapter, their value is not limited to the ability to take 2D measurements.

The distinguishing feature of the 2D spectrometer is the addition of two pump pulses used to excite molecules and then probe them in their excited state. The dual-stage Michelson interferometer, described in Section 3.4 , is used to as a means to control the relative time delay τ and absolute time delay T of the two pump pulses, and can be considered the heart of the 2D spectrometer. The time delays that the variables τ and T correspond to are shown in Figure 3.2.

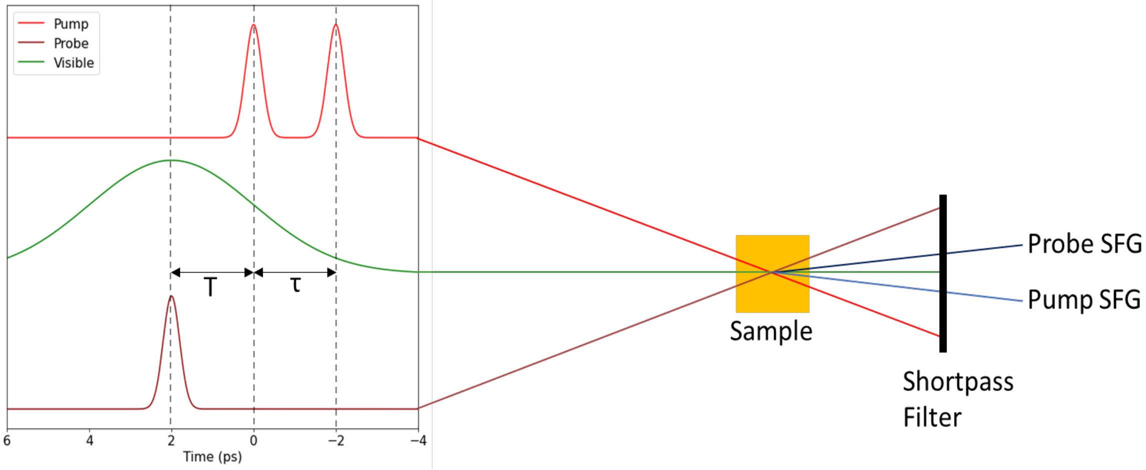

Figure 3.2. Simplified diagram of the pulses involved in the 2D spectrometer. Focusing optics are not shown. The y-axis of the plot shown in the left panel is field amplitude, which is not shown due to the y-offset used to depict spatial separation between pulses. The pump SFG is only used for calibration and not to collect a 2D spectrum.

The use of two interfering pump pulses gives spectral resolution through the use of interferometry. By scanning over τ, the delay between pump pulses, an interferogram is produced at all SFG frequencies. This interferogram can be Fast Fourier Transformed (FFT'd) for every SFG frequency to produce a 2D spectrum with pump wavenumber and probe wavenumber as its axes.

Though the absolute time delay T is not scanned when a single 2D spectrum is acquired, it still remains an acquisition parameter which needs to be controlled and reported accurately. Having the ability to accurately control T also presents the ability to take time-resolved 2D SFG measurements.

3.2 Optical Parametric Amplifier (OPA)

The ability to observe peaks in a 2D SFG spectrum depends on the amount of population that is transferred to an excited state, which is proportional to the intensity of the pump pulse used to excite the molecules. The ability to generate enough mid-IR light to transfer population presents the biggest challenge in collecting a 2D spectrum. In attempt to overcome this, an optical parametric amplifier (OPA), described in this section, was designed to more efficiently convert 800 nm pulses into mid-IR pulses. The OPA was purposely built to produce mid-IR near 2900 cm^{-1} (3450 nm) to excite CH stretches, which meant that wavelength flexibility could be sacrificed for greater efficiency at the desired wavelength. Figure 3.3 shows the non-linear optical processes involved in converting 800 nm light into mid-IR light for SFG-VS spectroscopy used previously at SFU Chemistry. Figure 3.4 shows the non-linear optical process proposed to be used for the 2D spectrometer.

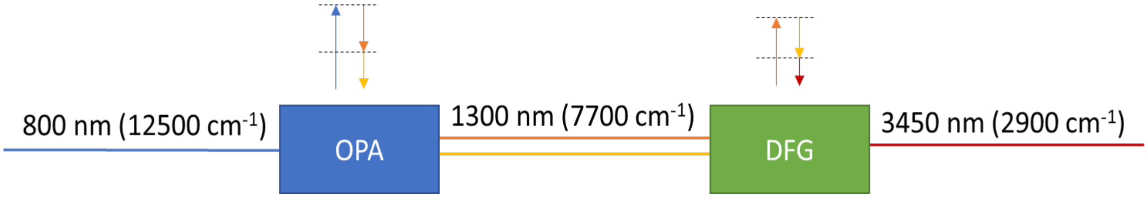

Figure 3.3. Diagram of the non-linear optical processes that were involved previously to generate ultrashort mid-IR pulses for SFG-VS at SFU Chemistry. Optical parametric amplification (OPA) is used generate two intermediate pulses, which are then used in difference frequency generation (DFG) to generate a pulse with the desired mid-IR frequency. The arrows illustrate the transitions between the energy levels involved in each process. Both processes were done in the commercially available Quantronix Palitra-FS Duo optical parametric amplifier.

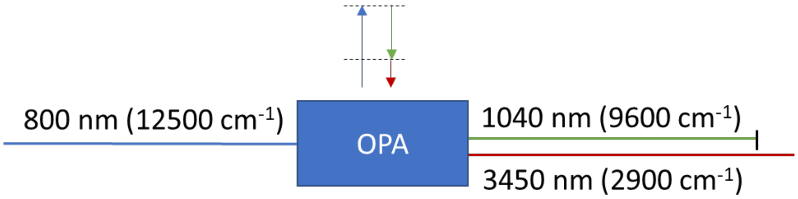

Figure 3.4 Diagram of the single non-linear optical parametric amplification process proposed in this work to generate ultrashort mid-IR pulses to be used in the 2D spectrometer. The arrows illustrate the transitions between the energy levels involved.

The material of the non-linear crystals used in the existing Quantronix Palitra-FS Duo OPA, bismuth triborate (BiBO), does not have sufficient transmission for the direct generation of the mid-IR light needed to excite CH stretches, which is supported by the fact that the existing OPA was unable to produce output at this frequency. Another material had to be selected which provides sufficient transmission, non-linear susceptibility, and the ability to phase match at the desired wavelength. Phase-matching is the condition where the refractive indices of a crystal are similar for the wavelengths of light involved in a non-linear process, allowing for constructive interference for light generated across the length of the crystal, due to its phase being matched. Phase-matching can be achieved through rotating a birefringent crystal, to tune the effective refractive index for the desired wavelengths of light. The crystal can be cut at or near the correct angle to minimize the effects of refraction. Various alternatives to BBO were considered, lithium niobate was chosen for the reasons given in the next paragraph.

Not only is lithium niobate able to phase-match effectively to produce the desired mid-IR wavelength while being transmissive, it also has a similar group velocity for all the wavelengths involved. The group velocity is an effective refractive index that takes into account the effect of dispersion on ultrashort pulses. The time that it takes for an ultrashort pulse to propagate across the crystal is inversely proportional to the group index. By having a similar group velocity for all the wavelengths involved, the wavelengths are able to stay overlapped in time for a longer distance within the crystal, allowing for greater amplification. Lithium niobate also presented itself as a suitable choice in literature[26,27], with an overall conversion efficiency (in terms of power) up to 3% at the desired wavelength[27], which would be a substantial improvement over the 0.5% overall conversion efficiency of the existing Quantronix Palitra-FS Duo OPA at the desired wavelength.

Non-linear optical calculations were performed using SNLO software[28] to compare the non-linear properties between bismuth triborate and lithium niobate. The results of which are shown in Figure 3.5. It was found that lithium niobate has an effective nonlinearity of -4.29 pm/V, which is significantly greater in magnitude than bismuth triborate's nonlinearity of 2.7 pm/V with the same type of phase matching. This suggests that lithium niobate is a viable choice for the direct generation of mid-IR light.

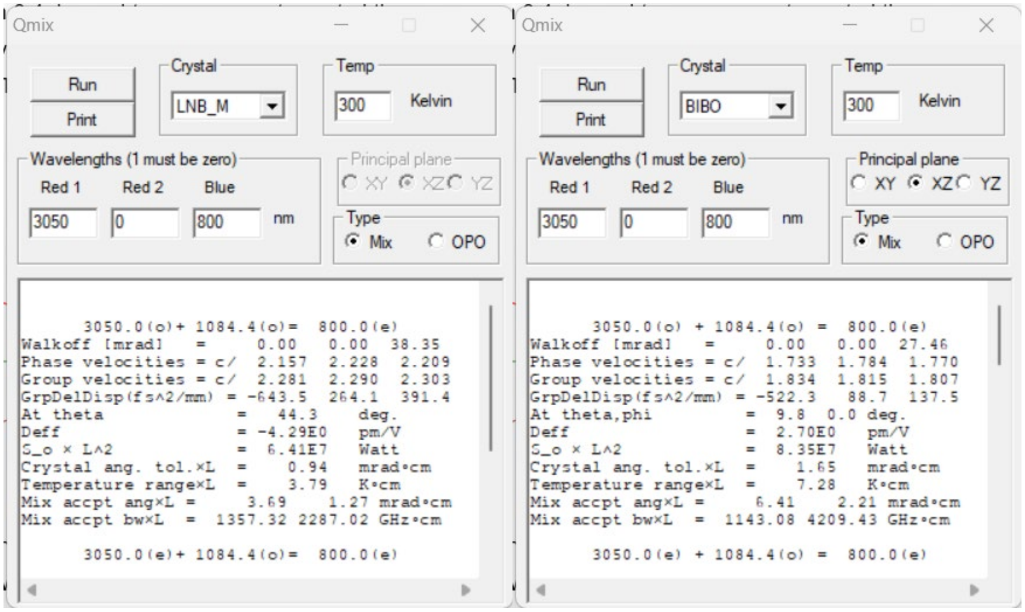

Crystal: LNB_M
Temp: 300 Kelvin
Wavelengths (1 must be zero): Red 1 3050, Red 2 0, Blue 800 nm
Principal plane: ○ XY ● XZ ○ YZ
Type: ● Mix ○ OPO

```
      3050.0(o)+ 1084.4(o)=  800.0(e)
Walkoff [mrad]    =      0.00   0.00  38.35
Phase velocities = c/  2.157  2.228  2.209
Group velocities = c/  2.281  2.290  2.303
GrpDelDisp(fs^2/mm) = -643.5  264.1  391.4
At theta                =   44.3    deg.
Deff                    = -4.29E0   pm/V
S_o × L^2               =  6.41E7   Watt
Crystal ang. tol.×L  =     0.94   mrad•cm
Temperature range×L  =     3.79   K•cm
Mix accpt ang×L =      3.69    1.27 mrad•cm
Mix accpt bw×L  =  1357.32 2287.02 GHz•cm

      3050.0(e)+ 1084.4(o)=  800.0(e)
```

Crystal: BIBO
Temp: 300 Kelvin
Wavelengths (1 must be zero): Red 1 3050, Red 2 0, Blue 800 nm
Principal plane: ○ XY ● XZ ○ YZ
Type: ● Mix ○ OPO

```
      3050.0(o) + 1084.4(o) =  800.0(e)
Walkoff [mrad]    =      0.00   0.00  27.46
Phase velocities = c/  1.733  1.784  1.770
Group velocities = c/  1.834  1.815  1.807
GrpDelDisp(fs^2/mm) = -522.3   88.7  137.5
At theta,phi            =  9.8  0.0 deg.
Deff                    =  2.70E0   pm/V
S_o × L^2               =  8.35E7   Watt
Crystal ang. tol.×L  =     1.65   mrad•cm
Temperature range×L  =     7.28   K•cm
Mix accpt ang×L =      6.41    2.21 mrad•cm
Mix accpt bw×L  =  1143.08 4209.43 GHz•cm

      3050.0(e) + 1084.4(o) =  800.0(e)
```

Figure 3.5. Results of non-linear optical calculations for lithium niobate (5% (by mol) MgO) (left) and bismuth triborate (right). The calculations were performed using SNLO software.[28] Calculations were performed with a mid-IR wavelength of 3050 nm to fit within the known data for bismuth triborate (limited to its transmission window).

The new OPA was designed around a two-stage design found in literature[27] with modifications to accommodate for the laser pulse used to pump it. Approximately 5% of the input pump pulse (p-polarized) is reflected off a beamsplitter and focused by a lens to produce white-light continuum used as a signal seed pulse with a center wavelength of 1040 nm. The polarization of the signal seed pulse is flipped by a periscope to accommodate for phase-matching in the birefringent lithium niobate, before being amplified in two stages of amplification with lithium niobate crystals pumped with 800 nm light, to produce an amplified signal pulse at 1040 nm as well as an idler pulse with a desired center wavelength of 3450 nm. Lithium niobate is known to have a relatively low damage threshold to ultrashort laser pulses compared to other non-linear crystals;

because of this, lithium niobate is doped with MgO to increase its damage threshold.[29] The 800 nm light used in the two stages of amplification is telescoped out to avoid damaging the MgO-doped lithium niobate crystals from the extreme peak intensities of the light used. The intensities are reduced by 36% and 64% for the first and second amplification stages respectively. The optics and beam path involved in each stage of the OPA design are shown in Figure 3.6-Figure 3.8.

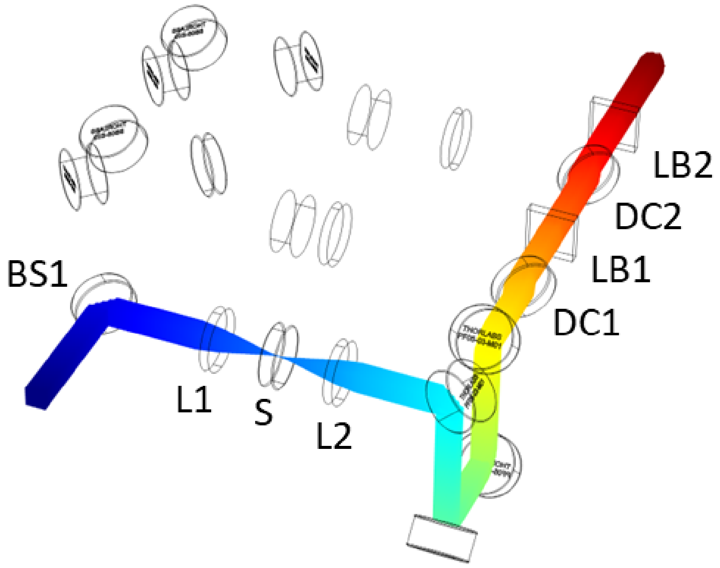

Figure 3.6. COMSOL Multiphysics raytracing simulation of the generation of the seed pulse. Beamsplitter BS1 reflects 0.15 mJ of the 3mJ ~20 fs 800 nm input pulse into lens L1 (f=15 mm)*, which focuses the beam into a spot within sapphire window S (z-cut 3 mm thick) to generate white-light continuum. The white-light continuum contains the seed pulse with a center wavelength of 1040 nm. The diverging seed beam is collimated by lens L2 and the polarization is flipped by a periscope composed of two gold mirrors. The beam is then translated up to its original level by another two gold mirrors so it can be combined with the pump pulse used for the first stage of amplification by dichroic beamsplitter DC1 (950 nm cut on). The remaining beam path is shared with the beam in the figure below and described in its caption.

---

* “f” refers to the focal length relative to the optical center of the lens.

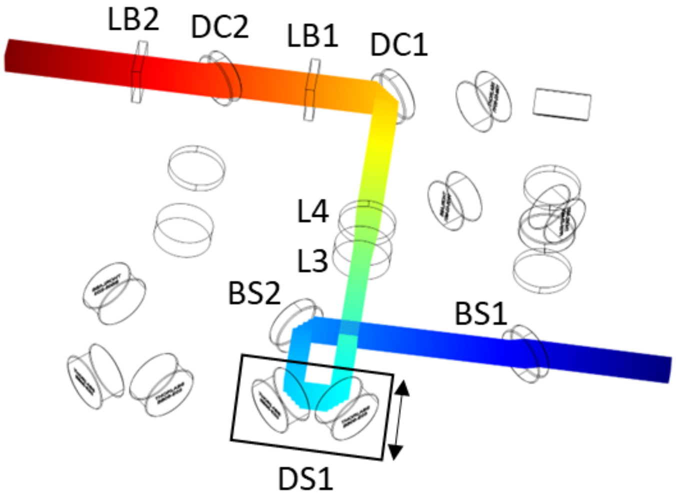

Figure 3.7. COMSOL Multiphysics raytracing simulation of the first stage of optical parametric amplification. Beamsplitter BS2 reflects 1.2 mJ of the 800 nm pulse transmitted through beamsplitter BS1 into Delay Stage DS1, which is used to control the timing of the pulse with respect to the seed pulse. The beam is then passed through a telescope composed of lenses L3 (f=-40 mm) and L4 (f=50 mm), before it is combined with the seed pulse by dichroic beamsplitter DC1 and passed through Lithium Niobate Crystal LB1 (2 mm thick, MgO:LiNbO3 (5% (by mol) MgO), Theta= 44.1°, phi=0°) for amplification of the seed pulse with a center wavelength of 1040 nm. The crystal is mounted on a custom-built motorized rotation stage (not shown) to fine-tune the angle to phase-match for the desired wavelength. The step size of the rotation stage is 0.12 mrad. The amplified seed pulse is then combined with the pump pulse used for the second stage of amplification by dichroic beamsplitter DC2. The first stage of amplification is expected to generate a significant of amount of mid-IR light; however, the UV fused silica substrate of dichroic beamsplitter DC2 is unable to transmit it for further amplification. All mid-IR light used for the 2D spectrometer is generated in the second stage of amplification.

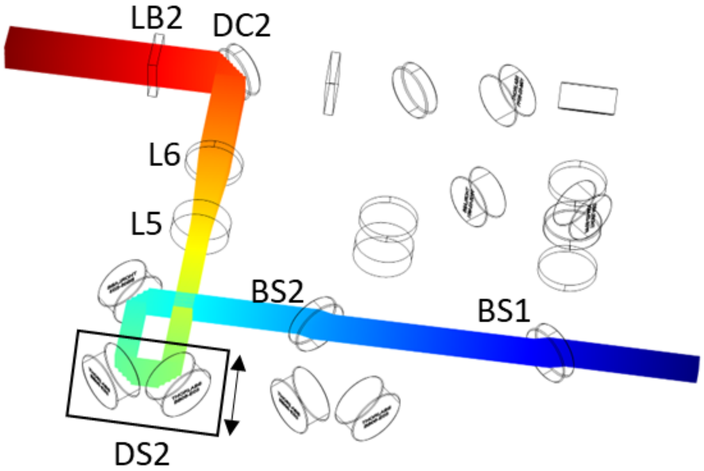

Figure 3.8. COMSOL Multiphysics raytracing simulation of the final stage of optical parametric amplification. The remaining 1.8 mJ of the 800 nm pulse transmitted through BS2 is reflected into delay stage DS2, which is used to control the timing of the pulse with respect to the seed pulse. The beam is then passed through a telescope composed of lenses L5 (f=-30 mm) and L6 (f=50 mm), before it is combined with the amplified seed pulse by dichroic beamsplitter DC2 and passed through lithium niobate crystal LB2 (2 mm thick, MgO:LiNbO3 (5% (by mol) MgO), Theta= 44.1°, phi=0°) for further amplification of the seed pulse with a center wavelength of 1040 nm, as well as the generation of the desired mid-IR pulse with a center wavelength of 3450 nm. Lithium niobate crystal LB2 is mounted on a custom-built motorized rotation stage (not shown) to fine-tune the angle to phase-match for the desired wavelength. The step size of the rotation stage is 0.12 mrad.

The OPA was designed around the layout of optics shown in Figure 3.6-Figure 3.8. Fusion 360 was used to model the optical mounts and body of the OPA as shown in Figure 3.9. The assembled OPA is shown in Figure 3.14 and Figure 3.15.The optical mounts were designed as separate pieces from the body to allow for small modifications to be made to the mounts without having to 3D print the entire body. This also provided some degree of adjustability of the mounts themselves for beam alignment. The mounts were designed around CAD models of the optics available from the manufacturer, Thorlabs. This allowed the mounts to have a tolerance small enough to firmly hold the optics in place without a set screw, reducing the overall size of the mount.

All of the delay and rotation stages contained in the OPA design were based around stepper motors, which allowed for them to be computer-controlled. This was done so that the tuning process could eventually be automated to find the optimal delays and angles to produce a range of frequencies of mid-IR pulses, and the 2D spectrometer could scan over a bandwidth much greater than is available within a single pulse.

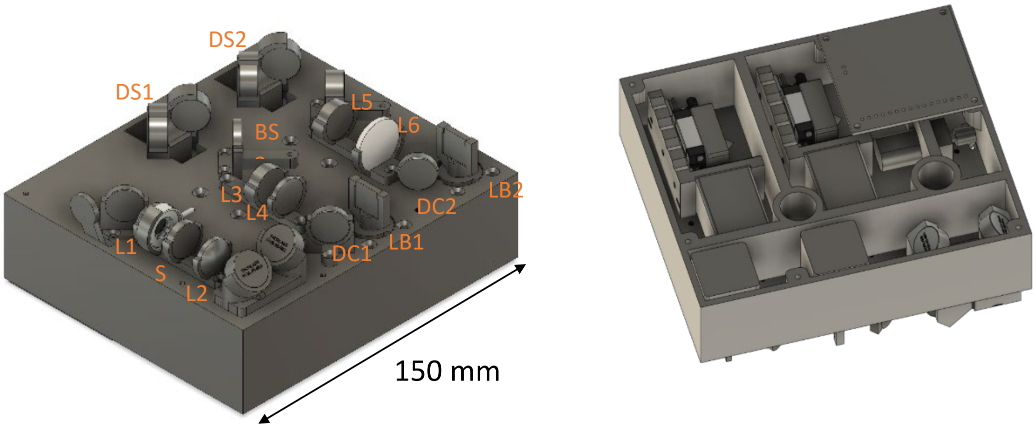

Figure 3.9. CAD model of the OPA designed in this work.

A translation stage (for Delay Stages DS1 and DS2) was designed to be integrated into the OPA while adding minimal additional optical path length to the OPA design. It was designed so all the mechanical components were mounted underneath the beam path, allowing for optics to be mounted over top of the motor. The design is shown in Figure 3.10.

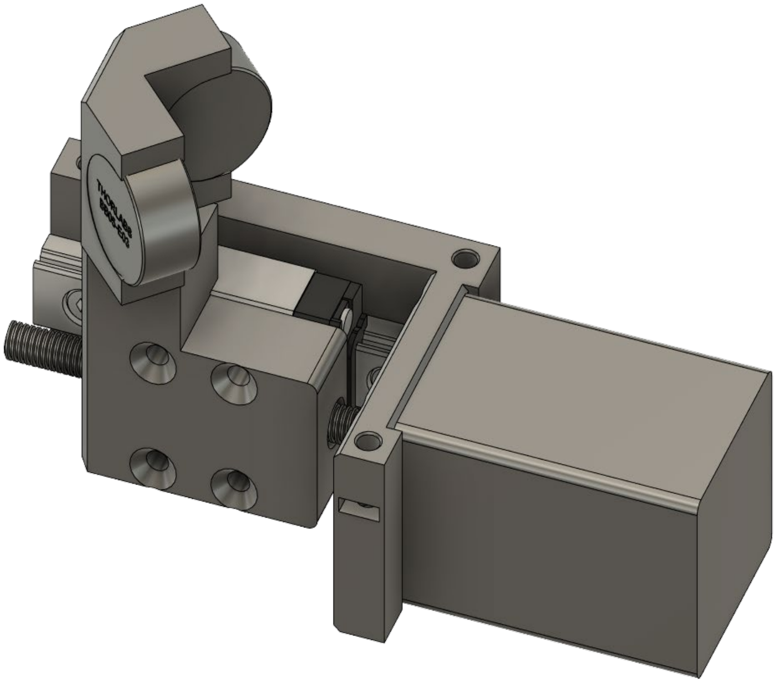

Figure 3.10. CAD model of delay stage used to delay the 800 nm pump pulses to overlap them in time with the pulses that they were used to amplify. The stage uses only two custom-made parts which can be printed with most stereolithography (SLA) 3D printers.

A control board was designed to control the translation and rotation stages. It was designed to be small enough to be mounted within the body of the OPA, with the only external connections being to a 12V power supply and a USB port of a computer. The stepper motor drivers used in the board are able to detect a stall condition based on the current the stepper motor consumed. The stall condition is not expected to cause excessive wear as only a small amount of current is being used even during the stall. This allowed for homing of the stages to be preformed by stalling them at their limit of travel, without relying on a limit switch, which reduced the complexity of the design of the stages. When a stall condition is detected, current to the motor is stopped, so there is an insignificant amount of heat dissipated and wear on the motors during this step. The was also able to control a shutter within the OPA to block the input beam.

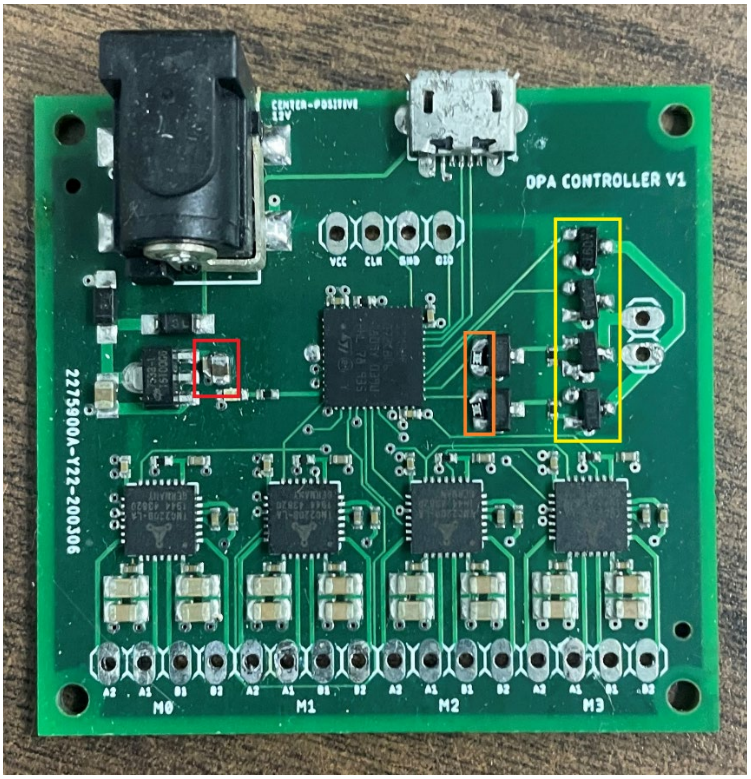

Figure 3.11. Control board designed for the 4 motion stages and shutter of the OPA. The PCB was fabricated and assembled by JLCPCB. The board contains 4 Trinamic TMC2209 stepper motor driver ICs and an H-bridge to drive the geared motor of the shutter. An STM32F0 series microcontroller provides a single USB interface to control all of the motors inside the OPA. A 10 μF capacitor (in red box) was added by hand to prevent the microcontroller from resetting due to the power surge caused by plugging in the 12V motor power supply. Pull-down resistors (in orange box) were hand-soldered to prevent a shoot-through condition which destroyed the MOSFETs of the H-bridge (replacement MOSFETs are in yellow box). The components were soldered with a soldering iron heated to 700 °C. They were held down with a flat-head screwdriver. The solder used was 63% Sn and 37% Pb with rosin flux core. The flux residue was cleaned with isopropanol and a toothbrush.

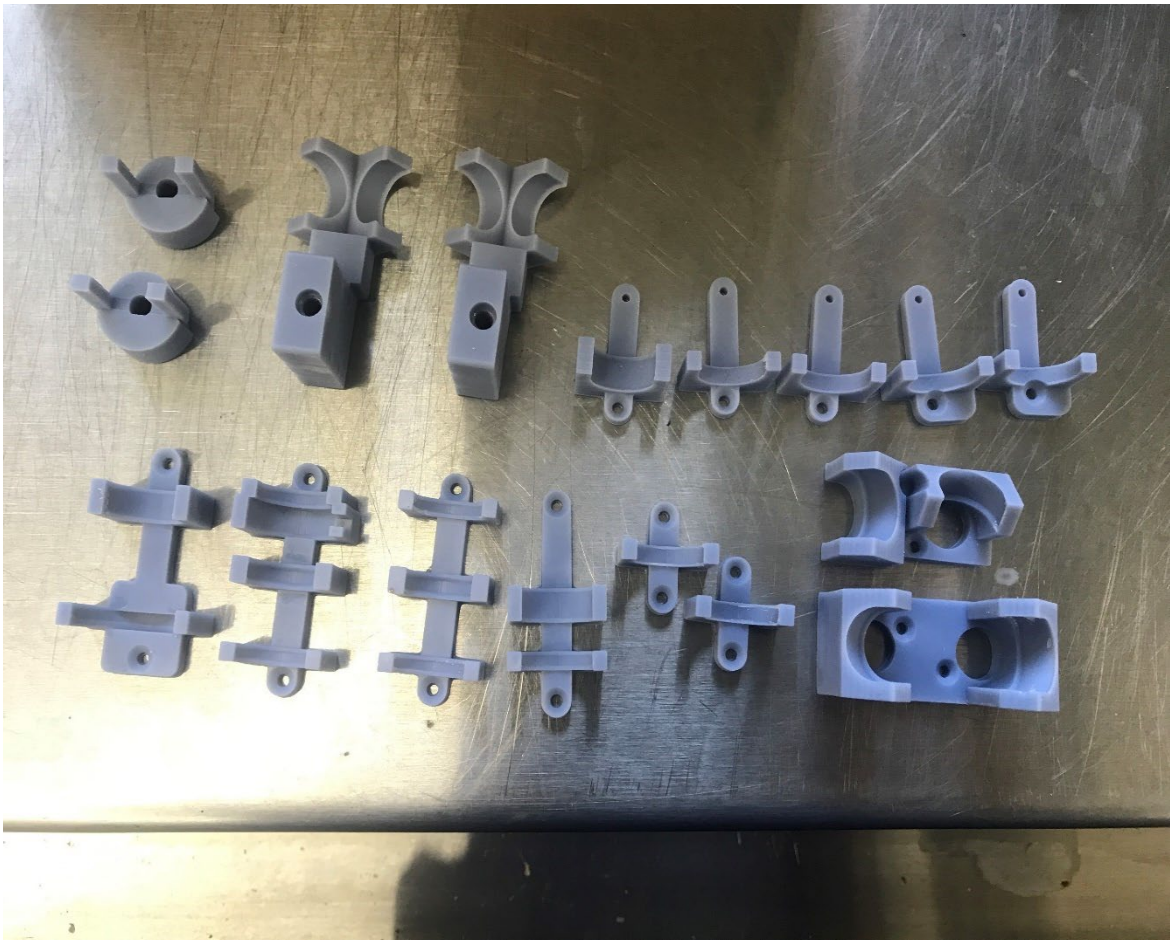

Figure 3.12. Picture of optical mounts used in OPA. All mounts were printed using a stereolithography (SLA) 3D printer (property of the author of this thesis). ELEGOO ABS-Like photopolymer resin was used (sourced from Amazon.ca). The printing process is depicted and described in Figure 3.13.

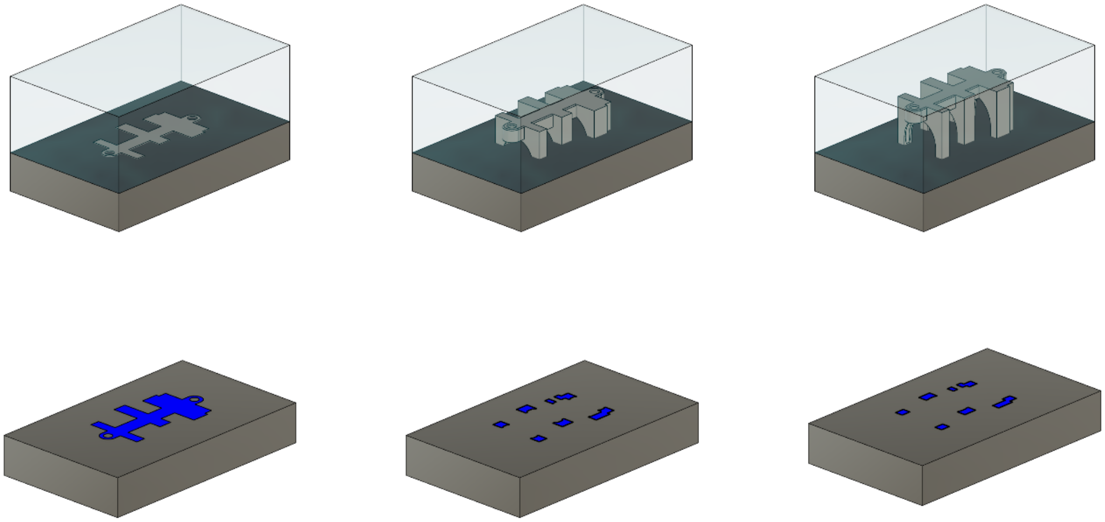

Figure 3.13. Stages of stereolithography (SLA) 3D printing an optical mount (top). Corresponding UV LCD exposure patterns (bottom). The resin is made up of epoxy acrylate resin, 1,6-Hexanediol diacrylate monomer, 1-hydroxycyclohexyl phenyl ketone photoinitiator and grey pigment. The photoinitiator produces radicals when exposed to UV light, which then react with the monomer to initiate polymer chain growth. The resin is exposed to UV light with an LCD screen at the bottom of the resin tank to selectively polymerize the resin at the base of the model against a metal build plate (not shown in figure). The build plate is then lifted with a motor to create space for another layer of resin to flow underneath the hardened layer, and is hardened in areas where material is desired in the model. This procedure is repeated to build the model by polymerizing the model in slices. The printed model is then cleaned in methanol to remove the residual resin, and is then left under a UV lamp to ensure the polymerizing is complete and the model is cured.

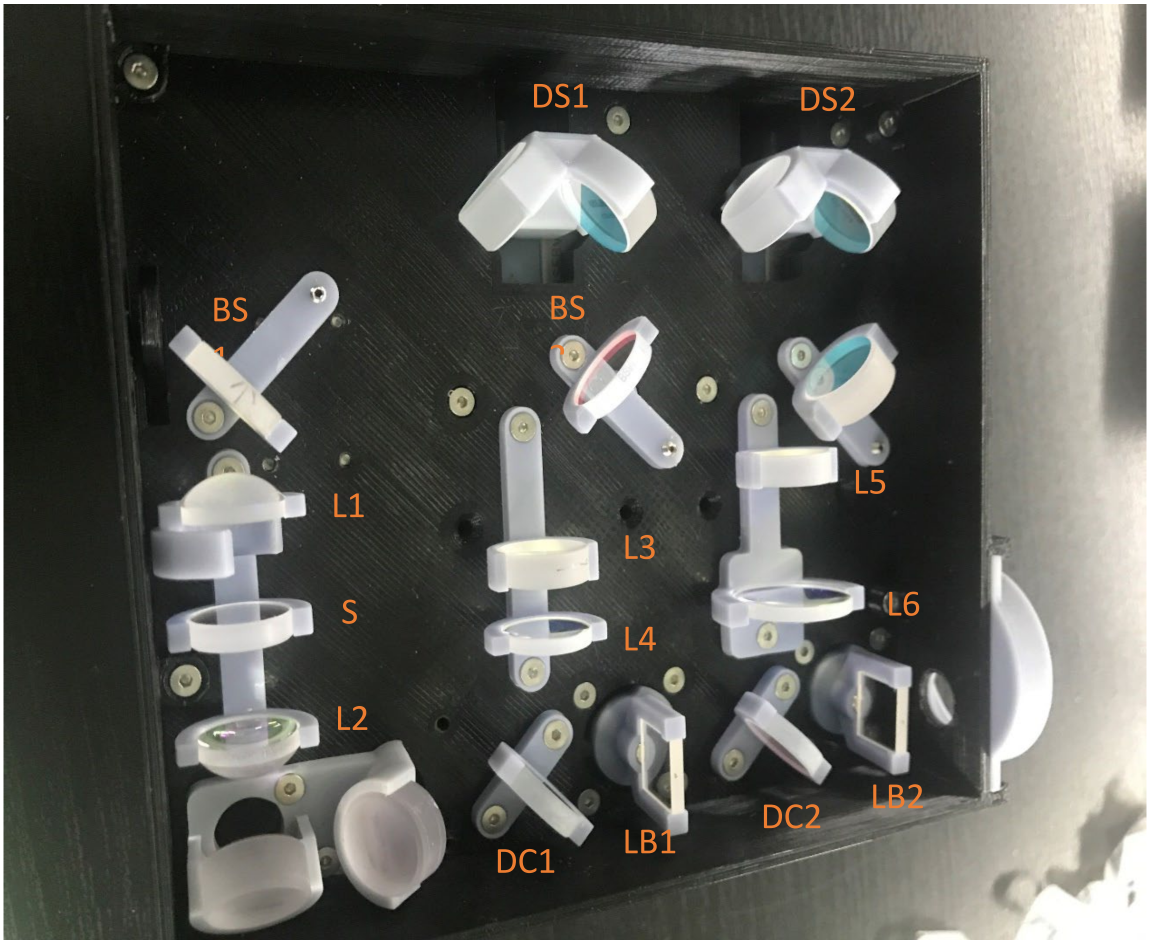

Figure 3.14. Picture of OPA assembled with optics (with cover removed). The black body of the OPA was printed using a fused deposition modeling (FDM) 3D printer. AMZ3D PLA 3D printer filament was used. The filament was fed through the printer with a motor, before being melted by the print head. The molten plastic hardened after being deposited at the desired locations in the model. There was no need to cure the model after printing.

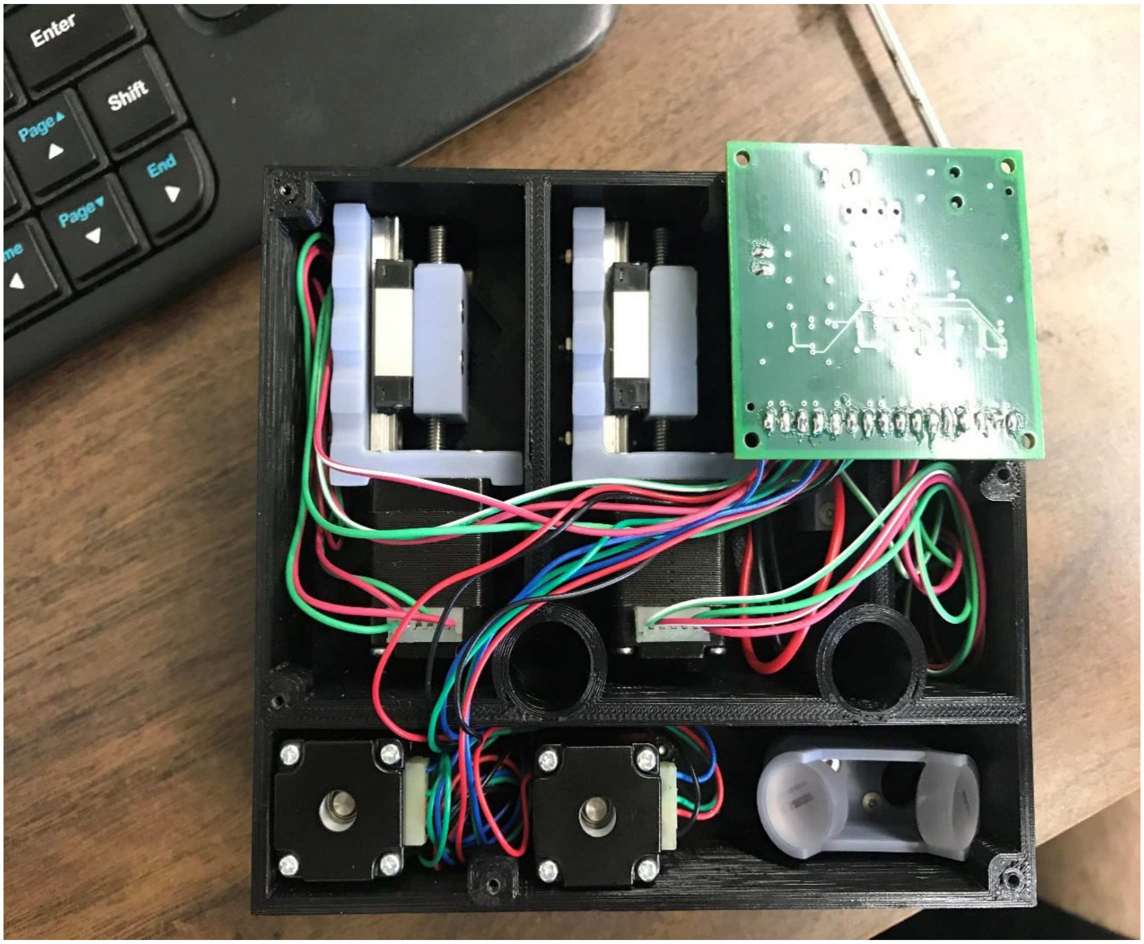

Figure 3.15. Picture of underside of assembled OPA (with cover removed) showing the translation and rotation stages used to move the optics and the control board.

The OPA described in this section was never implemented in the 2D spectrometer. The efficient generation of mid-IR pulses requires thorough characterization and tuning of each stage in the amplification process, which was found to be too difficult to accomplish within the size constraints of this OPA design. In hindsight, it would have been advisable to characterize and tune each stage in the amplification process separately on an optical table before combining them into as compact a space as possible. The motion control and optical mounts in the OPA work as intended, and could be of great value if the issues in the optical design are identified and addressed, which is beyond the scope of this thesis.

3.3 Spectral Manipulator

In order to enhance the resolution in probe frequency, for both the 2D spectrometer and conventional 1D measurements, a new spectral manipulator was built. This also improved the spatial mode of the laser beam, allowing for better overlap of the laser pulses on the sample and greater signal intensity. A diagram of the optical setup is shown in Figure 3.16. A picture of the constructed spectral manipulator is shown in Figure 3.17.

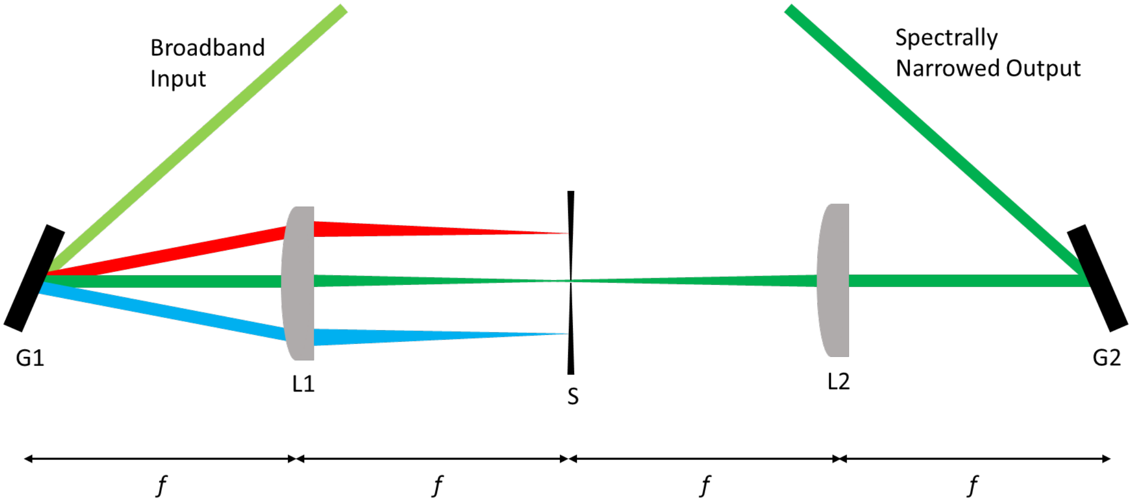

Figure 3.16. Diagram of spectral manipulator with bandwidth of broadband input exaggerated to demonstrate the dispersion of grating. The input beam is spectrally dispersed by grating G1. The spectrally dispersed light is then focused by lens L1 onto adjustable micrometer-controlled slit S, which blocks all but the desired wavelengths. The diverging light is then collimated by lens L2 and the spectral dispersion of grating G1 is reversed by grating G2. The focal length f of the lenses is 300 mm. Both gratings have a groove density of 2400 grooves/mm.

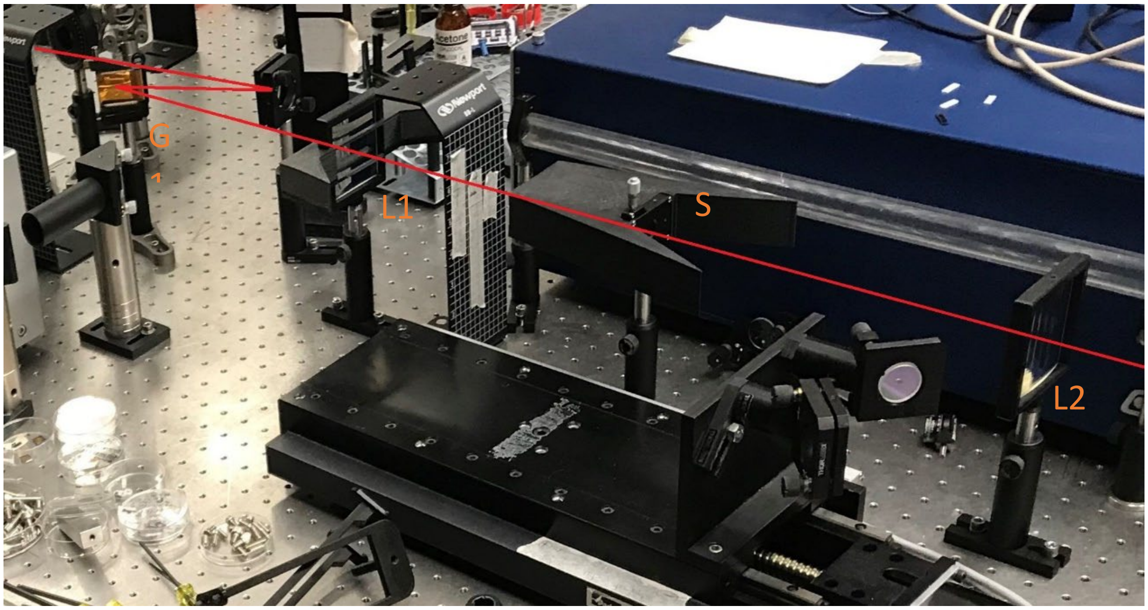

Figure 3.17. Picture of the constructed spectral manipulator. The beam path is shown in red. Grating G2 is not shown in the picture.

The spectral manipulator uses a $4f$ optical configuration where the distance between all the components is the same and equal to the focal length f of the lenses, with a total length of $4f$. The $4f$ configuration ensures that all wavelengths travel the same optical path length, allowing them to be recombined with the same relative phases as the input beam. A transform-limited pulse is a pulse which has the shortest possible duration in the time domain for a given bandwidth in the frequency domain. Recombining the wavelengths with the same relative phases allows for a transform-limited output pulse, given a transform-limited input pulse. While it is possible to use parabolic mirrors in place of lenses to avoid both spherical and chromatic aberrations, the use of lenses allowed for shorter optical path length, making it more suitable for the 2D spectrometer. The use of mirrors may be more appropriate where a larger bandwidth is allowed through the slit and the effects of spherical and chromatic aberrations from the lenses exceed those of the divergence and instability caused by the extra optical path length from using mirrors.

The lenses used were cylindrical and plano-convex. The use of cylindrical lenses allowed the beam propagation to remain unaffected by the spectral manipulator in the vertical direction; all manipulation happens in the plane of the optical table, being unaffected by misalignment normal to the plane and preventing further misalignment to be caused by the spectral manipulator. This also prevented the slit blades from burning due the light being focused in both directions, which was a problem with previous attempts to implement a spectral manipulator at SFU Chemistry. By not focusing the light in the vertical direction, the laser power available in the experiment is maximized by not having to use neutral density filters to prevent the slit burning. The use of plano-convex lenses reduced the effects of spherical aberrations compared with their convex alternatives. Lens mounts were designed and 3D-printed to hold and protect the lenses.

An alignment procedure was developed for the spectral manipulator. The first step was to correctly position the lens L2 shown in Figure 3.16. The gratings were replaced with mirrors and a neutral density filter was placed in front of the input beam to prevent the full power of the undispersed input beam being focused by lens L1. With the slit removed, the position of lens L2 was adjusted until the output appeared to be collimated after propagating approximately 10 m across the room. The second step was to correctly adjust the grating angles. The mirrors were replaced with the gratings and the neutral density filter was removed. The angle of grating G1 was adjusted so that the laser power measured at the position of the slit was maximized. Although changing the angle of grating G1 also changes the linear dispersion at the slit, optimizing for power at this position was still found to make the most intense wavelengths of light pass through the slit. The light was then allowed to propagate to grating G2 and the angle of grating G2 was adjusted until no dispersion was seen after propagating approximately 10 m across the room. It is important for the slit to be removed in this step, as a large bandwidth is required to see small errors in the angle of grating G2. The final step was to correctly position the slit along the beam axis. This was done by narrowing the slit to the minimum position where the output pulse spectrum could be measured by a UV-Vis spectrometer and adjusting the position of the slit so that the bandwidth of the output pulse was minimized.

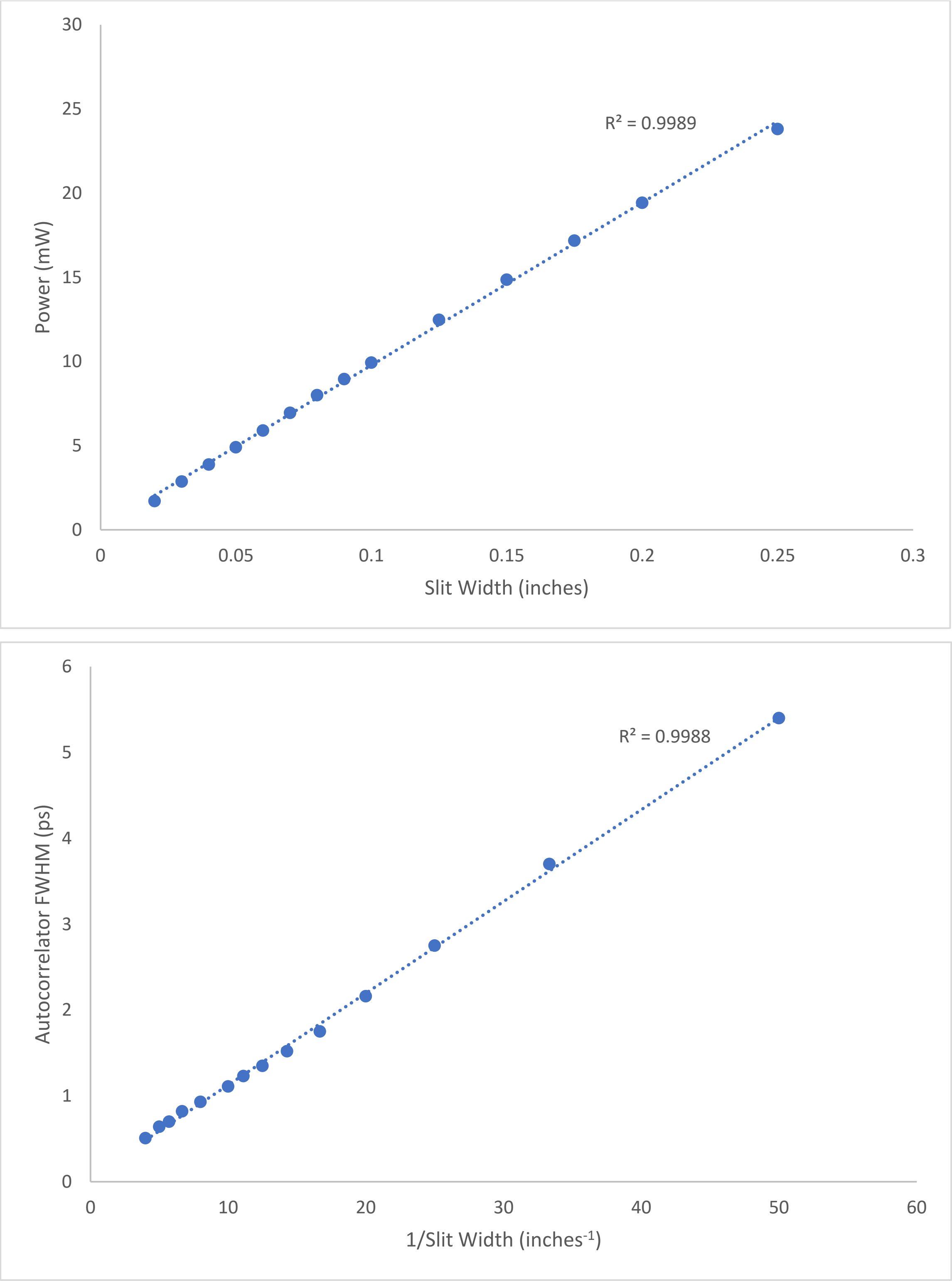

Figure 3.18. Spectrally narrowed output power as a function of spectral manipulator slit width (top). Autocorrelator FWHM measurements of spectral manipulator output as a function of reciprocal spectral manipulator slit width (bottom).

Figure 3.18 shows the characterization that was done on the output of the spectral manipulator. While Figure 3.18 (a) does not show the actual bandwidth of the output pulse, it does show that the output power is nearly proportional to the slit width, which indicates that the spectral manipulator is limiting the bandwidth of the output pulse and that the spectrum of the input pulse is nearly flat over the bandwidth making it through the slit for the slit widths used in these measurements. This was verified on a UV-Vis spectrometer, but the measurements were never recorded. Assuming that the slit width is proportional to the bandwidth of the output pulse, the linearity seen in Figure 3.18 (b) indicates that the output has a constant time-bandwidth product over the slit widths used in the measurements. It is suspected that a deviation from this linearity would be seen at greater slit widths due a shorter pulse being more easily lengthened by the dispersive optics in the beam path, but this could not be measured due to the physical limitation of the adjustable slit used. The slit used was Thorlabs VA100. The maximum slit width is 0.24”, which is substantially more than would be expected to ever be used in taking SFG measurements.

3.4 Dual-stage Michelson Interferometer

In order to control the timing of the pulses required for 2D SFG-VS, a novel adaptation of the Michelson Interferometer, typically used in FTIR spectrometers, was designed and constructed. It uses two moving mirrors to control both the relative time delay τ and the absolute time delay T, which reduces the number of optics used and the pathlength compared to the typical method of using a separate delay stage to control T as shown in Figure 3.19. The layout of the dual-stage Michelson interferometer, used in the 2D SFG-VS spectrometer presented in this work, is shown in Figure 3.20.

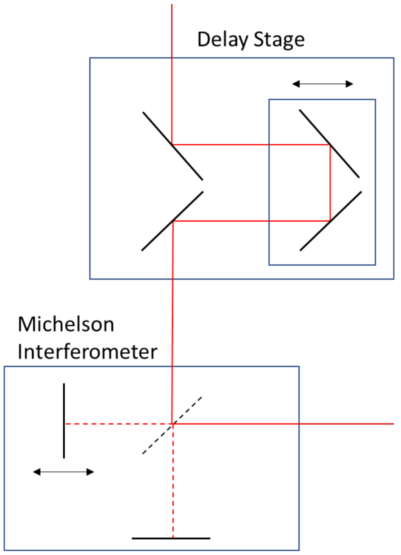

Figure 3.19. Typical layout of setup used to control time delays in a 2D SFG-VS spectrometer.

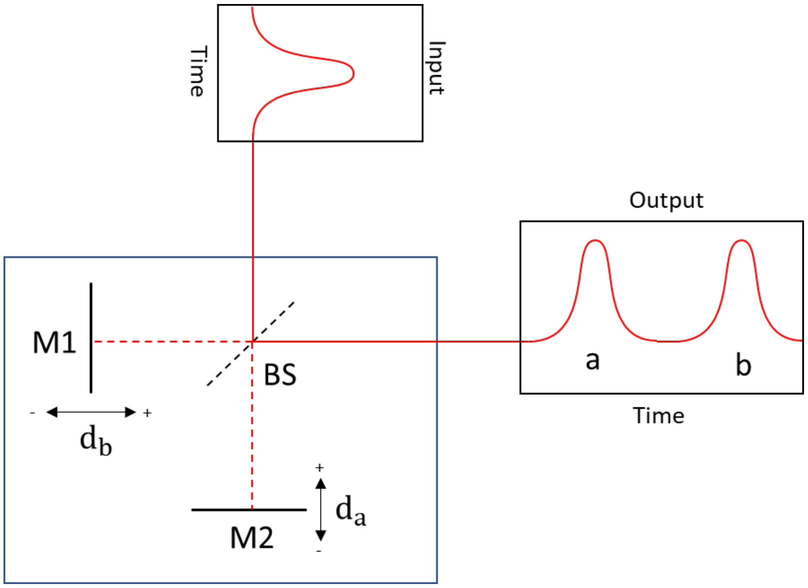

Figure 3.20. Layout of the dual-stage Michelson interferometer described in this section. Field amplitudes as a function of time are illustrated for the input and output, with labels “a” and “b” corresponding to the pulses which were reflected off Mirrors M1 and M2 respectively. Beamsplitter BS is a pellicle beamsplitter (Thorlabs BP145B4) with a thickness of approximately 2 μm, which splits the input beam into two beams of approximately equal intensity. The beamspitter is made from nitrocellulose and works with light of wavelengths between 3 and 5 μm. Mirrors M1 and M2 are protected gold mirrors (Thorlabs PF10-03-M01).

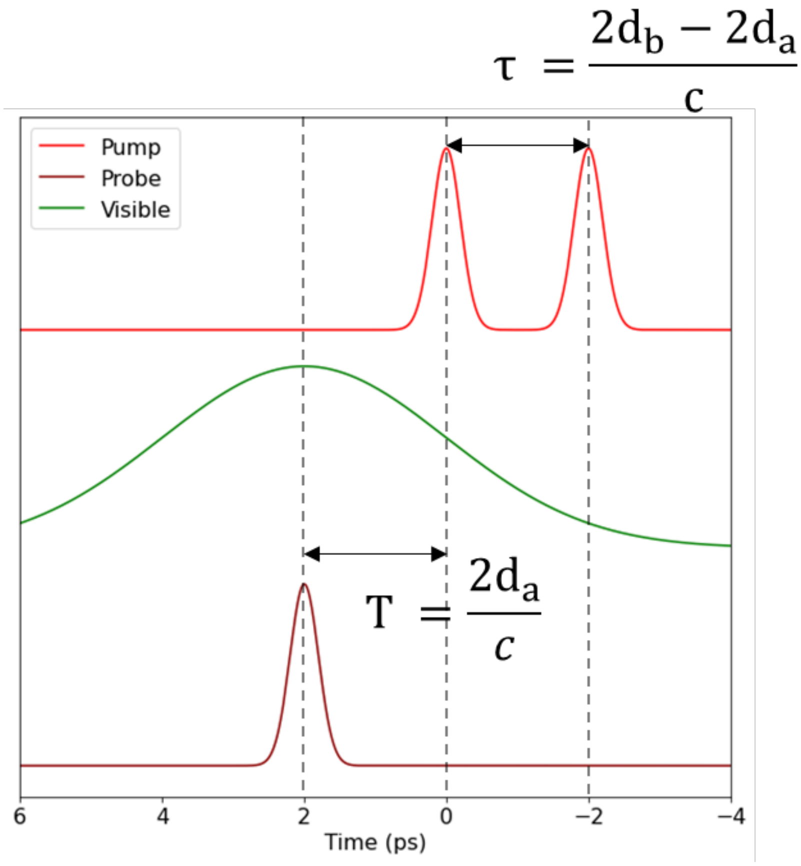

Figure 3.21. Diagram of pump pulses in frame with the other pulses used in the 2D spectrometer. The relative time delay τ and the absolute time delay T are given in terms of the distances the mirrors travel in Figure 3.20, where c is the speed of light.

As shown in Figure 3.21, τ is dependent on the position of both stages, which requires both stages to be calibrated to accurately control τ. A calibration procedure to calibrate both stages interferometrically was developed and is described in the later Section 3.6.2 .

A pellicle beamsplitter was chosen to split the pump into two pulses. It is approximately 2 µm thick. This eliminates ghosting according to the manufacturer (Thorlabs), and should minimize dispersion due to its minimal thickness. While a cube beamsplitter could be used to match the dispersion added to both pulses, it would still lengthen the ultrashort infrared pulses used in the 2D spectrometer, which would cause the time delays to be less defined.

An adjustable mount for the beamsplitter was available from Thorlabs, but it would obstruct part of the beam path when installed in the interferometer. To overcome this, a custom mount was designed in Fusion 360 CAD software. The mount utilized part of an adjustable mount from Thorlabs. Thorlabs makes CAD models available for most of their products, making it straightforward to design around them. The CAD model of the mount used in the 2D SFG-VS spectrometer is shown in Figure 3.22. The mount has three adjustment screws, giving two angular degrees of freedom and one translational degree of freedom. The translational degree of freedom was used to maximize the beam path that could pass through unobstructed by the edges of the beamsplitter. The CAD model was 3D printed and the mount was assembled as shown in Figure 3.24.

Figure 3.22. CAD model of adjustable beamsplitter mount. Only the grey component holding the beamsplitter was designed in this work. The other components, including the beamsplitter, were taken from CAD models available from Thorlabs. Fusion 360 CAD software was used.

In order for the data collected using the interferometer to give spectral resolution of pump wavenumbers, the relative time delay τ needs to be incremented the same or less than half of the minimum period of pump infrared light. This requirement is set by the Nyquist theorem[30]. The maximum expected pump frequency for the 2D spectrometer is approximately 100 THz, which has a period of 10 fs; therefore, τ must be sampled at most every 5 fs. This corresponds to a mirror displacement of just 0.75 μm. While this is the maximum step size of the motion stage in the interferometer while scanning τ, the accuracy of the stage needs to be much better than this in order to sample the oscillations in the interferogram with the correct phase. This requirement applies only to one of the two motion stages in the Michelson interferometer as the other stage is kept stationary when τ is being scanned.

Though not a requirement, identical stages were used for both arms of the interferometer, in order to simplify the design and interface. The stages were Newport MFA-CCs. Their specifications suggest they are suitable for the 2D spectrometer; with a minimum incremental movement of 100 nm, encoder step size of approximately 18 nm, and a typical unidirectional repeatability of ±80 nm; however, the CONEX controller included with them could only control the position of the stages to 1 μm. For that reason, a new controller was designed and built for both stages, and is described in the next section.

Before the interferometer was constructed, it was modelled in Fusion 360 CAD software[31]. This allowed for a design with minimal spacing between the beamsplitter and moving mirrors while ensuring nothing collides when both interferometer arms are at their shortest position. The adjustable beamsplitter mount was also designed within this model to ensure it would not obstruct the motion stages over their range of travel. A cover was designed to protect the pellicle from dust and to block air currents within the room causing small variations to the optical path length difference between interferometer arms. The full CAD model is shown in Figure 3.23. The assembled interferometer is shown in Figure 3.24.

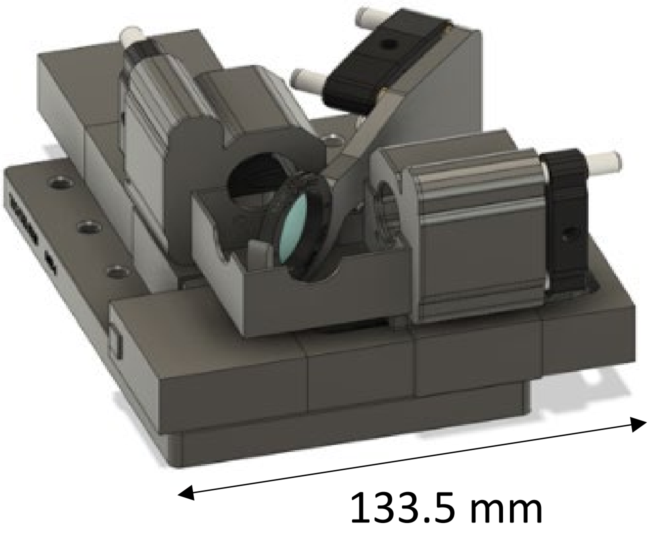

Figure 3.23. CAD model of the assembled interferometer. Fusion 360 CAD software was used.

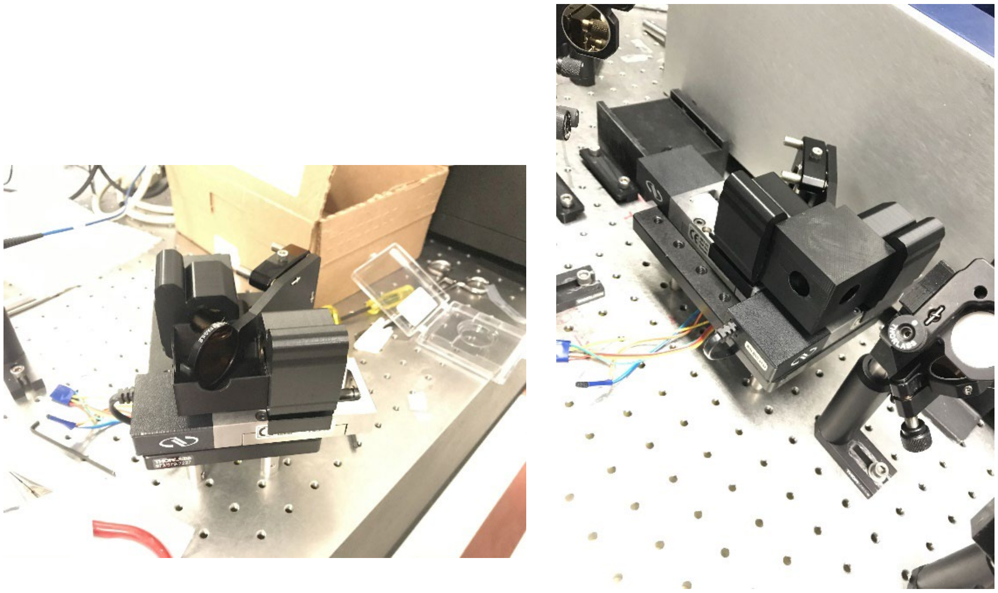

Figure 3.24. Constructed interferometer with pellicle beamsplitter exposed (left) and covered (right). The interferometer was raised with 4 1” thick pedestal posts, which were bolted to the optical table to dampen vibrations from the movement of the motion stages. The vibrations would not cause noise in the signal, due to the stages being stationary when data is acquired; they would only affect the positioning of the stages when they are moving.

3.5 Motion Controller

Due to the nature of the signal and detection, moving mirrors could not be used during acquisition, so a custom motion controller was designed and constructed to accommodate for the small step size required to perform interferometry with IR light, as discussed in the previous section. The controller was designed around an STM32G4 series microcontroller, which provides a direct encoder interface and digital-to-analog converter (DAC).

3.5.1 Hardware

The physical design of the motion controller was simple. It consists of three integrated circuits: the microcontroller, a dual operational amplifier (motor driver), and a voltage regulator the microcontroller. Due to the simplicity of the design, a schematic was never made. The PCB was designed directly in Eagle EDA software.[24] It was built to order by JLCPCB PCB fabrication house.[25] The components were hand-soldered with a soldering iron heated to 700 °C. The solder used was 63% Sn and 37% Pb with rosin flux core. The assembled PCB is shown Figure 3.25. Two PCBs were assembled for each stage in the dual-stage Michelson interferometer described in the Section 3.2 .

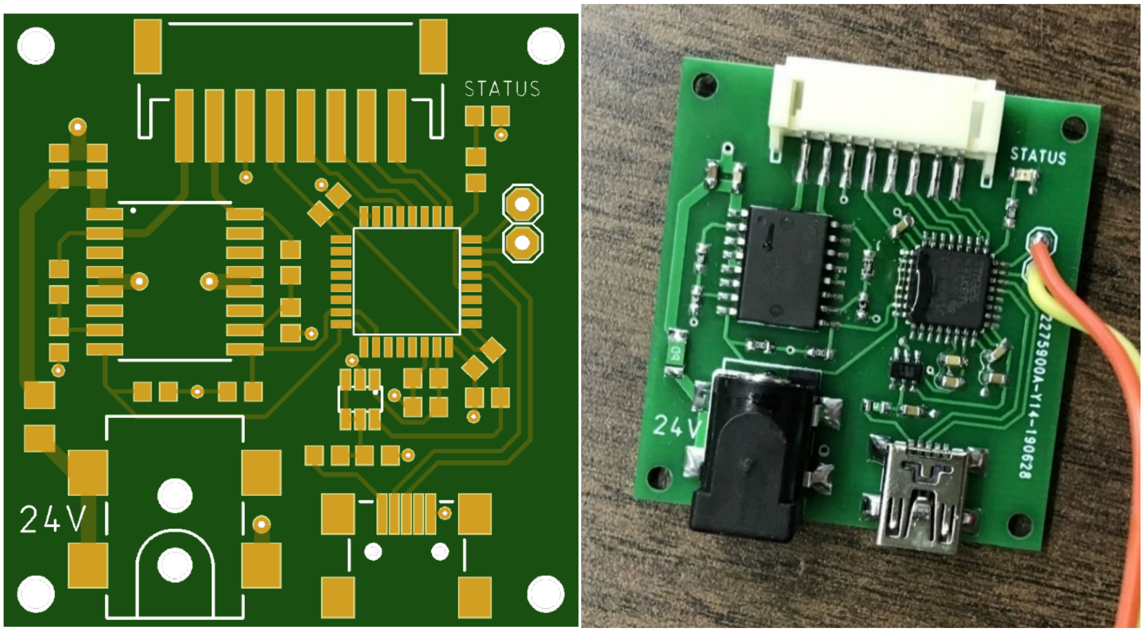

Figure 3.25. Motion controller PCB design (left). Hand-soldered motion controller PCB (right).

The majority of the hardware design of the motion controller lies in the configuration of the hardware within the microcontroller, which is done by its firmware. The firmware was developed using STM32Cube initialization code generator[32] for the initial configuration of the hardware peripherals in the microcontroller, and Arm Keil MDK (Microcontroller Development Kit)[33] to write and compile the code. Figure 3.26 shows how the components within the microcontroller interconnect and how they interact with the rest of the controller and motion stage.

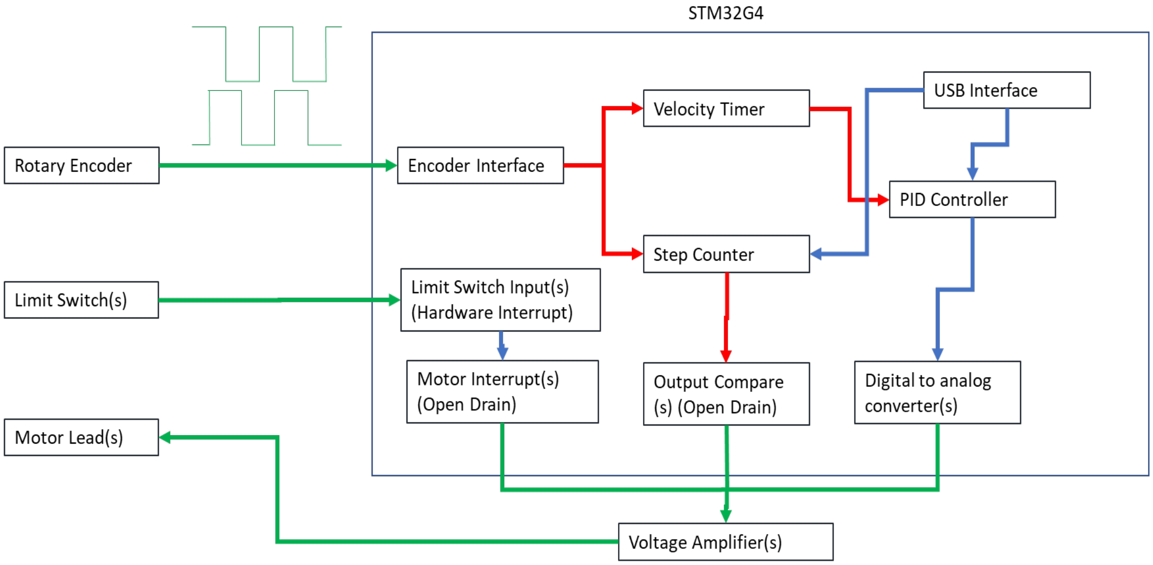

Figure 3.26. Signal flow diagram of motion controller. Off-chip connections are in green. Hardware connections are in red. Software-mediated connections are in blue.

The design of the controller relies heavily on the integrated peripherals of the STM32G4 series microcontroller. All of the time-critical signals pass through hardware connections between the peripherals, enabling for a FPGA-level response time[†], despite being based on a microcontroller.

At every change of the encoder position; the velocity timer is captured and reset, and a hardware interrupt is triggered to allow the PID controller to adjust the motor voltage according to the latest velocity timer capture. The velocity timer is 16-bit and has a clock frequency of 160 MHz. The linear velocity v of the stage can be given by

---

[†] FPGAs tend to have a faster response time than microcontrollers due to its operation not relying on instructions which can take multiple clock cycles to execute.

$$\mathrm{v} = \frac{\mathrm{d\,f}}{\mathrm{n}}, \tag{3.1}$$

where d is the step size, n is the timer count, and f is the clock frequency. According to the equation above, the slowest velocity that could be recorded without the 16-bit timer overflowing[‡] is approximately 0.05 mm/s, which is too fast for the stage to stop consistently at the target position. To circumvent this limitation; a second 16-bit timer was used, with a counter incremented every time the first timer overflowed. Both timers are captured in hardware simultaneously, eliminating the possibility for an overflow to occur between captures. Together the timers can measure velocities as low as 7e-7 mm/s, enabling the target approach velocity of 0.02 mm/s to be used to allow the stage to stop consistently at the target position.

When the stage is moving, the step counter is compared in hardware to the target position set by the USB interface. When the target position is reached, the input of the voltage amplifier driving the motor is pulled to ground by the output compare of the step counter, pulling its output to ground and halting the motor. While the voltage amplifier is unable to respond instantaneously, it should respond consistently to its input being shorted to ground. No software is involved in the process of stopping the motor, allowing for a fast and consistent response of the motion controller. This could be verified using an oscilloscope; however, the performance of the motion controller did not present the need to.

3.5.2 Software

An early attempt at the controller was made using a simple PID loop to maintain the velocity of the stages until the target position was reached. It was found that the velocity readings were spurious when they were not averaged over multiple steps. Averaging over multiple steps was not viable to maintain a velocity that was slow enough to maintain control while not stalling the motor.

The spurious velocity readings were found to be periodic with the number of rotary encoder positions, indicating that the spurious readings were due to manufacturing defects in the encoder. An iterative algorithm was developed to determine the correction factors that had to be applied to each encoder position to compensate for the manufacturing defects. The algorithm had to be iterative in order to prevent true changes in velocity from

---

[‡] Overflow is a condition where the memory register of the counter cannot hold the value of the counter so it resets the memory register to zero.

influencing the correction factors. By scanning over the same rotary encoder positions, but over different linear positions of the motion stage in each scan, the effects of the variable linear resistance over the motion range were averaged out, by only making incremental adjustments to correction factors that would not completely account for the variation in velocity in a single scan.

Applying correction factors to each encoder position meant that, in order for the correction factors to still be valid, the stage needed to be homed to the same encoder position after power was lost. The limit switches could not be relied upon to home the stage to the same encoder position every time; there was a variability of approximately 15 steps, which is even less variation than is reported by the manufacturer of the stage. The variability was measured by moving the stage to trigger the limit switch, while retaining the original homing position reference of the encoder. A homing procedure was developed that used the spurious velocity readings produced from the manufacturing defects as a fingerprint of the encoder. Examples of this fingerprint are shown in Figure 3.27.

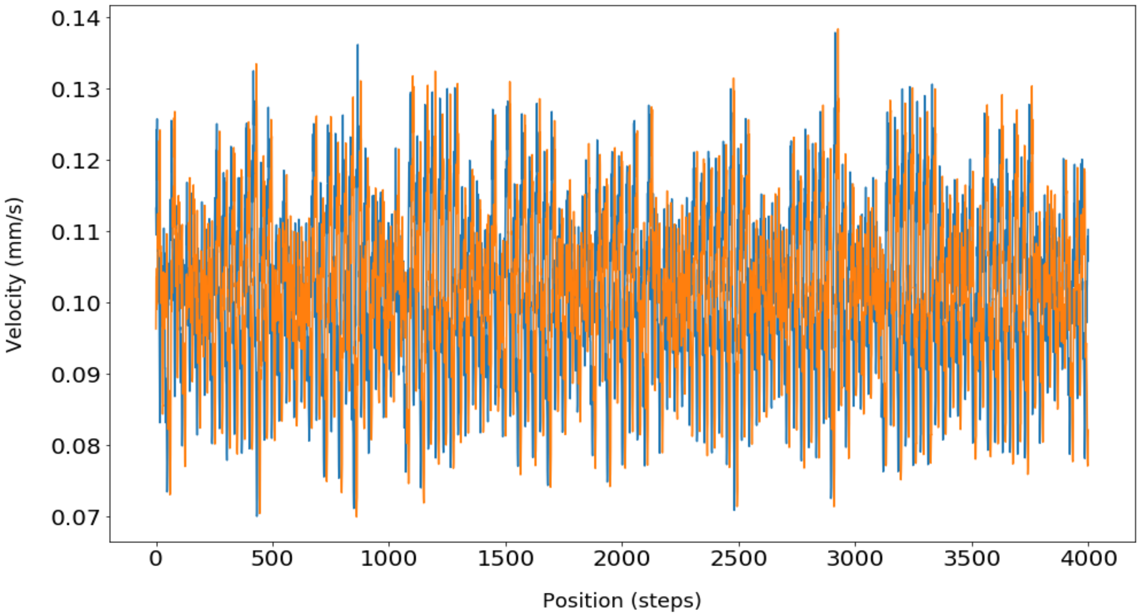

Figure 3.27. Reported velocity vs. reported position of stage. The motion controller’s target velocity was 0.1 mm/s over the scan. The two colours correspond to data that was collected after being homed to different positions.

Any unknown offset in the homing position of the stage could be found by taking the cross-correlation of the fingerprint with the current homing and the previous homing. The highest peak in the cross-correlation corresponds to the offset. An example is shown in Figure 3.28.

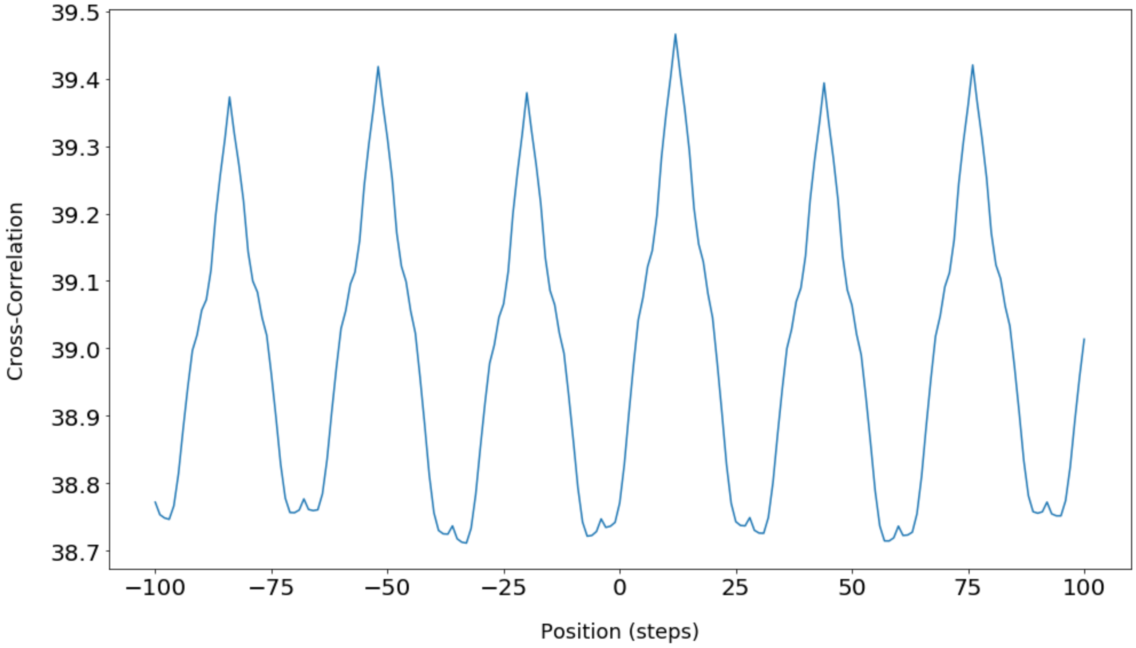

Figure 3.28. Cross-correlation of the scans in shown in Figure 3.27. Details about the type of cross-correlation used are provided in Appendix B.

This homing procedure allows the correction factors to be used between homing sequences, which saves time in day-to-day use. The homing procedure is automated by the GUI developed for the spectrometer and can be initiated by the press of a button. It was observed that the correction factors were no longer valid after long periods of time when the system was not in use. It is suspected that this could be caused by oil settling in the stages drive mechanism. For these cases, the procedure to find the correction factors has also been automated and integrated into the GUI. The procedure can find the correction factors directly without any initial assumptions, but it is much quicker if it can use previous correction factors as a starting place.

3.6 Calibration

In order to ensure that the spectrometer reports the correct time delays and wavenumbers, a set of calibration procedures was developed. The calibration of pump frequency and time delays is done after the calibration of the UV-Vis spectrometer as it uses the spacing in SFG frequencies as a reference. A GUI was developed to allow users to easily calibrate the spectrometer with minimal technical knowledge. The GUI was developed solely by the author of this thesis.

3.6.1 UV-Vis Spectrometer: SFG Frequency

The first step in the calibration is to calibrate the UV-Vis spectrometer used to measure the SFG signal. All of its calibration was done using the 632.8 nm output of a helium-neon laser. The grating in the spectrograph was moved and the spectrum of the helium-neon laser was recorded on the CCD, with the x-axis being pixel position, over a range of grating positions. An example of a spectrum collected at one grating position is shown in Figure 3.29. The single peak was moved across the CCD as the grating angle was changed. A complete dataset for the scan of a single grating (and diffraction order) is plotted in Figure 3.30.

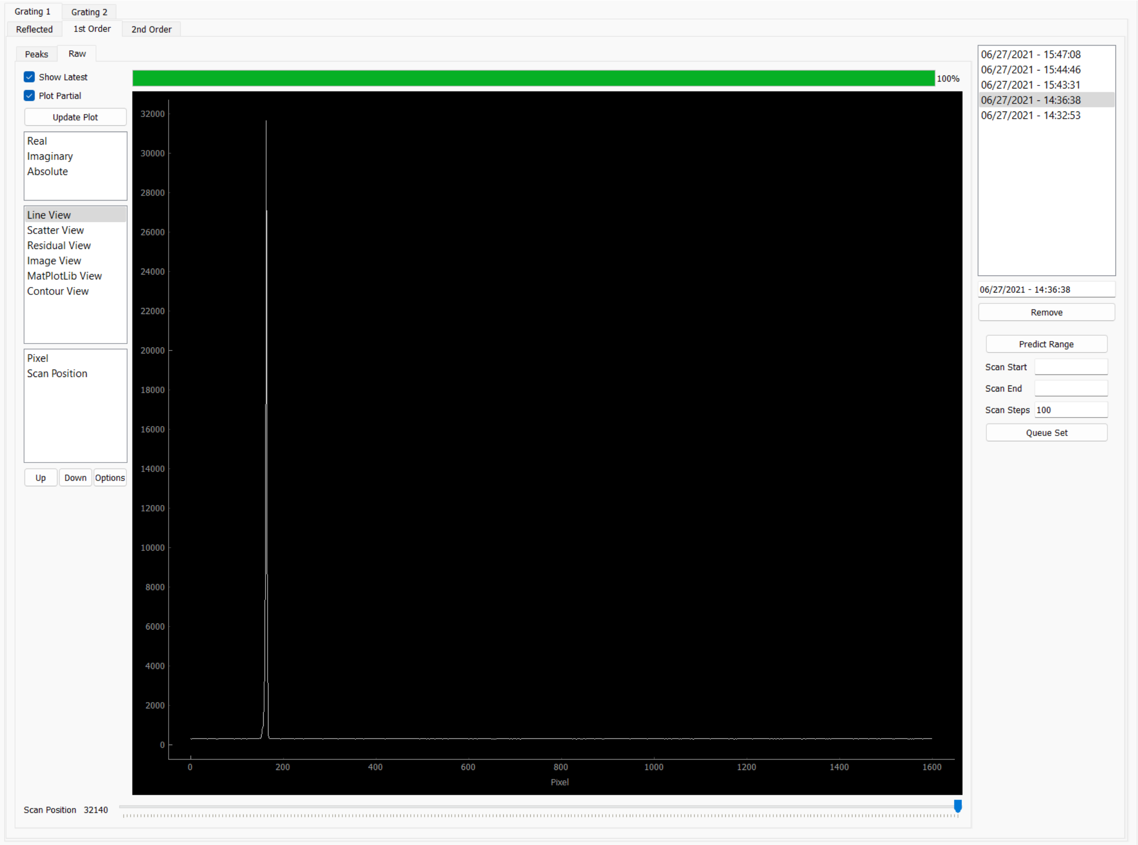

☑ Show Latest
☑ Plot Partial

06/27/2021 - 15:47:08
06/27/2021 - 15:44:46
06/27/2021 - 15:43:31
06/27/2021 - 14:36:38
06/27/2021 - 14:32:53

06/27/2021 - 14:36:38

Scan Start
Scan End
Scan Steps 100

Scan Position 32140

Figure 3.29. GUI displaying the spectrum of 632.8 nm light in terms of pixel position on CCD. The slider on the bottom can select whichever grating position is in the scan data set.

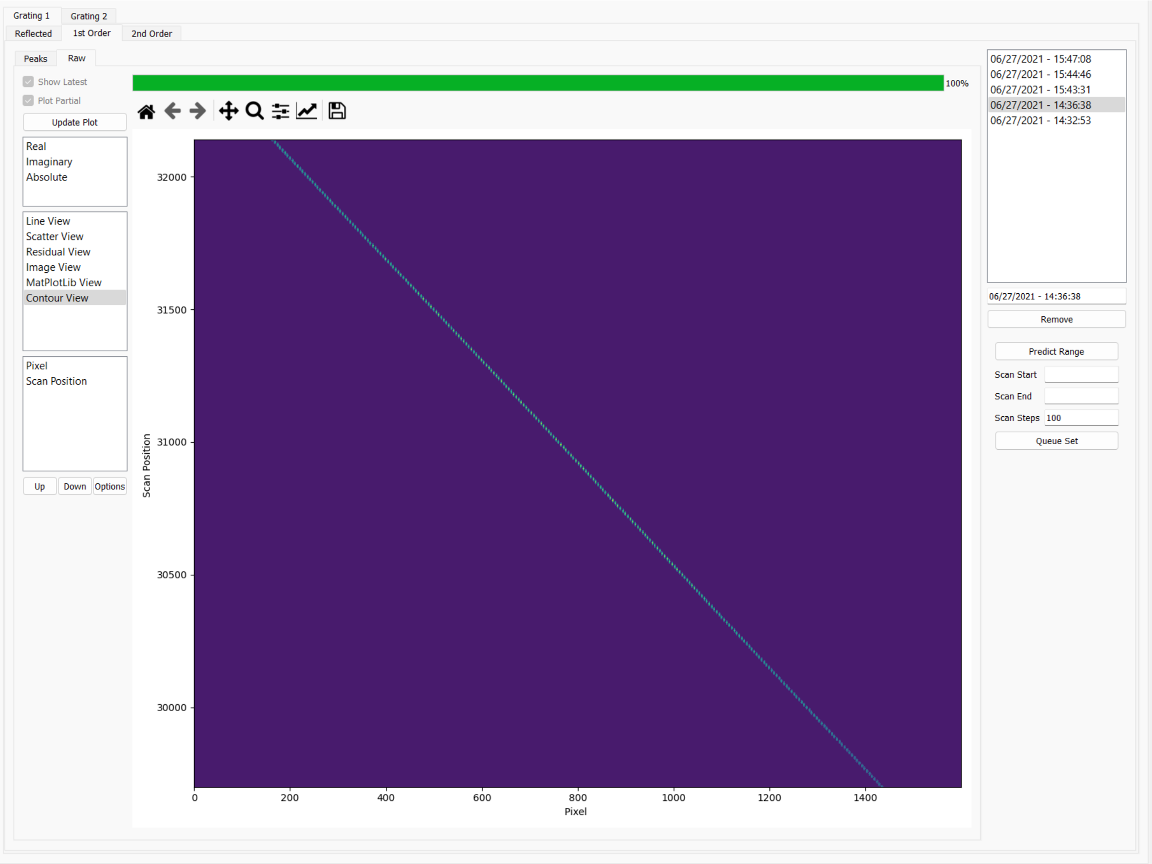

06/27/2021 - 14:36:38

Scan Steps 100

Figure 3.30. GUI displaying a contour plot of a series of spectra produced from a range of grating positions.

The GUI was made to extract the pixel position on the CCD where the peak was for every grating scan position by taking the pixel of maximum intensity, reducing the two-dimensional data to one-dimensional data. This is shown in Figure 3.31. The GUI is used to fit this data to calibration parameters that could be used to determine the wavelength of light hitting each CCD pixel for a given grating position.

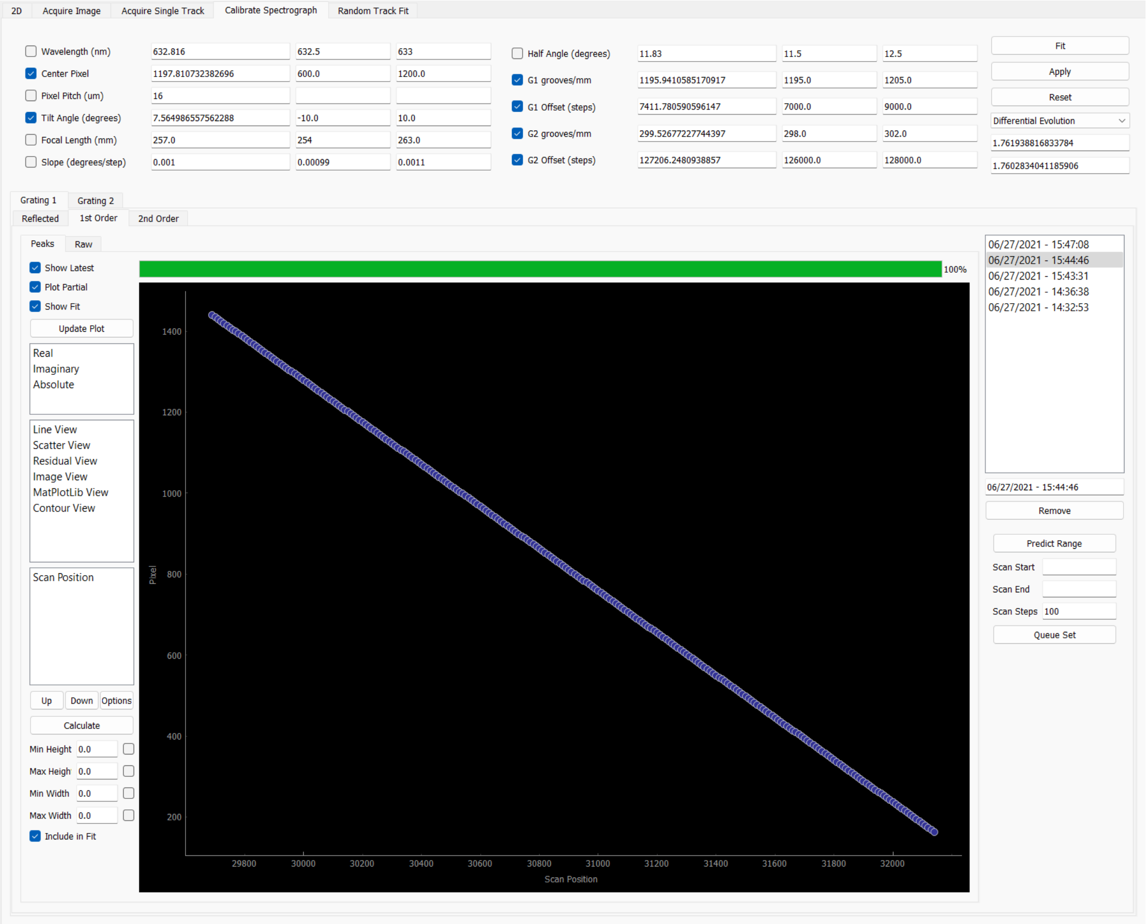

☐ Wavelength (nm)	632.816	632.5	633
☑ Center Pixel	1197.810732382696	600.0	1200.0
☐ Pixel Pitch (um)	16		
☑ Tilt Angle (degrees)	7.564986557562288	-10.0	10.0
☐ Focal Length (mm)	257.0	254	263.0
☐ Slope (degrees/step)	0.001	0.00099	0.0011
☐ Half Angle (degrees)	11.83	11.5	12.5
☑ G1 grooves/mm	1195.9410585170917	1195.0	1205.0
☑ G1 Offset (steps)	7411.780590596147	7000.0	9000.0
☑ G2 grooves/mm	299.52677227744397	298.0	302.0
☑ G2 Offset (steps)	127206.2480938857	126000.0	128000.0

Differential Evolution

1.761938816833784

1.7602834041185906

☑ Show Latest
☑ Plot Partial
☑ Show Fit

Min Height 0.0 ☐
Max Heigh 0.0 ☐
Min Width 0.0 ☐
Max Width 0.0 ☐
☑ Include in Fit

06/27/2021 - 15:47:08
06/27/2021 - 15:44:46
06/27/2021 - 15:43:31
06/27/2021 - 14:36:38
06/27/2021 - 14:32:53

06/27/2021 - 15:44:46

Scan Start
Scan End
Scan Steps 100

Figure 3.31. GUI displaying extracted peak position on CCD as a function of spectrograph grating position. The residuals are too small to see the fit line. Possible fitting parameters and their bounds are at the top of the window. Only the parameters that are checked are allowed to change when fitting.

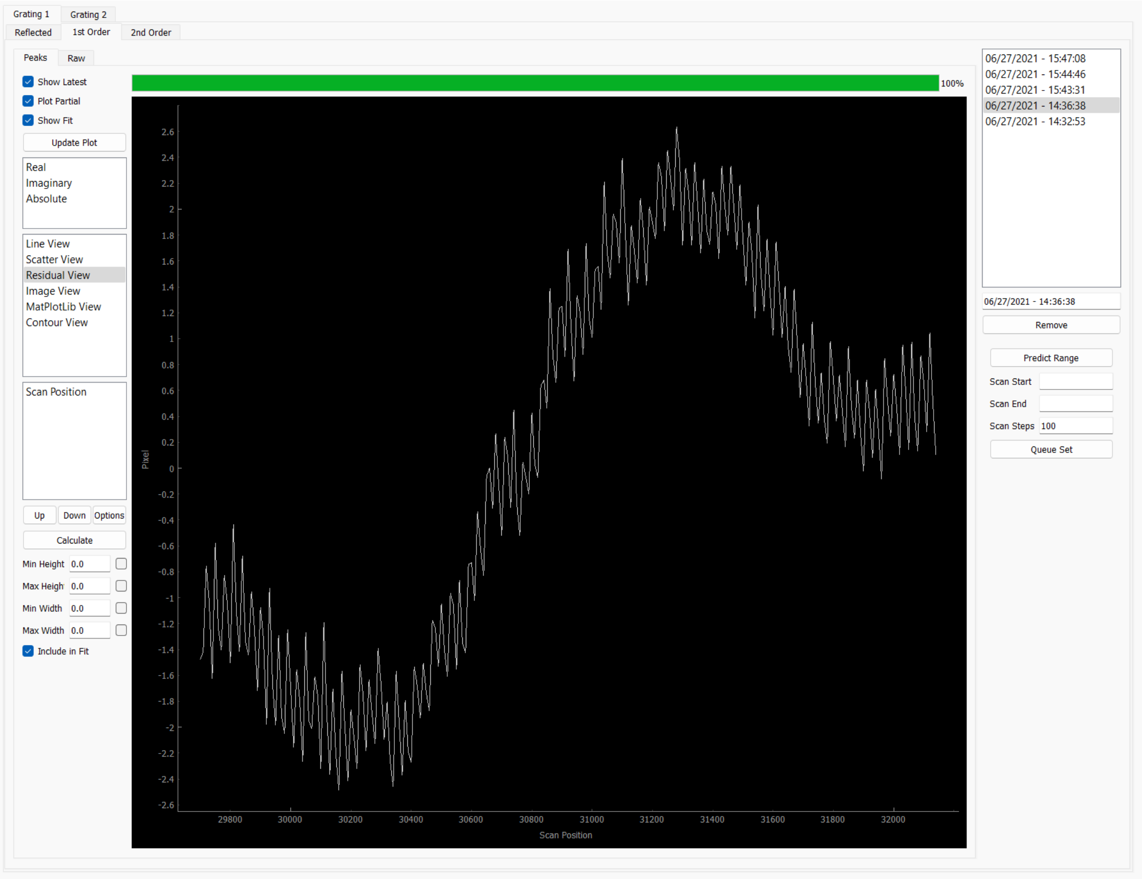

☑ Show Latest
☑ Plot Partial
☑ Show Fit

Min Height 0.0 ☐
Max Heigh 0.0 ☐
Min Width 0.0 ☐
Max Width 0.0 ☐
☑ Include in Fit

06/27/2021 - 15:47:08
06/27/2021 - 15:44:46
06/27/2021 - 15:43:31
06/27/2021 - 14:36:38
06/27/2021 - 14:32:53

06/27/2021 - 14:36:38

Scan Start
Scan End
Scan Steps 100

Figure 3.32. GUI displaying residuals of fit shown in Figure 3.31. The residuals are on 1/1000 level.

The calibration of the spectrometer was not limited to scanning the first-order diffraction from the grating. The zeroth-order reflection and second-order diffraction could also be scanned. The use of these scans in fitting the calibration parameters leads to much more confidence that the calibration is valid over a much larger bandwidth than is captured by the CCD in a single spectrum. The GUI predicts the proper scan ranges based on the current calibration parameters. The also GUI allows an arbitrary number of datasets to be fit simultaneously. Scans from multiple gratings can be fit simultaneously in the GUI so that the calibration parameters that do not depend on the gratings are consistent between gratings when they are changed. This also increases confidence in these parameters, as they are fit to a more diverse set of data.

3.6.2 Pump Frequency and Relative Time Delay τ

The calibration of the time delay between pump pulses, referred to as relative time delay τ, is necessary both to determine the pump wavenumbers and to control the dual-stage Michaelson interferometer described in the Section 3.4 . A calibration procedure was developed to determine τ interferometrically.

If a non-resonant sample is used to produce SFG, the spectrum of the SFG is primarily determined by the light used to create it. When there is a time delay between the infrared pump pulses used in the 2D SFG-VS spectrometer, there is an interference pattern in the infrared spectrum, with a fringe frequency that is proportional to τ. When SFG is produced with this interference pattern in the infrared spectrum and narrow-bandwidth 800 nm light on a non-resonant sample, the same interference pattern is seen in the SFG spectrum with its frequency increased by the frequency of the 800 nm pulse. An example of such a pattern is seen in Figure 3.33. An FFT can be preformed on the spectrum which should contain a peak corresponding to the fringe frequency, which is proportional to τ. An example FFT is shown in Figure 3.34.

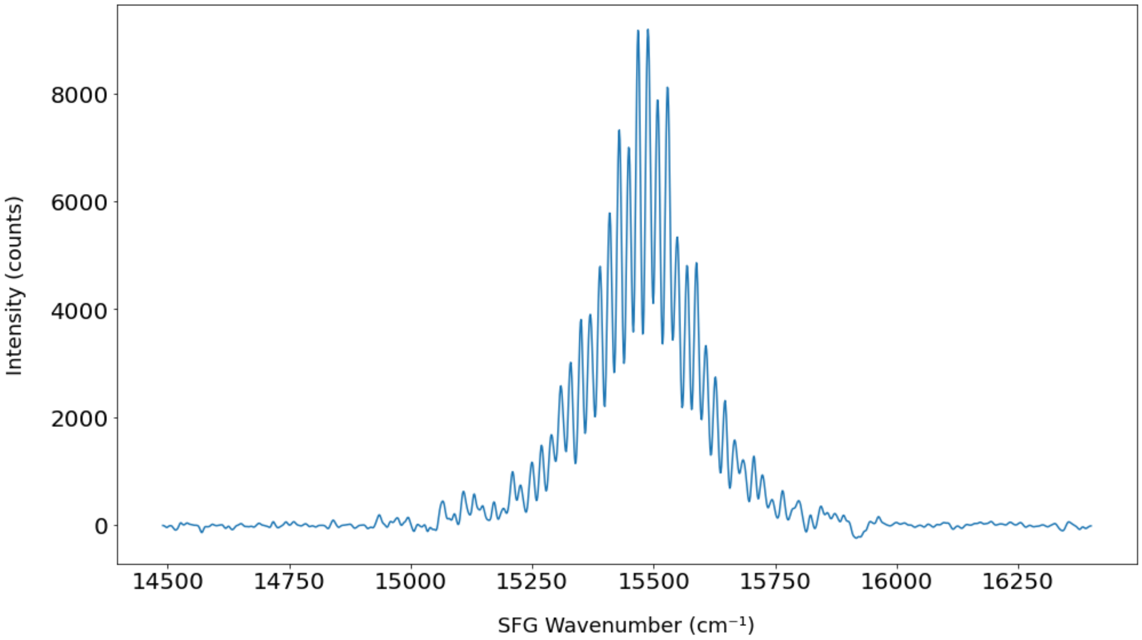

Figure 3.33. SFG fringe pattern produced from two interfering pump pulses being upconverted by a narrow-bandwidth 800 nm pulse. The sample used was a piece of gallium arsenide wafer, which is non-resonant with the frequencies of light used.

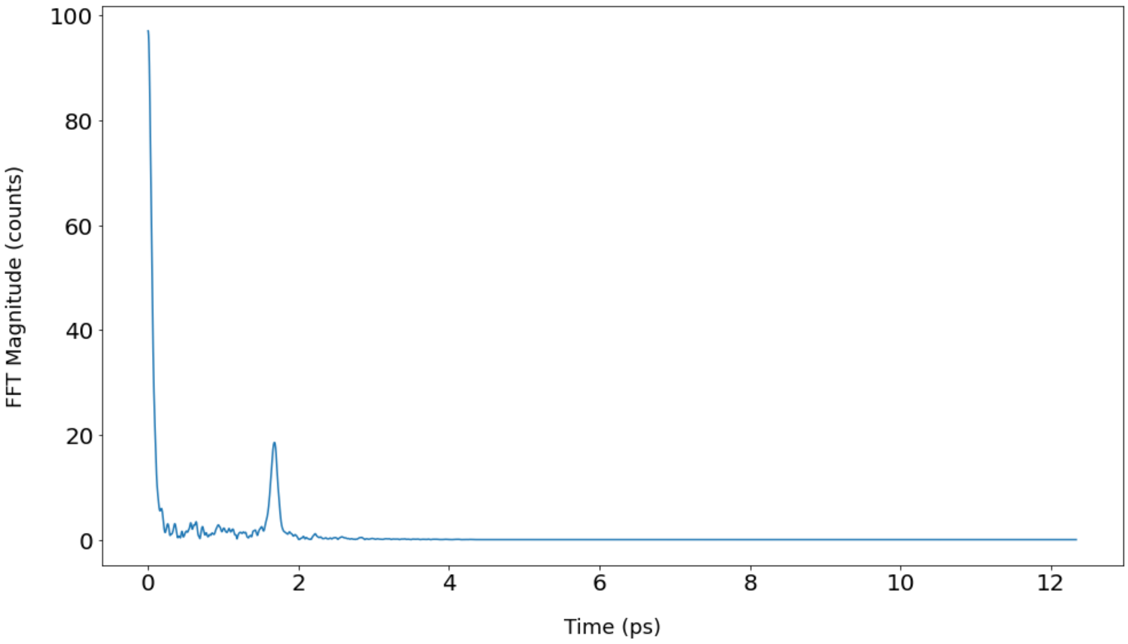

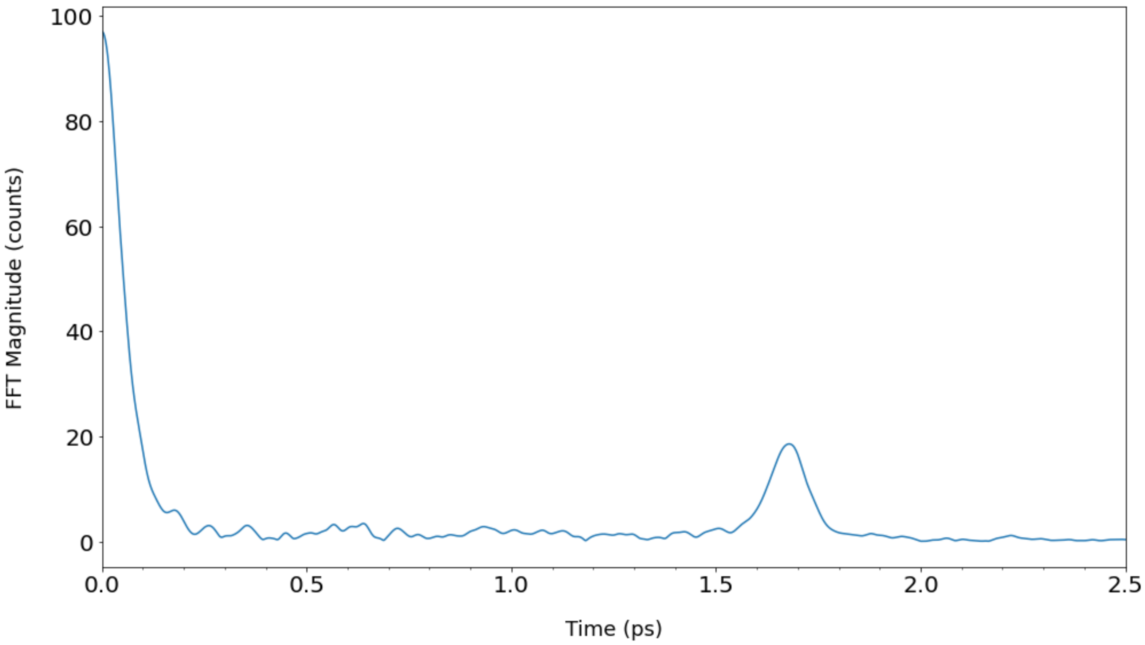

Figure 3.34. FFT magnitude for the data shown in Figure 3.33 (top) and corresponding inset plot (bottom). The peak corresponding to the time delay between infrared pump pulses is seen at approximately 1.7 ps.

The absolute value of τ is extracted from the FFT of the interference pattern seen at various interferometer mirror positions. The mirror position is reported in steps of the motion stage. By fitting this data, a set of calibration parameters are established between motor position in steps and the optical time delay between the pump pulses. While the true time difference would be linear with respect to mirror position, the time delay extracted from the FFT is actually the absolute value of the time difference. This is inconsequential to the interpretation of the data since the direction that the mirror is moving physically is known and the correct sign of the time delay can be deduced. This is verified by using some initial guesses for the calibration parameters that have the signs that are expected. Consequently, the solver used to extract calibration parameters converges on the solution that retains these signs. Alternatively, bounds could be placed on these variables. An example of a calibration plot used for a single stage is shown Figure 3.35. This calibration is preformed for both motion stages by scanning one stage while keeping the other one stationary. The calibration parameters for both stages are fit simultaneously. While this does not improve confidence in the fitted distance moved per step of each stage, it does increase confidence in the zero position of both stages. While the zero position of both stages cannot be determined in this calibration step, the parameters fit in this step are used to find the zero position for the other stage after the absolute time delay T is determined in the calibration procedure described in the next subsection.

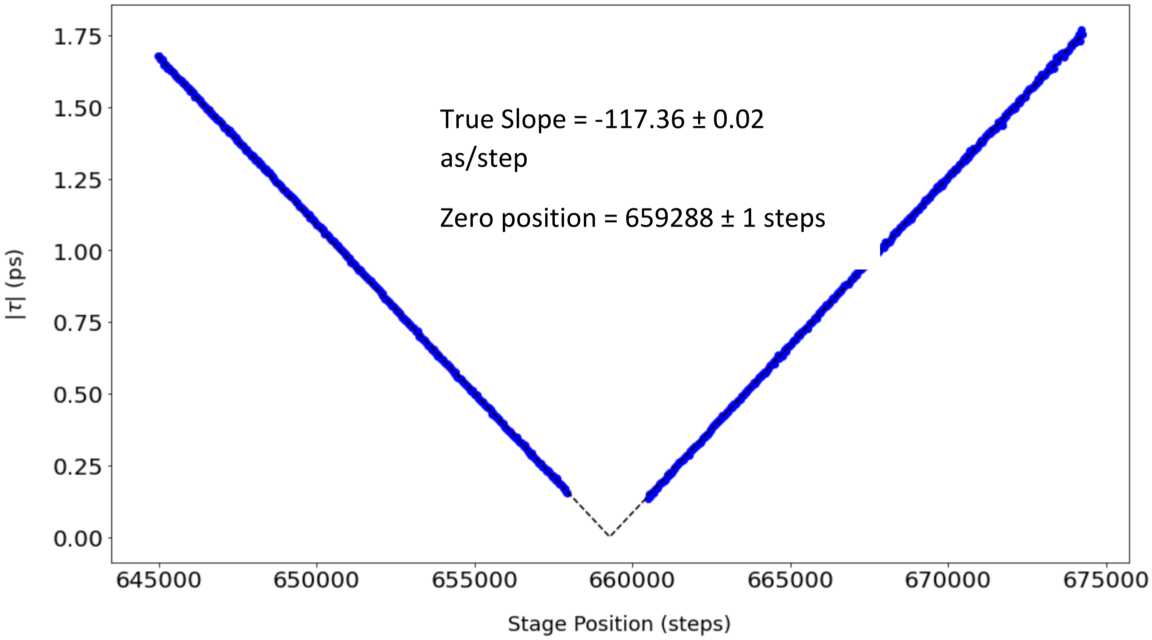

Figure 3.35. Extracted absolute value of time delays from the peaks seen in the FFTs of the fringe patterns produced at different delays between the pump pulses. Data points that correspond to small time delays were not used due to the difficulty to discern the fringe pattern from the natural spectrum of the pump pulses with no time delay between them.

The “True Slope” is the slope with its sign in agreement with the physical motion of the stage.

If the only goal of this calibration was to correctly report the pump wavenumber in the 2D spectrum, the stages’ manufacturer’s calibration could be used to find the distance moved per step so that the wavenumber error is within 0.1%. However, the true goal of the calibration is to find the positions where there is a time difference between the pump pulses of zero, which allows the stages to be moved in concert and allows for the calibration of the absolute time delay T described in the next section.

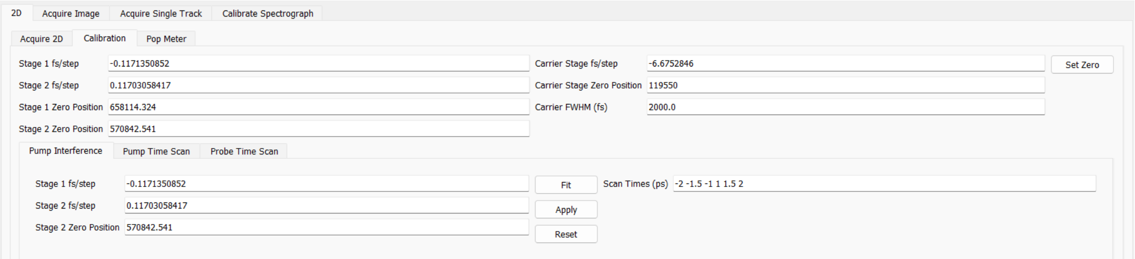

Stage 1 fs/step -0.1171350852
Stage 2 fs/step 0.11703058417
Stage 1 Zero Position 658114.324
Stage 2 Zero Position 570842.541
Carrier Stage fs/step -6.6752846
Carrier Stage Zero Position 119550
Carrier FWHM (fs) 2000.0

Stage 1 fs/step -0.1171350852
Stage 2 fs/step 0.11703058417
Stage 2 Zero Position 570842.541
Scan Times (ps) -2 -1.5 -1 1 1.5 2

Figure 3.36. GUI displaying all the parameters to be fit before collecting a 2D SFG spectrum (top), and the parameters to be fit in the pump frequency calibration (in the “Pump Interference” tab).

It should be also noted that the secondary purpose of collecting this calibration data is to provide validation of the 2D spectrometer’s ability to produce a 2D spectrum. The non-resonant gallium arsenide sample would not be expected to produce any peaks in a typical 2D spectrum due to lack of anharmonic coupling; however, when the SFG produced by the pump pulses is measured, the 2D spectrum is a direct result of the interference between the pulses, allowing the interferometer’s performance to be validated in the same configuration it is used to collect a real 2D spectrum of a sample. An example of this spectrum is shown in Figure 3.38.

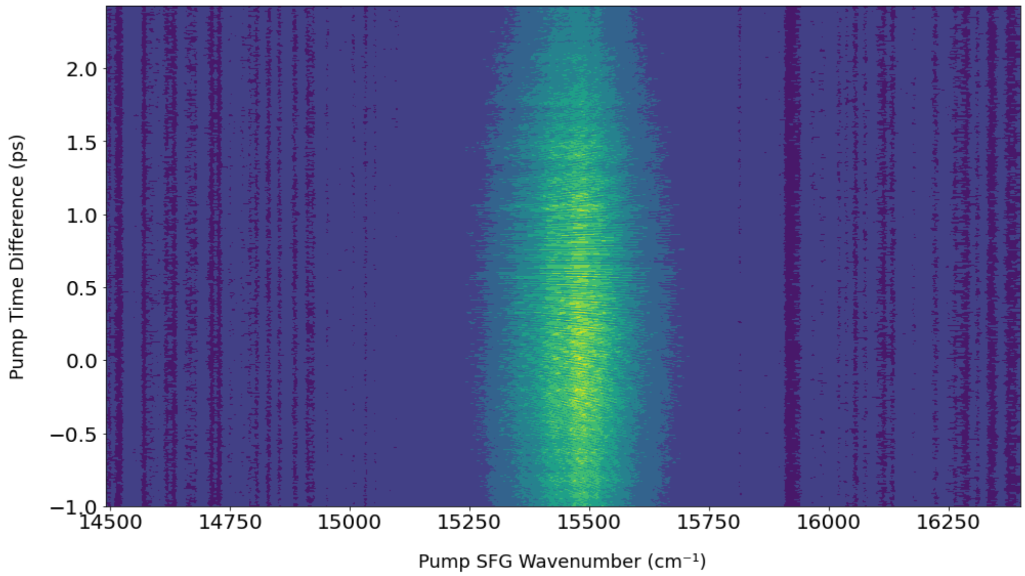

Figure 3.37. Raw data collected from calibration scan used to make Figure 3.35. The exposure time was 100 ms, while the pulse repetition rate was 1 KHz. A possible cause for artifacts is due to the CCD not being triggered from the laser and some measurements being exposed to more laser pulses than others. It is not expected to be the result of errors in positioning.

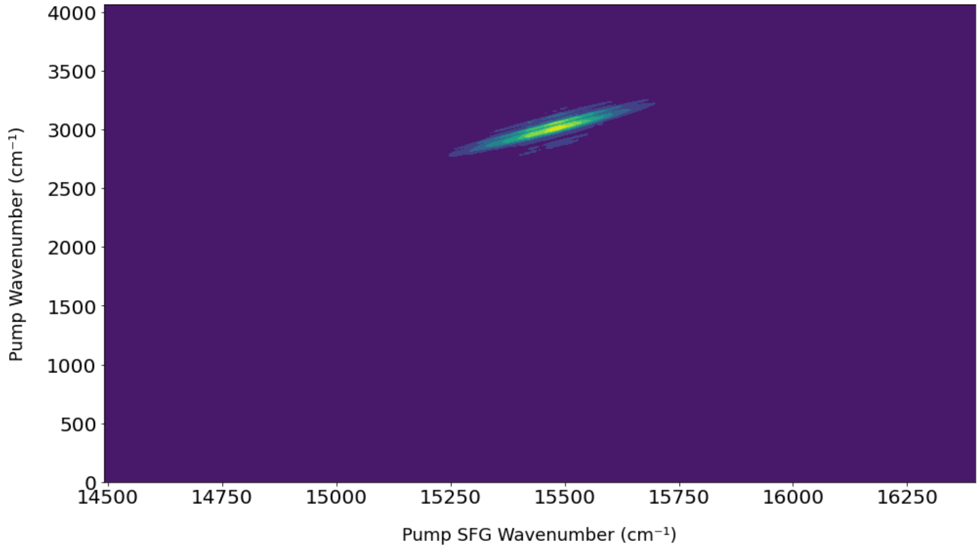

Figure 3.38. 2D pump spectrum of gallium arsenide used for validation of spectrometer's ability to produce a 2D spectrum. The spectrum is the magnitude of the FFT of the raw data shown in Figure 3.37.

3.6.3 Absolute Time Delay T

The final step in the calibration of the 2D spectrometer is the calibration of the absolute time delay T, which is the time difference between the probe IR pulse and the pump IR pulse that remains fixed in time during a scan of τ. Attempts were made to use the calibration procedure described in the previous section to calibrate T; however, the SFG from the pump and the probe could not be made to overlap on the CCD in the UV-Vis spectrometer to reliably produce an interference pattern. In place of this, a scanning procedure was used.

The scanning procedure involves scanning in time the 800 nm pulse, also referred to as the carrier pulse, over the combined pump pulses (τ=0). The scanning is done by moving a delay stage for the 800 nm pulse and measuring the total SFG intensity (all wavelengths combined) at every position. For every scan, a Gaussian peak is fit to determine its center, where the maximum SFG intensity would be expected. This scanning process is illustrated in Figure 3.39. A scan is done at different positions of the combined pump pulses to establish a calibration between the pump delay stages and the 800 nm delay stage.

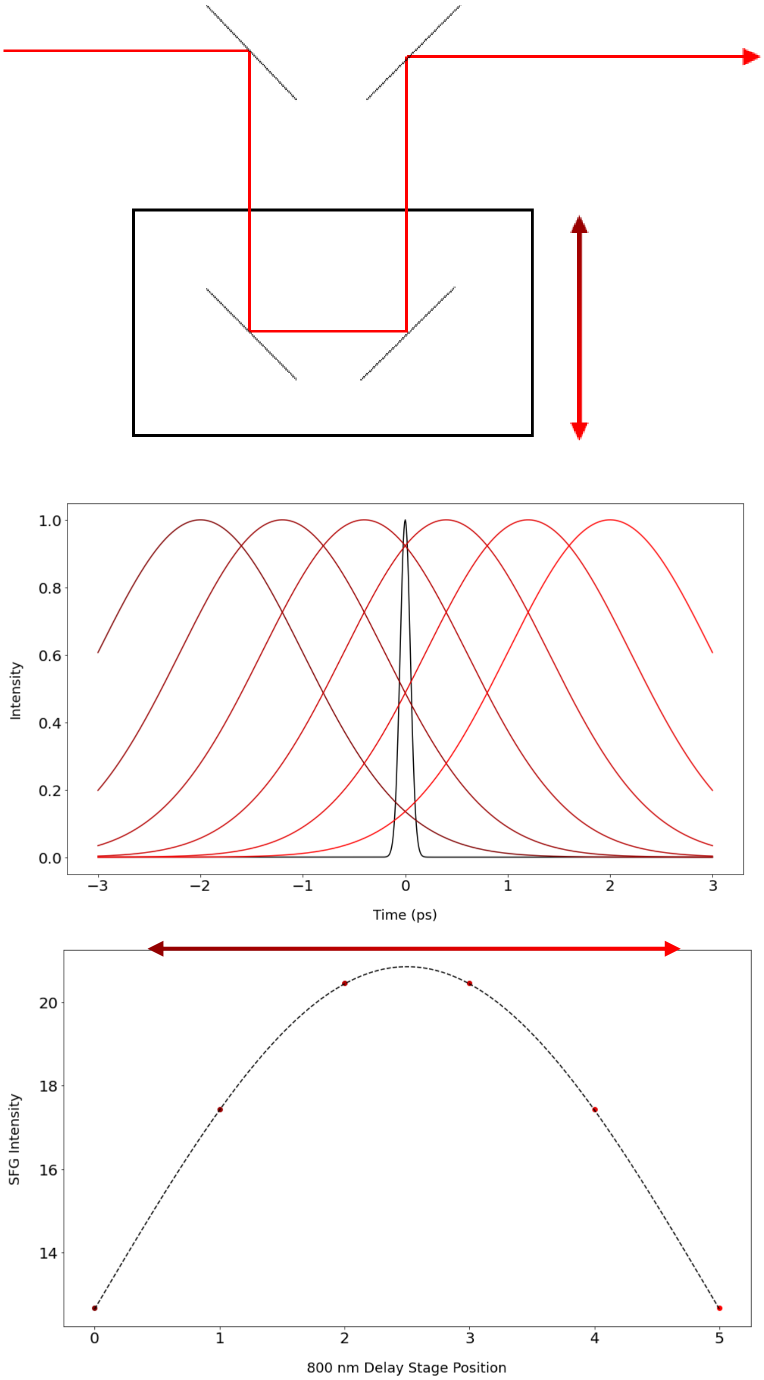

Figure 3.39. Diagram of delay stage used to scan over time delays of the 800 nm light (top). The gradient of the arrow corresponds to the gradient of the colours used in the bottom two plots. Pulse intensity of a function of time (middle). IR pulse intensity is plotted in black. 800 nm pulse intensity is plotted in varying shades of red for each time delay used in the scan. Total SFG intensity (all wavelengths combined) with colours

corresponding to the scan positions in plot above (bottom). The Gaussian peak that was fitted is shown by the black dashed line. All data is simulated for the purpose of illustration.

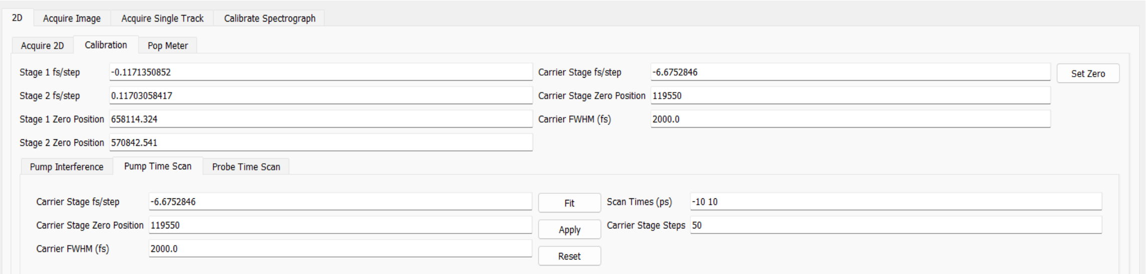

Stage 1 fs/step: -0.1171350852
Stage 2 fs/step: 0.11703058417
Stage 1 Zero Position: 658114.324
Stage 2 Zero Position: 570842.541
Carrier Stage fs/step: -6.6752846
Carrier Stage Zero Position: 119550
Carrier FWHM (fs): 2000.0

Carrier Stage fs/step: -6.6752846
Carrier Stage Zero Position: 119550
Carrier FWHM (fs): 2000.0
Scan Times (ps): -10 10
Carrier Stage Steps: 50

Figure 3.40. GUI displaying the parameters to be fit in the combined pump time scan (in the “Pump Time Scan” tab).

Once the 800 nm delay stage is calibrated against the pump delay stages, it can then be scanned over the IR probe pulse to determine the absolute time delay T. This step has the added benefit of finding the 800 nm pulse delay which maximizes the SFG intensity of the probe and hence the signal measured in the 2D spectrum.

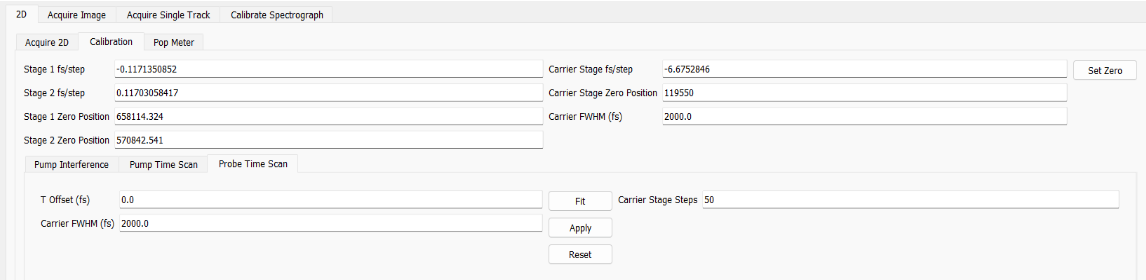

Stage 1 fs/step: -0.1171350852
Stage 2 fs/step: 0.11703058417
Stage 1 Zero Position: 658114.324
Stage 2 Zero Position: 570842.541
Carrier Stage fs/step: -6.6752846
Carrier Stage Zero Position: 119550
Carrier FWHM (fs): 2000.0

T Offset (fs): 0.0
Carrier FWHM (fs): 2000.0
Carrier Stage Steps: 50

Figure 3.41. GUI displaying the parameters to be fit in the probe time scan (in the “Probe Time Scan” tab).

3.7 Phasing

As shown in the previous section, the 2D spectrum produced from the magnitude of the FFT of the raw data is easy to interpret; however, the FFT produces a complex 2D spectrum which contains information about the phase of the oscillations corresponding to the peaks in the 2D spectrum. This phase information is lost when taking the magnitude. This section explains the experimental factors contributing to the phase observed in the complex 2D spectrum, and a method used to present the phase information in a way to more easily interpret and visualize as it pertains to the sample being studied.

For the purpose of explaining the phase of the 2D spectrum, the changes in the intensities of the SFG measured at the frequencies corresponding to the ground state and excited state of a vibrational mode, as a function of τ, caused by exciting molecules with Pump Frequency ω, can be given by;

$$\Delta \mathrm{I}_{\mathrm{ground}}(\tau) = -\mathrm{A}\cos(\omega\tau), \tag{3.2}$$

$$\Delta \mathrm{I}_{\mathrm{excited}}(\tau) = \mathrm{A}\cos(\omega\tau); \tag{3.3}$$

where A is the amplitude of the oscillations, which is determined by the maximum amount of population transfer to the excited state caused by the pump with frequency ω and the overall signal intensity produced by the probe. According to these equations, when the intensities as a function of τ are FFT'd, the 2D spectrum should be completely real with negative peaks corresponding to ground-state bleaching and positive peaks corresponding to molecules being excited by the pump, due to these oscillations having opposite phases. In practice however, τ is not necessarily known with enough certainty to make the 2D spectrum entirely real; even an error in τ that is a fraction of the period of infrared pump light would cause a significant imaginary component, which can be difficult to interpret physically. Incorporating this error into the equations above gives:

$$\Delta \mathrm{I}_{\mathrm{ground}}(\tau_c) = -\mathrm{A}\cos(\omega(\tau_c + \mathrm{t}_e)), \tag{3.4}$$

$$\Delta \mathrm{I}_{\mathrm{excited}}(\tau_c) = \mathrm{A}\cos(\omega(\tau_c + \mathrm{t}_e)), \tag{3.5}$$

Where τ_c is the τ determined by calibration and t_e is the error in calibration.

In case of data not being sampled over the maximum range where there are oscillations in intensity, the data is apodized before being FFT'd to avoid the spectral artifacts caused by having oscillations with different phases at the beginning and end of the data. This process adds a different amount of distortion to the phase at different frequencies, causing parts of the 2D spectrum to become imaginary. Incorporating this effect into the equations above gives:

$$\Delta \mathrm{I}_{\text{ground}}(\tau_c) = -\mathrm{A}\cos(\omega(\tau_c + \mathrm{t}_e) + \mathrm{q}_\omega), \tag{3.6}$$

$$\Delta \mathrm{I}_{\text{excited}}(\tau_c) = \mathrm{A}\cos(\omega(\tau_c + \mathrm{t}_e) + \mathrm{q}_\omega), \tag{3.7}$$

where $q_\omega$is the phase offset for pump frequency ω caused by apodizing the data. Figure 3.42 and Figure 3.43 were made to illustrate the effect of apodization on the phase reported by the FFT.

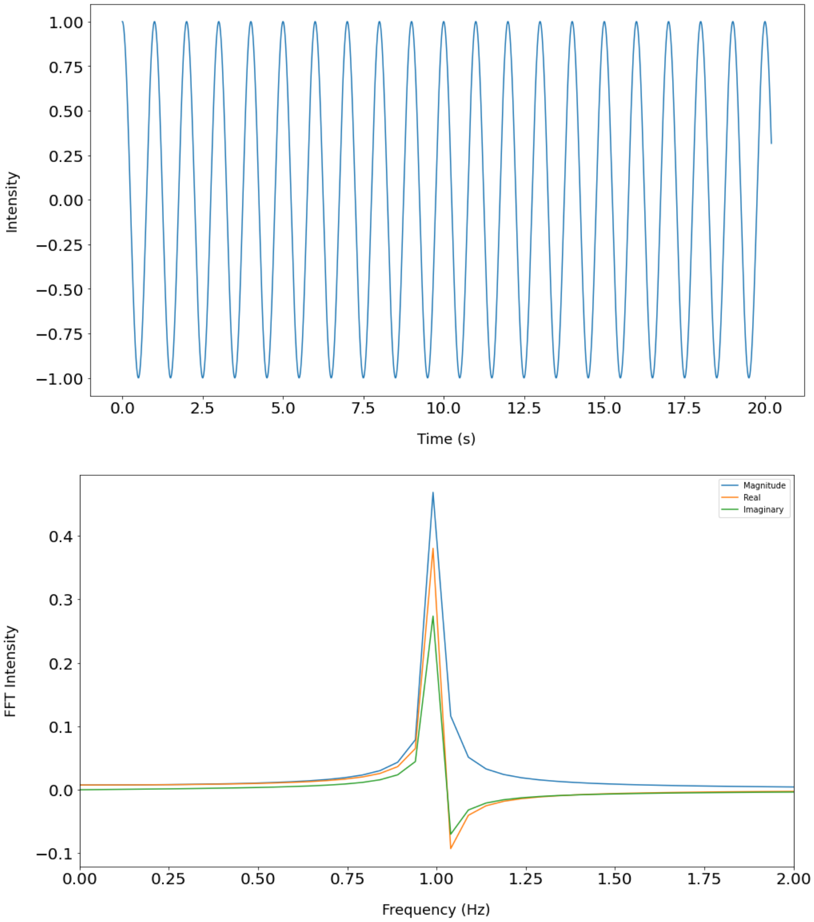

Figure 3.42. Non-apodized data used for illustration (top) and corresponding FFT (bottom). The data starts with a phase of zero but does not end with a phase of zero, resulting in a non-zero phase in the FFT intensity. Consequently, the result of the FFT is not entirely real or positive.

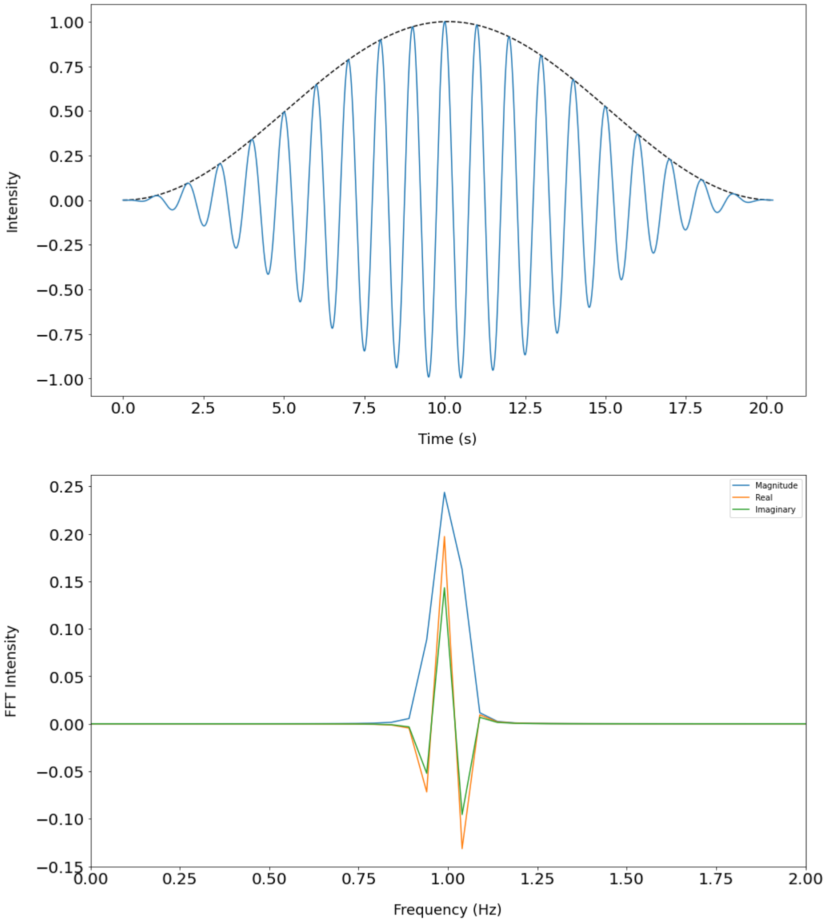

Figure 3.43. Data from Figure 3.42 after being apodized plotted in blue with the Hanning window used for apodization plotted in black (top), and corresponding FFT (bottom). The phases seen in the FFT have been shifted from those seen in Figure 3.43 by different amounts for each frequency.

As shown in the equations above, even after the effects of error in τ and apodization are accounted for, the oscillations retain opposite phases with respect to each other. It is desirable to produce a spectrum which retains the relative phases of the oscillations for a given pump frequency, while not being influenced by effects that are not specific to the sample being analyzed.

A phasing procedure, discussed below, was developed to make the 2D spectrum entirely real with a sign that is consistent with the ground-state bleaching peaks being negative, while retaining the relative phases of the oscillations for a given pump frequency. The result of this procedure performed on simulated data is shown in Figure 3.44.

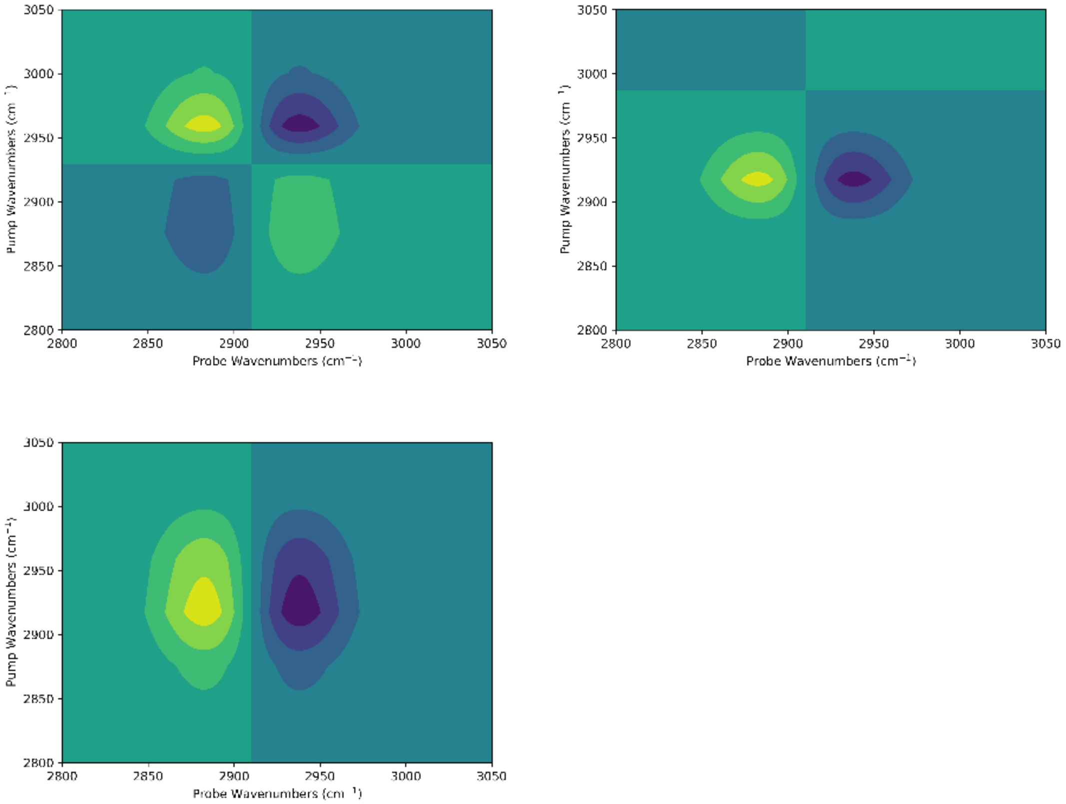

Figure 3.44. Real component of unphased FFT (top-left). Imaginary component of unphased FFT (top-right). Real component of phased FFT (bottom). All data is the result of simulation used to illustrate the effect of the phasing procedure. The imaginary component of the phased FFT is not shown because it is insignificant and likely the result of rounding error. The simulation was done using a typical CH3 stretching frequency and typical anharmonic shift. The two peaks are Gaussian with equal magnitude and opposite sign. A random error in time was added to the simulated data in the time domain, which was then FFT'd to produce the plots of the unphased signal.

The phasing procedure is preformed on each pump frequency independently. Doing so means that only a phase offset has to be found for each pump frequency, without determining a time offset valid for all pump frequencies. The procedure is performed on the complex 2D spectrum after the data is FFT'd. Since the 2D spectrum contains complex values, the phase for a pump frequency can be changed by multiplying it by a complex-exponential phase-correction factor. Since each pump frequency has a single phase offset for all SFG frequencies, only a single phase-correction factor needs to be applied to all

SFG frequencies for a given pump frequency. In doing so, the phase of the ground-state peak relative to the phase of the excited-state peak is preserved.

The first step of the phasing procedure is to make the 2D spectrum entirely real. This is done by changing the phase of the data at a pump frequency with a phase-correction factor, so that the sum of the magnitudes of the imaginary parts across all SFG frequencies is minimized. Since this step does not depend on the sign of the spectrum, only an interval of 0 to π has to be searched for the correct phase-correction factor.

The second step of the phasing procedure involves making the ground-state bleaching peaks negative. This is done by taking the sum of the spectrum at a pump frequency multiplied by the ground-state spectrum (obtained with pump blocked), and negating the data (shifting the phase by π) if the sum is not negative. While this constraint could be incorporated into the minimization step, it is far more computationally efficient to select the correct sign after the minimization has been completed, as the constraint only needs to be checked once.

The phasing procedure described allows for more flexibility in interpreting experimental data, without relying on the accuracy of the calibration of the spectrometer or the data not being apodized. The information lost in this procedure is not expected to be relevant to the sample.

3.8 Data Acquisition Program

A data acquisition program, described in this section, was developed to allow users of the 2D spectrometer to acquire a spectrum with minimal technical knowledge. The program features a full GUI. It is able to scan over both τ and T while capturing spectra on the UV-Vis spectrometer. The calibration procedures described in the previous Section 3.6 are also integrated into the program. The GUI was developed solely by the author of this thesis.

A full 2D SFG spectrum can take as long as a day to acquire, so it is important to identify problems with the experiment early on. The program includes real-time data analysis to allow the user to view the 2D spectrum as it is acquired, with a variable resolution in pump wavenumber depending on the values of τ sampled.

The program also allows the three-dimensional data, produced from scanning both τ and T, to be viewed in slices of any dimension, showing information about the lifetime of excitations in the dimension of T, and the energies of the excitations in the dimensions of pump and probe wavenumber. The GUI is shown in Figure 3.45.

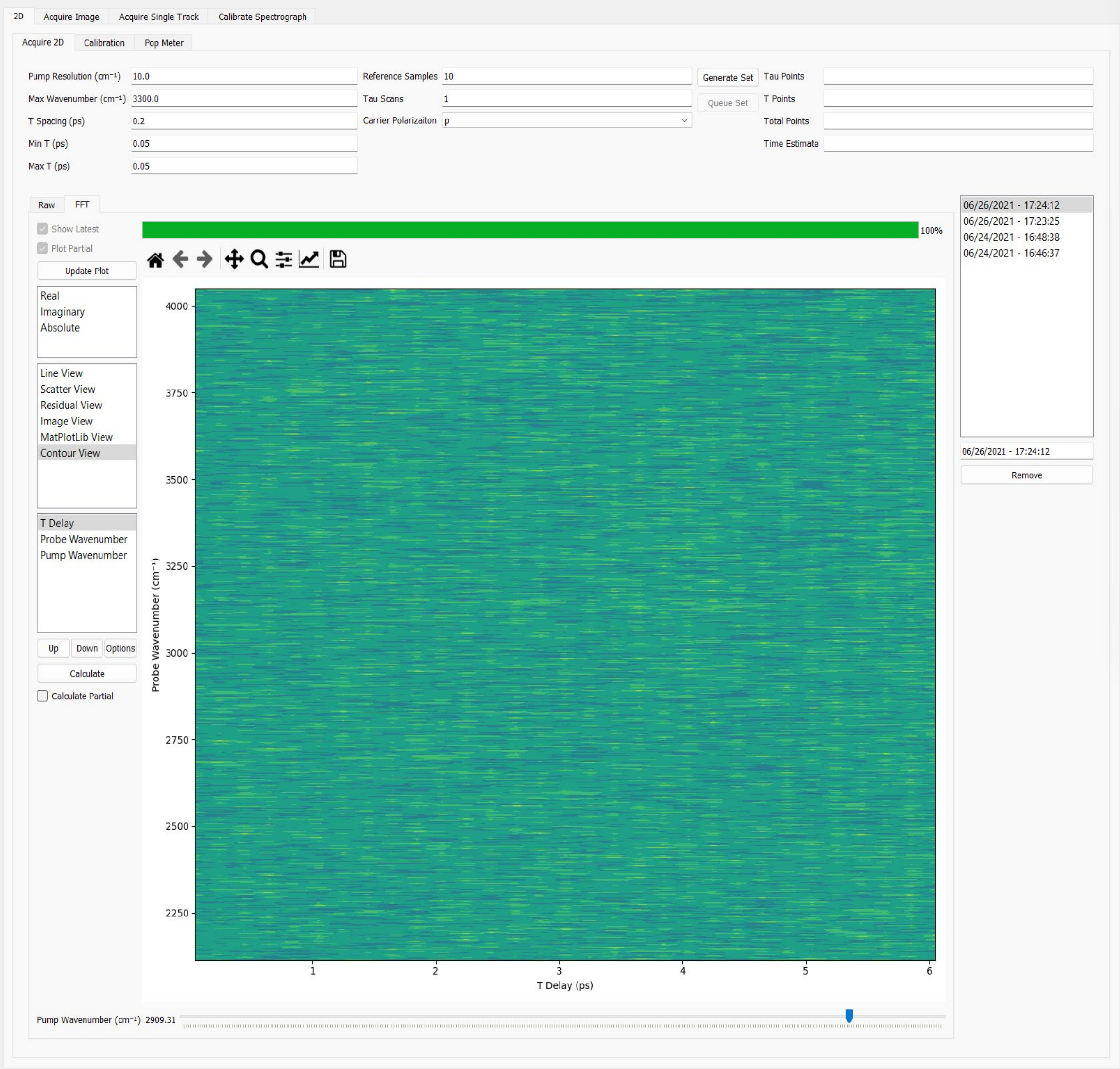

Pump Resolution (cm^{-1}) 10.0

Max Wavenumber (cm^{-1}) 3300.0

T Spacing (ps) 0.2

Min T (ps) 0.05

Max T (ps) 0.05

Reference Samples 10

Tau Scans 1

Carrier Polarizaiton p

Tau Points

T Points

Total Points

Time Estimate

06/26/2021 - 17:24:12

Pump Wavenumber (cm^{-1}) 2909.31

Figure 3.45. GUI showing 2D data view of probe wavenumber over the y-axis and Time Delay T over the x-axis, at a fixed pump wavenumber. The data shown is the result of noise on the CCD, as no data was successfully acquired with the 2D spectrometer to produce a 2D spectrum of a sample.

3.9 DFT Predictions

The design of the spectrometer has been heavily influenced by simulations of the expected signal. Density functional theory (DFT) is able to predict the derivatives of the potential energy with respect to each normal vibrational mode. It is also able to calculate higher order derivatives of every mode with respect to every other. This allows for the calculation of the anharmonic coupling matrix which includes the conventional anharmonicity of the modes along the diagonal, as well as the anharmonic shift that each mode imparts on another in the off-diagonal elements. The ability to produce a peak pair depends on the magnitude of the underlying anharmonicity and the ability to resolve the two peaks; therefore, the calculation of the anharmonic matrix is crucial in predicting which peaks, if any, will be seen in a spectrum of a given sample with a given spectrometer probe wavenumber resolution.

A film of stearic acid was intended to be used as a sample to demonstrate the working of the 2D spectrometer. To ensure that it was a suitable choice, DFT was used in attempt to predict the anharmonic matrix in Gaussian 09. The calculation was unable to complete due to the 162 normal vibrational modes in stearic acid. In place of stearic acid, the DFT calculations were performed on octanoic acid, since it is expected to exhibit a similar amount of anharmonicity in its CH stretches while having only 72 normal vibrational modes, allowing the calculation of the anharmonic matrix to complete. The modes expected to produce significant SFG intensity are shown in Figure 3.46 and Figure 3.47. The anharmonic matrix for these modes only is shown in Table 3.1.

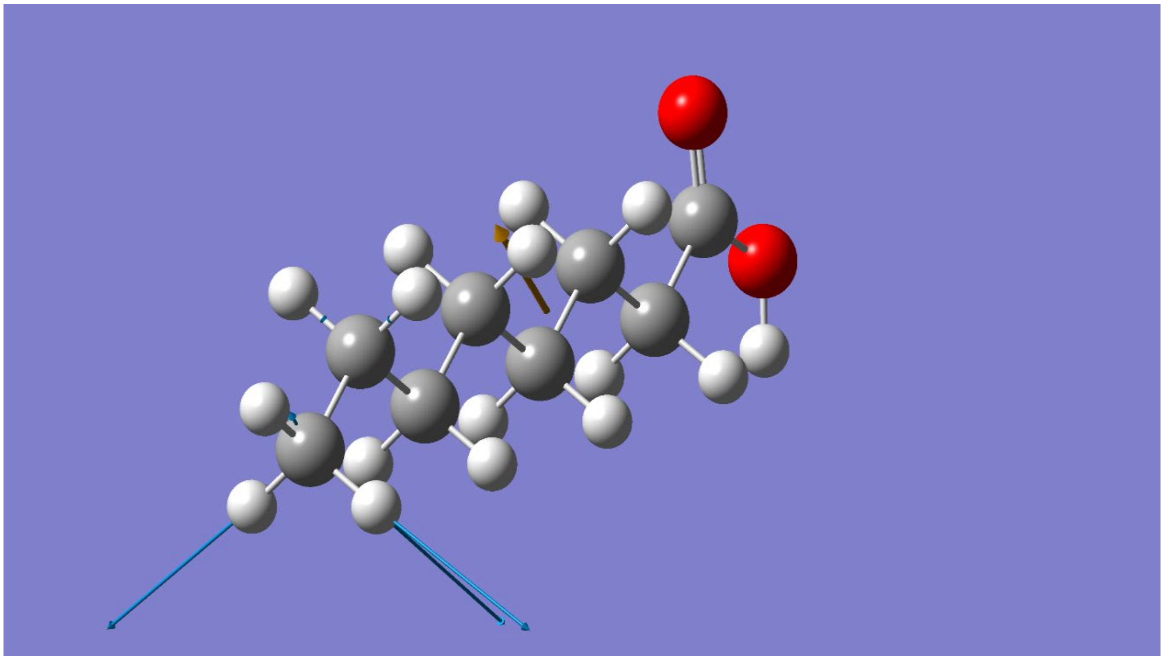

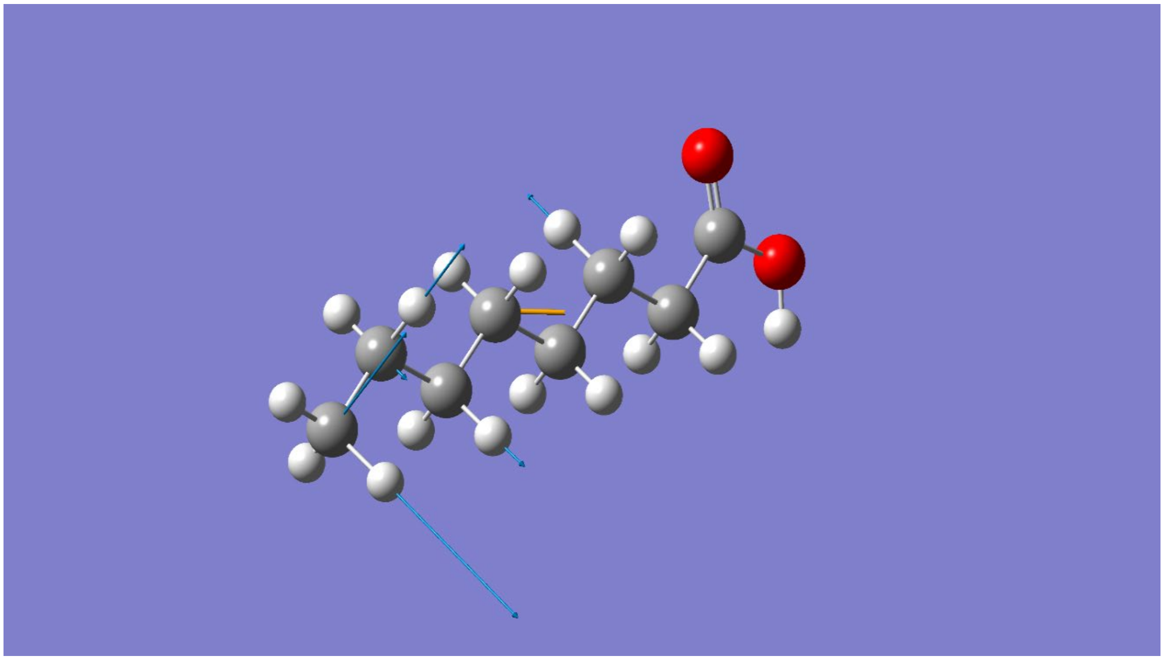

Figure 3.46. Asymmetric CH3 stretches ν_1 (top) and ν_2 (bottom) in octanoic acid which are expected to have significant signal intensity in the SFG spectrum. Under the harmonic approximation, the modes are degenerate with a frequency of 3111 cm^{-1}.

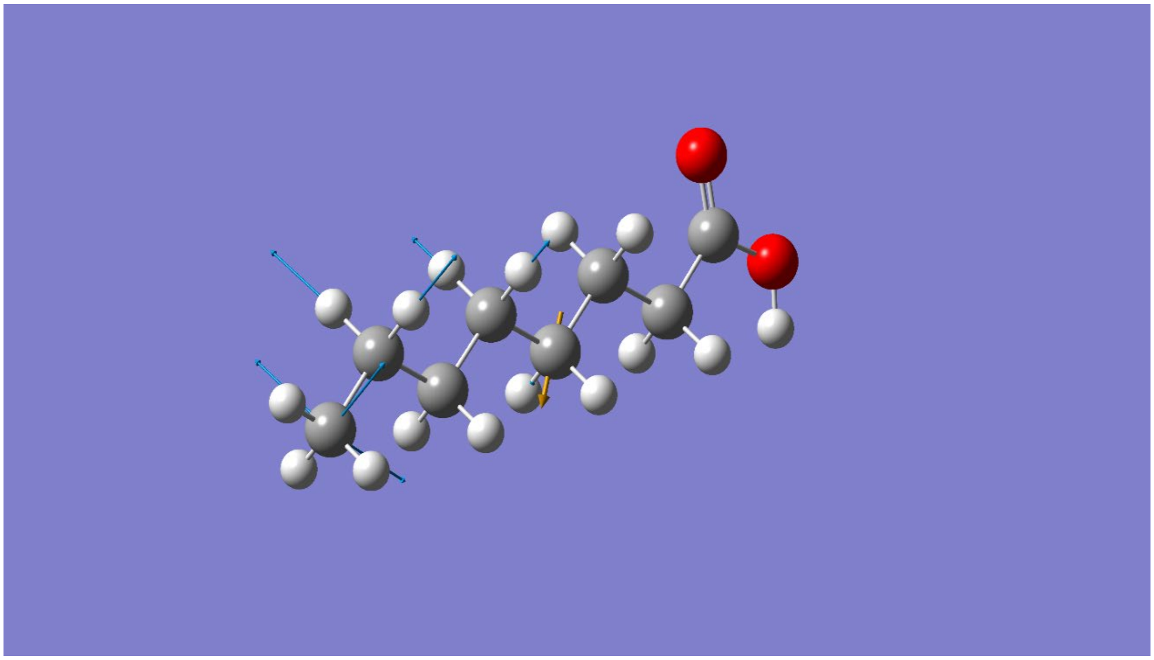

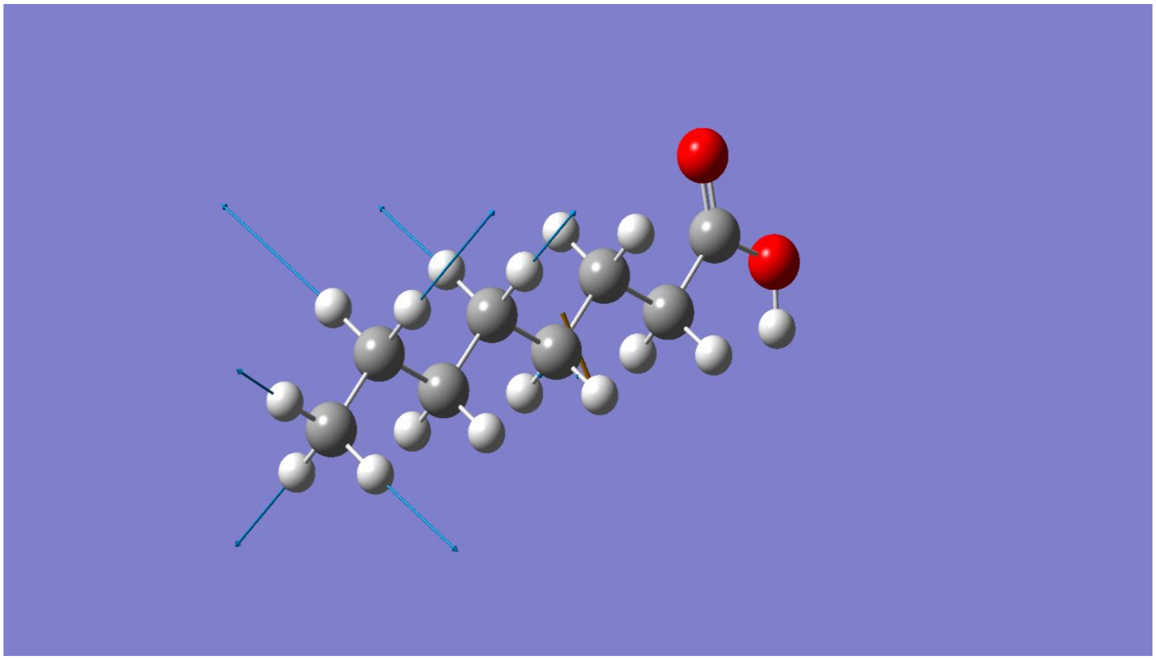

Figure 3.47. Symmetric CH3 stretches ν_3 (top) and ν_4 (bottom) in octanoic acid which are expected to have significant signal intensity in the SFG spectrum. Under the harmonic approximation, the frequencies of the modes are 3043 and 3045 cm^{-1} respectively.

Table 3.1. Anharmonic coupling matrix of select modes in Figure 3.46 and Figure 3.47 all values are in units of cm⁻¹. The matrix is symmetric about the diagonal, so the lower values were omitted. Taking anharmonicity into account, the fundamental frequencies of the modes are 2981, 2953, 2812 and 2922 cm⁻¹ respectively.

$$\begin{array}{cc} & \begin{array}{cccc} \nu_1 & \nu_2 & \nu_3 & \nu_4 \end{array} \\ \begin{array}{c} \nu_1 \\ \nu_2 \\ \nu_3 \\ \nu_4 \end{array} & \begin{bmatrix} -20 & -25 & -48 & -33 \\ & -38 & -60 & -15 \\ & & -11 & -26 \\ & & & -9 \end{bmatrix} \end{array}$$

The results of the DFT calculation show that a significant amount of anharmonic coupling is seen between the modes expected to produce significant SFG intensity. This means that the probe wavenumber resolution of the 2D spectrometer can be sacrificed for greater signal intensity, while still being able to observe peaks in the 2D spectrum.

4 Ongoing and Future Directions

4.1 Phase-sensitive SFG (PS-SFG)

The results of the PS-SFG measurements on gallium arsenide presented in Chapter 2 inspire confidence that the same measurement methodology can be used on vibrationally resonant samples. The ability to acquire PS-SFG measurements at SFU adds to future students' arsenal. If future students identify a study that requires the information provided from PS-SFG measurements, not only would the methodology presented here be of great value to them, but their study would of great value in demonstrating the usefulness of the methodology.

Another interesting prospect of the PS-SFG measurement methodology presented here, is to compare it to a spectral-interferometric implementation within the same SFG spectrometer. Such a comparison would provide a better understanding of how the theoretical advantages and disadvantages of each approach translate to experimental results.

4.2 Two-dimensional SFG (2D SFG)

The ability to acquire a true pump-probe 2D spectrum must be demonstrated before using the spectrometer to probe chemical systems of research interest. The current bottleneck in doing so is the ability to generate mid-IR light to transfer enough population into an excited state. The bandwidth and intensity of light that can be generated will dictate the systems that can be studied.

An interesting system to probe with the 2D SFG-VS spectrometer is the Langmuir-Blodgett film of cadmium stearate, which is known to produce a resonant SFG signal with sharp peaks.[8] In order to distinguish the effects of inter- and intra-molecular coupling at the interface, one would require a population of molecules to have different vibrational frequencies. A possibility would be to make a film where half of the molecules are deuterated. The coupling observed in the 2D-SFG spectrum between the deuterated and non-deuterated vibrational frequencies could only be the result of intermolecular coupling.

Another possible application of 2D SFG-VS would be the study of reaction dynamics. Due to the use of ultrashort pulses, 2D SFG-VS provides a narrow window to look at photocatalysis reactions at an interface where it can probe short-lived intermediates and measure their lifetimes after photocatalysis.

The literature on 2D SFG remains relatively limited compared to most fields, and is primarily focused on demonstrating the ability to probe different systems. More work is required both in data acquisition and the interpretation of the data before the technique is widely adopted. The work presented in this thesis is going to contribute to the implementation of 2D SFG-VS at SFU; which will broaden applications, build up skills and increase the community of users.

References

(1) Boyd, R. W. *Nonlinear Optics*; Academic Press, 2020.

(2) Murti, Y. V. G. S.; Vijayan, C. *Physics of Nonlinear Optics*; Springer Nature, 2021.

(3) New, G. *Introduction to Nonlinear Optics*; Cambridge University Press, 2014.

(4) Schultz, M. J.; Baldelli, S.; Schnitzer, C.; Simonelli, D. Aqueous Solution/Air Interfaces Probed with Sum Frequency Generation Spectroscopy. *J. Phys. Chem. B* **2002**, *106* (21), 5313–5324. https://doi.org/10.1021/jp014466v.

(5) Shen, Y. R. Surface Properties Probed by Second-Harmonic and Sum-Frequency Generation. *Nature* **1989**, *337* (6207), 519–525. https://doi.org/10.1038/337519a0.

(6) Zhu, X. D.; Suhr, H.; Shen, Y. R. Surface Vibrational Spectroscopy by Infrared-Visible Sum Frequency Generation. *Phys. Rev. B* **1987**, *35* (6), 3047–3050. https://doi.org/10.1103/PhysRevB.35.3047.

(7) Johansson, T. P.; Leach, G. W. Sum Frequency Generation Study of Langmuir Blodgett Film Architecture. *J. Phys. Chem. B* **2006**, *110* (33), 16567–16574. https://doi.org/10.1021/jp060804m.

(8) Johansson, T. P.; Leach, G. W. A Low Temperature Phase Transition in Langmuir-Blodgett Films. *J. Phys. Chem. B* **2008**, *112* (44), 13823–13833. https://doi.org/10.1021/jp806226e.

(9) Backus, E. H. G.; Cyran, J. D.; Grechko, M.; Nagata, Y.; Bonn, M. Time-Resolved Sum Frequency Generation Spectroscopy: A Quantitative Comparison Between Intensity and Phase-Resolved Spectroscopy. *J. Phys. Chem. A* **2018**, *122* (9), 2401–2410. https://doi.org/10.1021/acs.jpca.7b12303.

(10) Smit, W. J.; Tang, F.; Nagata, Y.; Sánchez, M. A.; Hasegawa, T.; Backus, E. H. G.; Bonn, M.; Bakker, H. J. Observation and Identification of a New OH Stretch Vibrational Band at the Surface of Ice. *J. Phys. Chem. Lett.* **2017**, *8* (15), 3656–3660. https://doi.org/10.1021/acs.jpclett.7b01295.

(11) Kraack, J. P.; Hamm, P. Surface-Sensitive and Surface-Specific Ultrafast Two-Dimensional Vibrational Spectroscopy. *Chem. Rev.* **2017**, *117* (16), 10623–10664. https://doi.org/10.1021/acs.chemrev.6b00437.

(12) Ho, J.-J.; Skoff, D. R.; Ghosh, A.; Zanni, M. T. Structural Characterization of Single-Stranded DNA Monolayers Using Two-Dimensional Sum Frequency Generation Spectroscopy. *J. Phys. Chem. B* **2015**, *119* (33), 10586–10596. https://doi.org/10.1021/acs.jpcb.5b07078.

(13) Vanselous, H.; Stingel, A. M.; Petersen, P. B. Interferometric 2D Sum Frequency Generation Spectroscopy Reveals Structural Heterogeneity of Catalytic Monolayers on Transparent Materials. *J. Phys. Chem. Lett.* **2017**, *8* (4), 825–830. https://doi.org/10.1021/acs.jpclett.6b03025.

(14) Hsieh, C.-S.; Okuno, M.; Hunger, J.; Backus, E. H. G.; Nagata, Y.; Bonn, M. Aqueous Heterogeneity at the Air/Water Interface Revealed by 2D-HD-SFG Spectroscopy. *Angewandte Chemie International Edition* **2014**, *53* (31), 8146–8149. https://doi.org/10.1002/anie.201402566.

(15) Singh, P. C. 2D Heterodyne-Detected Sum Frequency Generation Study on the Ultrafast Vibrational Dynamics of H_2O and HOD Water at Charged Interfaces. *The Journal of Chemical Physics* **2015**, *142* (21), 212431. https://doi.org/10.1063/1.4918644.

(16) Ho, J.-J.; Ghosh, A.; Zhang, T. O.; Zanni, M. T. Heterogeneous Amyloid β-Sheet Polymorphs Identified on Hydrogen Bond Promoting Surfaces Using 2D SFG Spectroscopy. *J. Phys. Chem. A* **2018**, *122* (5), 1270–1282. https://doi.org/10.1021/acs.jpca.7b11934.

(17) Xiong, W.; Laaser, J. E.; Mehlenbacher, R. D.; Zanni, M. T. Adding a Dimension to the Infrared Spectra of Interfaces Using Heterodyne Detected 2D Sum-Frequency Generation (HD 2D SFG) Spectroscopy. *Proceedings of the National Academy of Sciences* **2011**, *108* (52), 20902–20907. https://doi.org/10.1073/pnas.1115055108.

(18) Laaser, J. E.; Zanni, M. T. Extracting Structural Information from the Polarization Dependence of One- and Two-Dimensional Sum Frequency Generation Spectra. *J. Phys. Chem. A* **2013**, *117* (29), 5875–5890. https://doi.org/10.1021/jp307721y.

(19) Laaser, J. E.; Skoff, D. R.; Ho, J.-J.; Joo, Y.; Serrano, A. L.; Steinkruger, J. D.; Gopalan, P.; Gellman, S. H.; Zanni, M. T. Two-Dimensional Sum-Frequency Generation Reveals Structure and Dynamics of a Surface-Bound Peptide. *J. Am. Chem. Soc.* **2014**, *136* (3), 956–962. https://doi.org/10.1021/ja408682s.

(20) Barone, V. Anharmonic Vibrational Properties by a Fully Automated Second-Order Perturbative Approach. *J. Chem. Phys.* **2005**, *122* (1), 014108. https://doi.org/10.1063/1.1824881.

(21) Bloino, J.; Biczysko, M.; Barone, V. Anharmonic Effects on Vibrational Spectra Intensities: Infrared, Raman, Vibrational Circular Dichroism, and Raman Optical Activity. *J. Phys. Chem. A* **2015**, *119* (49), 11862–11874. https://doi.org/10.1021/acs.jpca.5b10067.

(22) Covert, P. A.; FitzGerald, W. R.; Hore, D. K. Simultaneous Measurement of Magnitude and Phase in Interferometric Sum-Frequency Vibrational Spectroscopy. *J. Chem. Phys.* **2012**, *137* (1), 014201. https://doi.org/10.1063/1.4731282.

(23) Li, H. H. Refractive Index of Alkaline Earth Halides and Its Wavelength and Temperature Derivatives. *Journal of Physical and Chemical Reference Data* **1980**, *9* (1), 161–290. https://doi.org/10.1063/1.555616.

(24) *EAGLE | PCB Design And Electrical Schematic Software | Autodesk*. https://www.autodesk.ca/en/products/eagle/overview (accessed 2022-10-27).

(25) *PCB Manufacturing & Assembly Capabilities - JLCPCB*. https://jlcpcb.com/capabilities/pcb-capabilities (accessed 2022-10-27).

(26) Zhang Qiu-Lin et al. Generation of Broadly Tunable Picosecond Mid-Infrared Laser and Sensitive Detection of a Mid-Infrared Signal by Parametric Frequency up-Conversion in MgO:LiNbO3 Optical Parametric Amplifiers. *Chinese Phys. B* **2012**, *21* (5), 054213. https://doi.org/10.1088/1674-1056/21/5/054213.

(27) Yang, H.; Qian, L.; Yuan, P.; Luo, H.; Zhu, H. Generation of Broadly Tunable Mid-Infrared Femtosecond Pulses by a LiNbO3 Optical Parametric Amplifier. *Chin. Sci. Bull.* **2009**, *54* (20), 3623–3626. https://doi.org/10.1007/s11434-009-0189-0.

(28) Smith, A. V. *Crystal Nonlinear Optics: With SNLO Examples*; AS-Photonics Albuquerque, NM, USA, 2018.

(29) Su, Z.; Meng, Q.; Zhang, B. Analysis on the Damage Threshold of MgO:LiNbO3 Crystals under Multiple Femtosecond Laser Pulses. *Optical Materials* **2016**, *60*, 443–449. https://doi.org/10.1016/j.optmat.2016.08.036.

(30) Augulis, R.; Zigmantas, D. Two-Dimensional Electronic Spectroscopy with Double Modulation Lock-in Detection: Enhancement of Sensitivity and Noise Resistance. *Opt. Express, OE* **2011**, *19* (14), 13126–13133. https://doi.org/10.1364/OE.19.013126.

(31) *Fusion 360 | 3D CAD, CAM, CAE, & PCB Cloud-Based Software | Autodesk*. https://www.autodesk.ca/en/products/fusion-360/overview (accessed 2022-10-27).

(32) *STM32CubeMX - STM32Cube initialization code generator - STMicroelectronics*. https://www.st.com/en/development-tools/stm32cubemx.html (accessed 2022-10-27).

(33) *MDK Version 5*. https://www2.keil.com/mdk5 (accessed 2022-10-27).

(34) Stiopkin, I. V.; Jayathilake, H. D.; Bordenyuk, A. N.; Benderskii, A. V. Heterodyne-Detected Vibrational Sum Frequency Generation Spectroscopy. *J. Am. Chem. Soc.* **2008**, *130* (7), 2271–2275. https://doi.org/10.1021/ja076708w.

(35) Vanselous, H.; Petersen, P. B. Extending the Capabilities of Heterodyne-Detected Sum-Frequency Generation Spectroscopy: Probing Any Interface in Any Polarization Combination. *J. Phys. Chem. C* **2016**, *120* (15), 8175–8184. https://doi.org/10.1021/acs.jpcc.6b01252.

(36) Xu, B.; Wu, Y.; Sun, D.; Dai, H.-L.; Rao, Y. Stabilized Phase Detection of Heterodyne Sum Frequency Generation for Interfacial Studies. *Opt. Lett., OL* **2015**, *40* (19), 4472–4475. https://doi.org/10.1364/OL.40.004472.

(37) Harris, C. R.; Millman, K. J.; van der Walt, S. J.; Gommers, R.; Virtanen, P.; Cournapeau, D.; Wieser, E.; Taylor, J.; Berg, S.; Smith, N. J.; Kern, R.; Picus, M.; Hoyer, S.; van Kerkwijk, M. H.; Brett, M.; Haldane, A.; del Río, J. F.; Wiebe, M.; Peterson, P.; Gérard-Marchant, P.; Sheppard, K.; Reddy, T.; Weckesser, W.; Abbasi, H.; Gohlke, C.; Oliphant, T. E. Array Programming with NumPy. *Nature* **2020**, *585* (7825), 357–362. https://doi.org/10.1038/s41586-020-2649-2.

(38) *numpy.fft.rfft — NumPy v1.23 Manual*. https://numpy.org/doc/stable/reference/generated/numpy.fft.rfft.html (accessed 2022-10-31).

(39) *numpy.fft.rfftfreq — NumPy v1.23 Manual*. https://numpy.org/doc/stable/reference/generated/numpy.fft.rfftfreq.html (accessed 2022-11-01).

(40) *numpy.correlate — NumPy v1.23 Manual*. https://numpy.org/doc/stable/reference/generated/numpy.correlate.html (accessed 2022-10-31).

(41) Raschke, M. B.; Hayashi, M.; Lin, S. H.; Shen, Y. R. Doubly-Resonant Sum-Frequency Generation Spectroscopy for Surface Studies. *Chemical Physics Letters* **2002**, *359* (5), 367–372. https://doi.org/10.1016/S0009-2614(02)00560-2.

Appendix A: Spectral-interferometric PS-SFG

Spectral-interferometric PS-SFG involves imparting a systematic phase shift across frequencies within the same measurement, which is usally acomplished by adding an additional optical path length between the SFG of the sample and LO. A diagram of a typical spectral-interferometric PS-SFG setup is shown in Figure A.1.

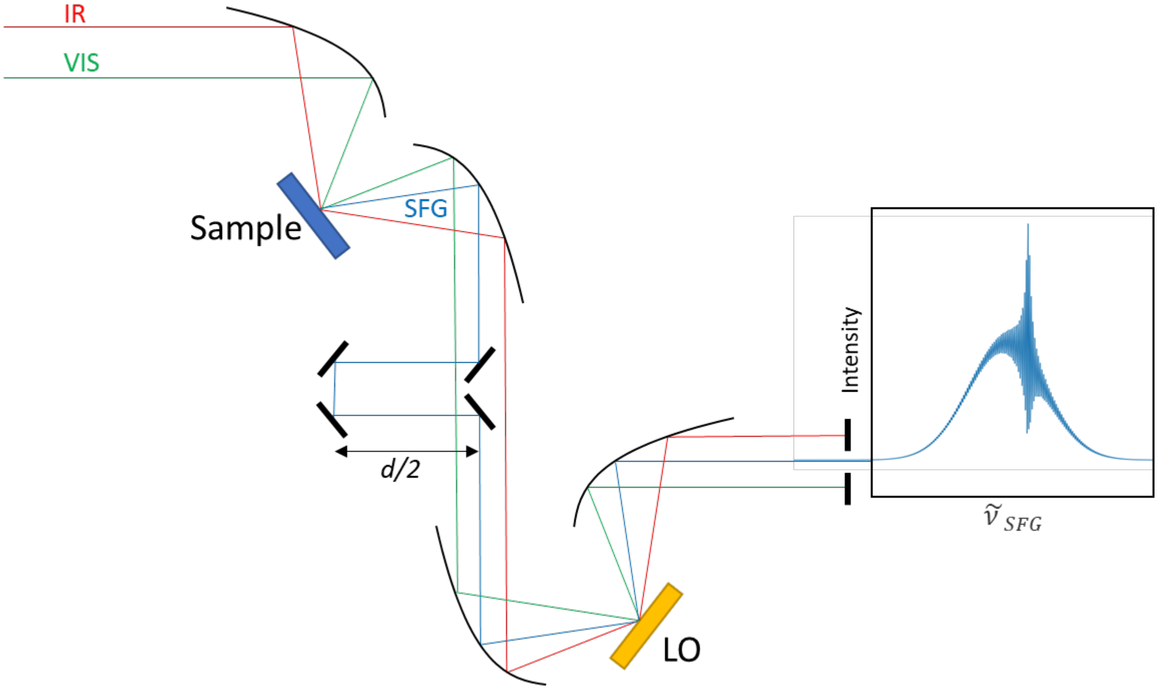

Figure A.1. Diagram of a typical spectral-interferometric PS-SFG setup. IR and VIS beams are focused on the sample by a parabolic mirror to produce SFG which is then collimated (along with the IR and VIS beams) by a second parabolic mirror. An optical path length of d is added exclusively to the SFG beam by an optical delay line. All beams are then focused onto the LO to produce a second source of SFG which interferes with the SFG produced from the sample, producing a spectral interferogram as shown.

In Figure A.1, the additional optical path length *d* added to the SFG produced by the sample results in a phase difference between the sample and LO signal given by

$$\Delta\varphi(\tilde{\nu}_{SFG}) = 2\pi\, d\, \tilde{\nu}_{SFG} + \varphi_{Sample}(\tilde{\nu}_{SFG}) \,, \tag{A.1}$$

where $\tilde{\nu}_{SFG}$ is the SFG wavenumber and $\varphi_{Sample}(\tilde{\nu}_{SFG})$ is the original phase of the sample signal. To demonstrate how $\varphi_{Sample}(\tilde{\nu}_{SFG})$ can be extracted from a spectral interferogram, a spectral interferogram produced by the setup shown in Figure A.1 was simulated and is shown in Figure A.2.

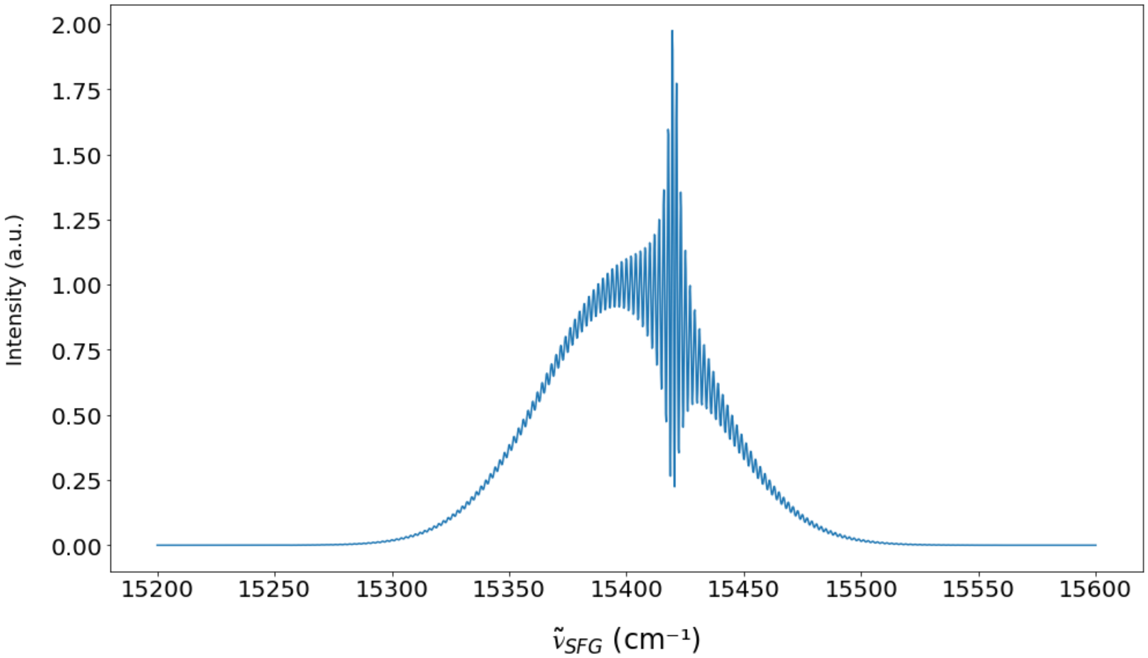

Figure A.2. Simulated spectral interferogram with *d* = 0.5 cm.

In order to extract the original phase of the sample signal $\varphi_{Sample}(\tilde{\nu}_{SFG})$, the interferogram must be separated into its two components:

$$I_{PI}(\tilde{\nu}_{SFG}) = |E_{LO}(\tilde{\nu}_{SFG})|^2 + |E_{Sample}(\tilde{\nu}_{SFG})|^2 , \tag{A.2}$$

$$I_{PD}(\tilde{\nu}_{SFG}) = 2|E_{LO}(\tilde{\nu}_{SFG})||E_{Sample}(\tilde{\nu}_{SFG})| \cos\left(2\pi\, d\, \tilde{\nu}_{SFG} + \varphi_{Sample}(\tilde{\nu}_{SFG})\right) , \tag{A.3}$$

where $I_{PI}(\tilde{\nu}_{SFG})$ is the phase-independent component and $I_{PD}(\tilde{\nu}_{SFG})$ is the phase-dependent component. $I_{PD}(\tilde{\nu}_{SFG})$ is expected to be oscillating with a frequency of *d* in the interferogram, while $I_{PI}(\tilde{\nu}_{SFG})$ is not. In order for spectral interferometry to be effective, a large enough *d* should be used so that 1/*d* is smaller than the width of the underlying spectral features of the sample signal. With this requirement satisfied, $I_{PI}(\tilde{\nu}_{SFG})$ can be taken as the low-frequency component and $I_{PD}(\tilde{\nu}_{SFG})$ can be taken as the remaining high-frequency component of the interferogram. Although this is the method used in literature, the means of separating the two components presented in literature uses an FFT of the interferogram and separates the two components in the inverse (time or distance) domain, and then IFFTs back into the original (frequency or wavenumber) domain.[34,35]

It is believed that the methods presented in literature can be a source of confusion, to alleviate this, a new method of extracting the $I_{PI}(\widetilde{\nu}_{SFG})$ component is presented here. The method is to apply a lowpass filter, such as a Gaussian filter, directly to the interferogram that sufficiently attenuates oscillations with frequency *d* while minimally attenuating the spectral features of the underlying signal. The $I_{PD}(\widetilde{\nu}_{SFG})$ component can be extracted by subtracting the $I_{PI}(\widetilde{\nu}_{SFG})$ filtered component from the original interferogram. This method does not require an FFT and results in two components that are completely real, which is consistent with the equations presented above. The results of this method applied to the interferogram in Figure A.2 are shown in Figure A.3. The FFTs of the extracted components are shown in Figure A.4 to demonstrate the effect of this method in the inverse domain.

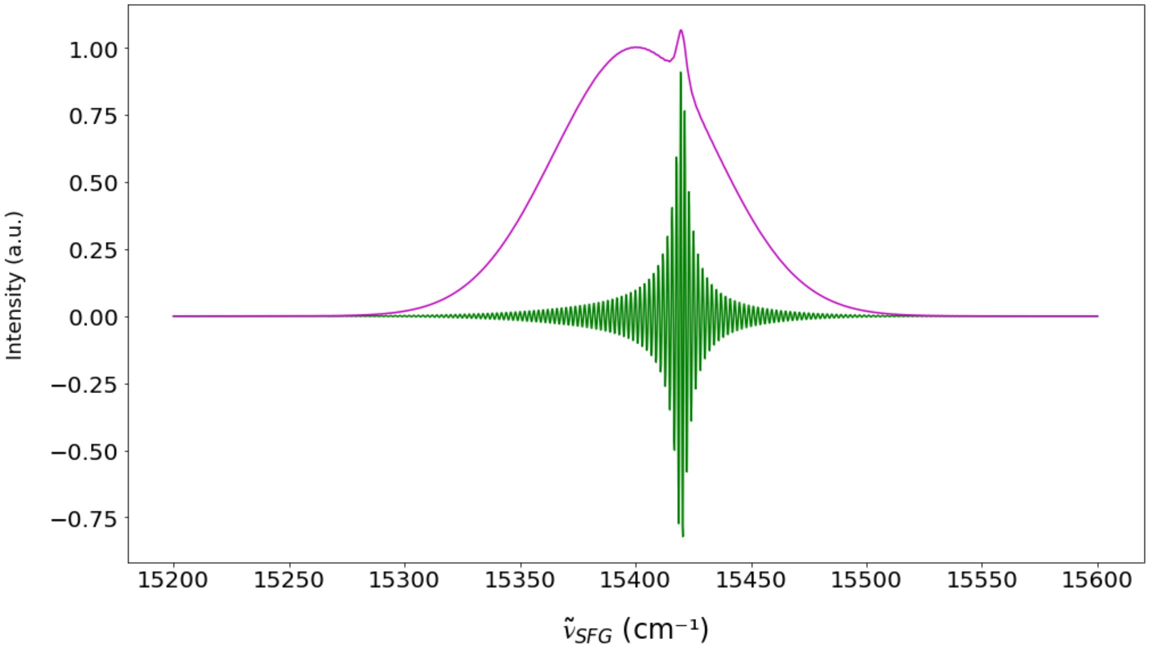

Figure A.3. $I_{PI}(\widetilde{\nu}_{SFG})$ (magenta) and $I_{PD}(\widetilde{\nu}_{SFG})$ (green) components of interferogram shown in Figure A.2. I_{PI} was extracted by applying a Gaussian filter with $\sigma = 1/(2d) = 1$ cm^{-1} to the original interferogram. $I_{PD}(\widetilde{\nu}_{SFG})$ was extracted by subtracting $I_{PI}(\widetilde{\nu}_{SFG})$ from the original interferogram.

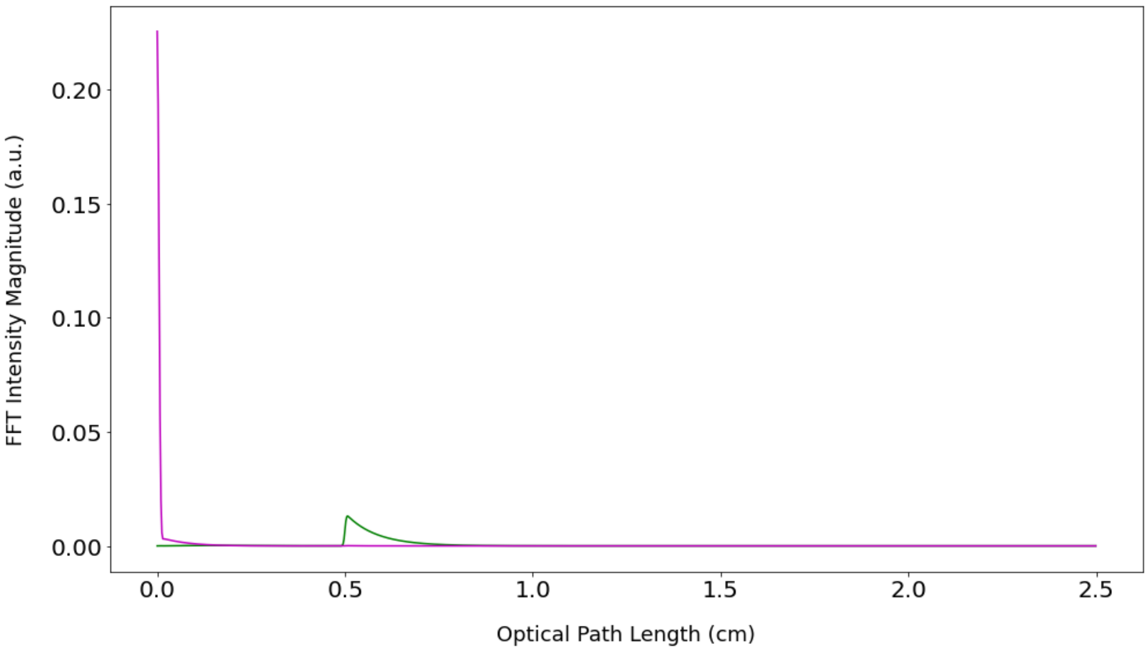

Figure A.4. FFT magnitude of the two components $I_{PI}(\widetilde{\nu}_{SFG})$ (magenta) and $I_{PD}(\widetilde{\nu}_{SFG})$ (green) shown in Figure A.3.

With $I_{PD}(\widetilde{\nu}_{SFG})$ extracted, it becomes possible to calculate $2|E_{LO}(\widetilde{\nu}_{SFG})||E_{Sample}(\widetilde{\nu}_{SFG})|$ and $\varphi_{Sample}(\widetilde{\nu}_{SFG})$ using

$$I_{PD}'(\widetilde{\nu}_{SFG}) \approx \frac{\Delta I_{PD}(\widetilde{\nu}_{SFG})}{\Delta \widetilde{\nu}_{SFG}} \ , \tag{A.4}$$

$$2|E_{LO}(\widetilde{\nu}_{SFG})||E_{Sample}(\widetilde{\nu}_{SFG})| = \frac{\sqrt{4\pi^2\ d\ I_{PD}(\widetilde{\nu}_{SFG})^2 + \left(I_{PD}'(\widetilde{\nu}_{SFG})\right)^2}}{2\pi\ d} \ , \tag{A.5}$$

$$\varphi_{Sample}(\widetilde{\nu}_{SFG}) = atan2^{§}\left(-I_{PD}'(\widetilde{\nu}_{SFG}),\ 2\pi\ d\ I_{PD}(\widetilde{\nu}_{SFG})\right) - 2\pi\ d\ \widetilde{\nu}_{SFG} \ , \tag{A.6}$$

where $I_{PD}'(\widetilde{\nu}_{SFG})$ is approximated by taking the average rate of change of $I_{PD}(\widetilde{\nu}_{SFG})$ with respect to $\widetilde{\nu}_{SFG}$ between the two neighboring data points. Values calculated with these equations are plotted in Figure A.5 and Figure A.6.

[§] $atan2(y, x)$ is the angle measured between the positive x-axis and the line passing through the origin and point (x, y) in the cartesian plane. It is equal to $arctan(y/x)$ when $x>0$.

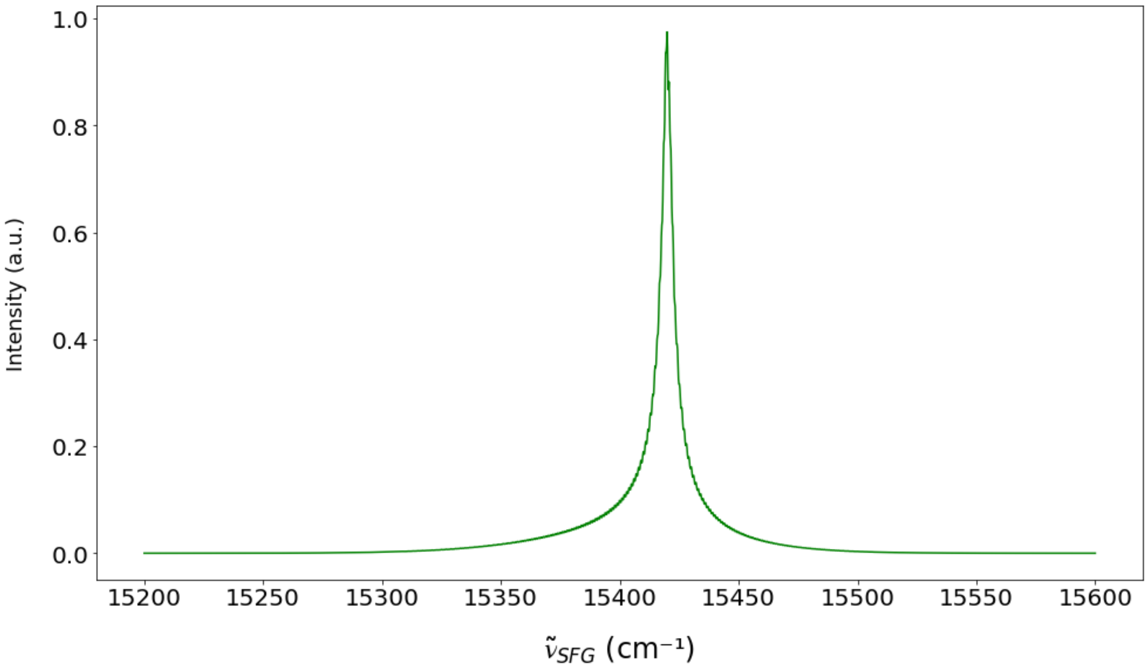

Figure A.5. $2\left|E_{LO}\left(\widetilde{\nu}_{SFG}\right)\right|\left|E_{Sample}\left(\widetilde{\nu}_{SFG}\right)\right|$ calculated from $I_{PD}\left(\widetilde{\nu}_{SFG}\right)$ plotted in Figure A.3.

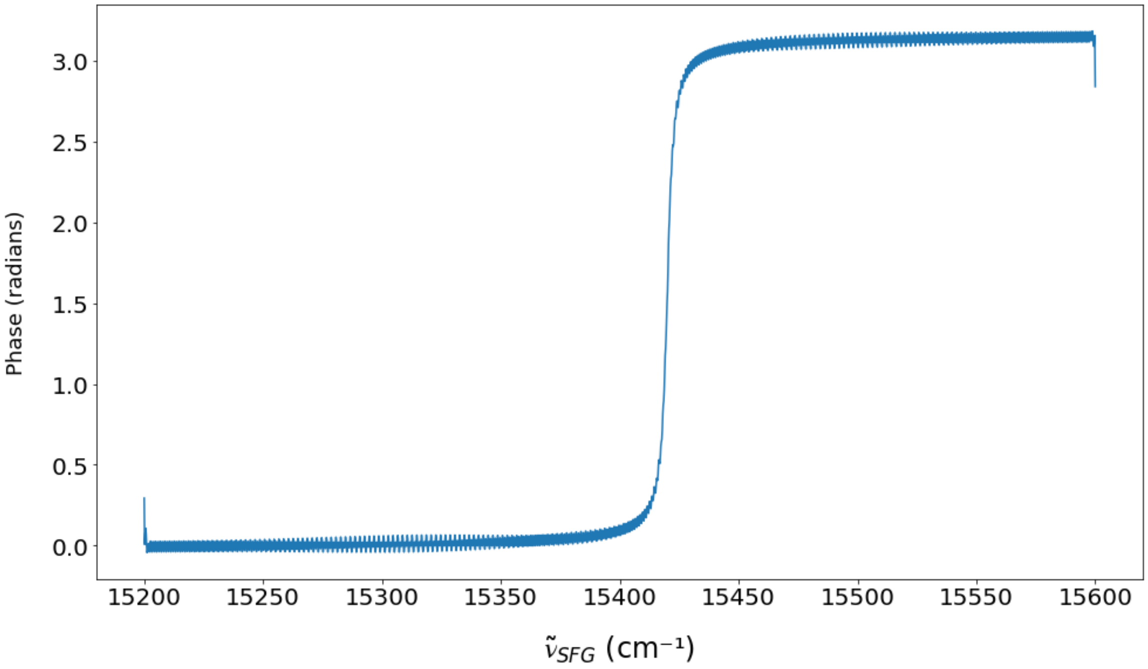

Figure A.6. $\varphi_{Sample}\left(\widetilde{\nu}_{SFG}\right)$ calculated from $I_{PD}\left(\widetilde{\nu}_{SFG}\right)$ shown in Figure A.3.

The term $\left|E_{Sample}(\tilde{\nu}_{SFG})\right|$ can be solved for algebraically or numerically from $2\left|E_{LO}(\tilde{\nu}_{SFG})\right|\left|E_{Sample}(\tilde{\nu}_{SFG})\right|$ and $I_{PI}(\tilde{\nu}_{SFG})$ assuming $\left|E_{Sample}(\tilde{\nu}_{SFG})\right|$ is smaller than $\left|E_{LO}(\tilde{\nu}_{SFG})\right|$, which can be verified experimentally. The complex amplitude of the sample signal can then be given by

$$E_{Sample}(\tilde{\nu}_{SFG}) = \left|E_{Sample}(\tilde{\nu}_{SFG})\right| e^{i\varphi_{Sample}(\tilde{\nu}_{SFG})}. \tag{A.7}$$

The resulting $E_{Sample}(\tilde{\nu}_{SFG})$ extracted from the interferogram in Figure A.2 is shown in Figure A.7, as well as the known $E_{Sample}(\tilde{\nu}_{SFG})$ that was used to prepare the interferogram. The difference between the extracted spectrum and known spectrum is shown in Figure A.8. The difference can be primarily attributed to the additional optical path length *d* not being large enough to allow for accurate separation of I_{PI} and I_{PD}, as well as the spacing between $\tilde{\nu}_{SFG}$ samples being too large which reduces the accuracy of the calculated $I_{PD}'(\tilde{\nu}_{SFG})$. As *d* becomes large, the spacing between $\tilde{\nu}_{SFG}$ samples becomes even more limiting. In practice an ideal *d* has to be found for a given spacing between $\tilde{\nu}_{SFG}$ values to minimize measurement error.

Since the sample signal is extracted using the change in intensity as a function of $\tilde{\nu}_{SFG}$, there is an inherent loss of resolution in spectral-interferometric PS-SFG measurements when compared with the resolution that the interferogram was acquired with. This, and the measurement error discussed above, are the primary drawbacks of taking spectral-interferometric measurements as opposed to phase-shifting measurements.

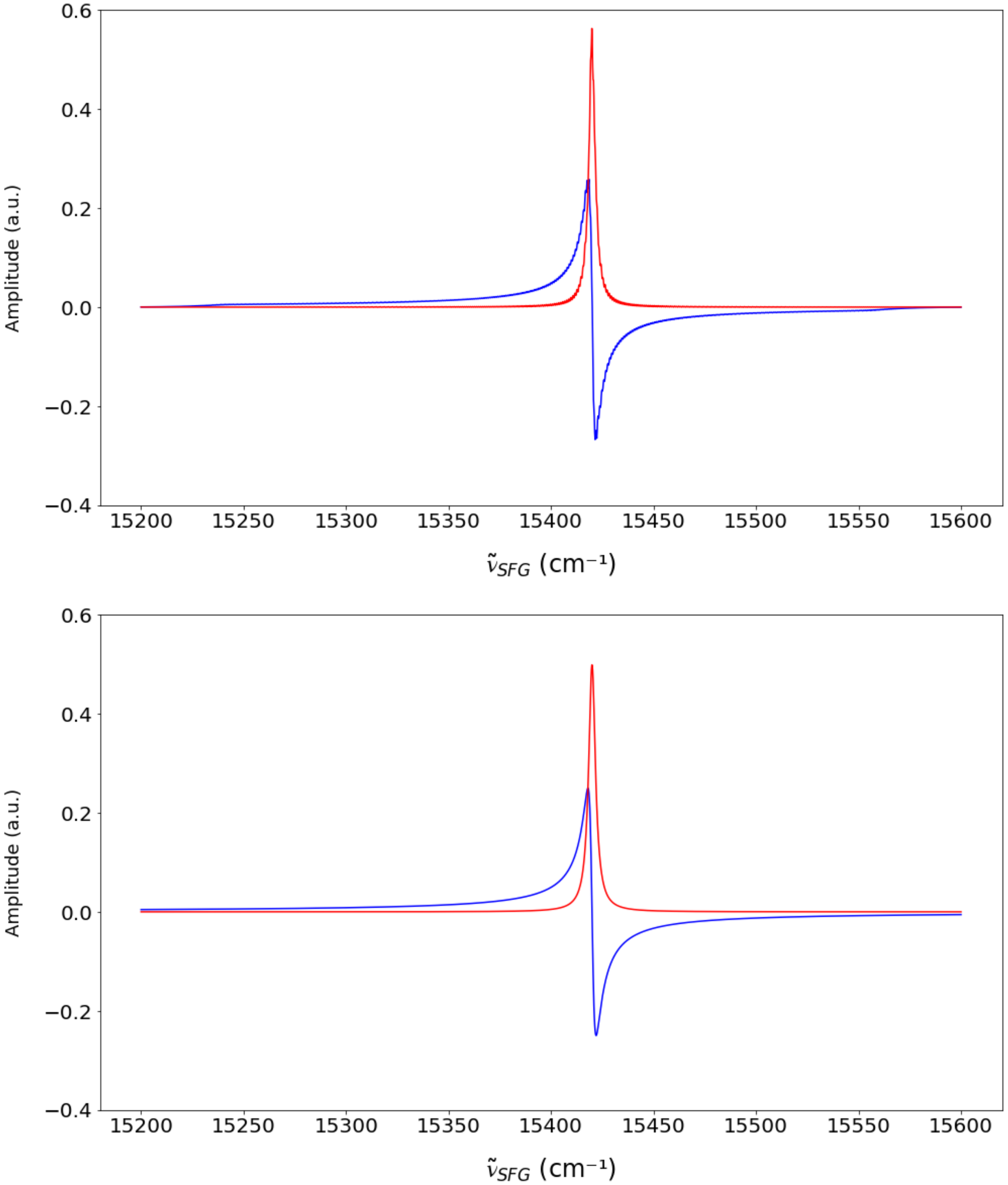

Figure A.7. Extracted complex field amplitude of the SFG produced by the sample extracted from the interferogram in Figure A.2 (top). Known values used to produce the interferogram in Figure A.2 (bottom). Real and imaginary components are plotted in blue and red respectively.

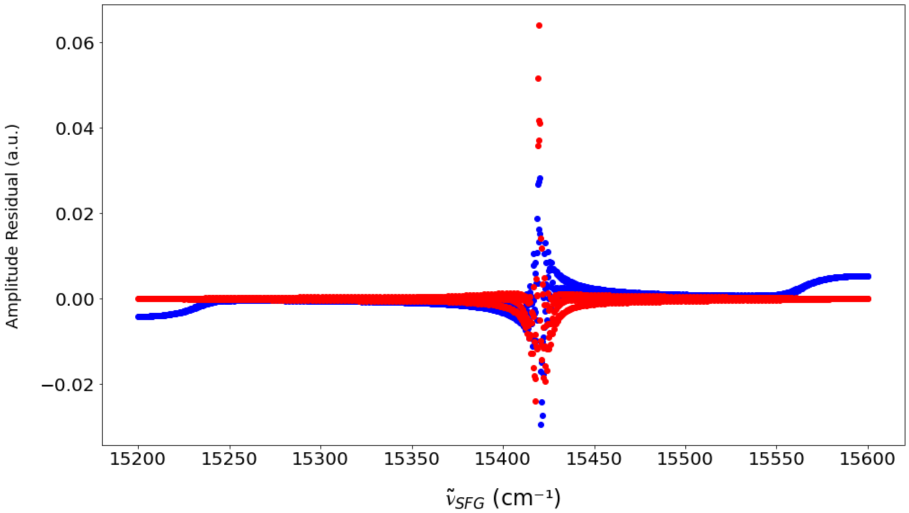

Figure A.8. Difference in the extracted values of $E_{Sample}(\tilde{\nu}_{SFG})$ and the known values used to produce the interferogram in Figure A.2. Real and imaginary components are plotted in blue and red respectively.

The layout in Figure A.1 was chosen specifically because it does not contain dispersive optics, which simplifies extraction of the sample signal. In practice, however, it is not practical to insert an optical delay line in the beam path of the SFG signal alone. In most cases, a dispersive optic is added to the beam path in order to create the additional optical path length *d*. The consequence of this is that there is now a different effective *d* for each $\tilde{\nu}_{SFG}$ due to dispersion. In cases where the dispersion is significant, it is desirable to use a reference in place of the sample and determine $d(\tilde{\nu}_{SFG})$ experimentally. The reference signal can also be used to find the phase offset caused by other dispersive elements in the beam path, including air, so that it can later be subtracted from the phase of the extracted sample signal.

In cases where the IR and VIS beams are collinear, it is impossible to add additional optical path length to the SFG beam alone. It has been demonstrated in literature that a dispersive optic can be placed in the beam path of all the beams, where an effective additional optical path length is created from the dispersion alone.[36] This does however lead to unsatisfactory results due to the dispersive optic delaying the IR and VIS pulses differentially, causing them to no longer overlap in time, preventing SFG from being produced by the second source. The implementation presented in literature used a thin dispersive element to circumvent this, which resulted in a small effective additional optical path length and a low-resolution measurement.

Appendix B: Math Functions

All FFTs presented in this thesis were calculated in Python using the NumPy library.[37] Since all input values were real, the function “numpy.fft.rfft”[38] was used, which does not compute the negative frequency terms as they are redundant when the input is real. The normalization mode used was “forward,” which produces an FFT magnitude that is consistent with the apparent amplitude of the oscillations in the signal for a given frequency. The frequency axis of the FFTs were calculated using the function “numpy.fft.rfftfreq,”[39] which takes the length and sample spacing of the FFT input data, and returns frequencies which are consistent with the FFT function used.

The cross-correlation shown in Figure 3.28 was calculated using the function “numpy.correlate.”[40] This function calculates the correlation defined by

$$c_k = \sum_n a_{n+k}\, b_n^* \ , \tag{B.1}$$

where a_n and b_n are the input sequences. Although this definition uses the complex conjugate of the second sequence b_n^*, this is inconsequential to the cross-correlation presented in this thesis, as both input sequences were real-valued.

Appendix C: Additional Information on SFG

As explained in the introduction, SFG can be resonantly-enhanced by having vibration excitations with the same energy of photons used to generate SFG. This process is illustrated in Figure C.1.

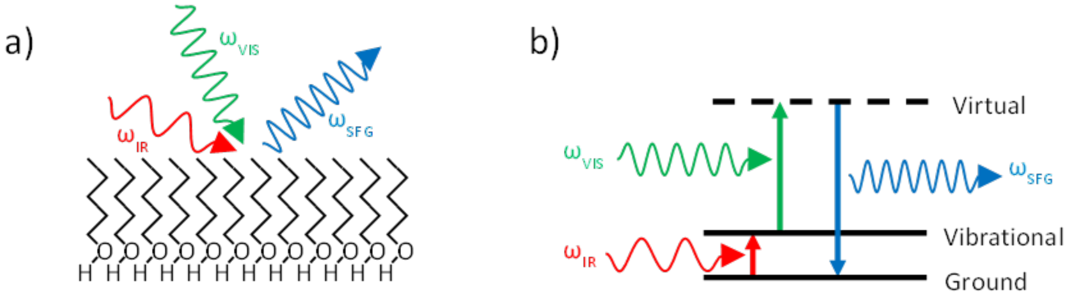

Figure C.1. Illustration of IR and visible (VIS) fields incident on monolayer of 1-pentanol producing a reflected SFG field. b) Corresponding energy level diagram for vibrationally-enhanced SFG when ω_{IR} matches the resonant frequency of a vibrational mode. The SFG field satisfies the condition $\omega_{SFG} = \omega_{IR} + \omega_{VIS}$.

The monolayer of 1-pentanol shown in Figure C.1 would be expected to produce a significant amount of SFG due to all of the molecules having the same orientation. The phase of the SFG field produced from the molecules is dependent on their orientation. If molecules were to have alternating orientations, and hence alternating phases, the SFG produced from molecules in one orientation would cancel with the SFG produced from molecules orientated in the opposite direction. In such cases, it is still possible to produce a net SFG signal from the molecules due to the symmetry breaking nature of interfaces. If molecules orientated one way had their head group exposed to an interface distinct from those in the opposite orientation (e.g., gold substrate vs. air), they could still produce net SFG due to the different interfaces influencing the molecules differently, whether they cause a frequency shift or simply a change in SFG intensity.

The use of resonant enhancement is not limited only to resonances with vibrational modes. It is possible to produce SFG that is resonantly-enhanced simultaneously by vibrational excitations with the IR pulse and electronic excitation with the visible pulse. This is illustrated in Figure C.2. This has been demonstrated in literature as a means to further study the resonances at interfaces.[41]

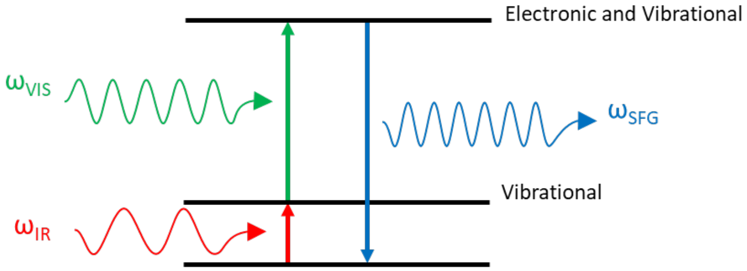

Figure C.2 Energy level diagram for doubly-resonant SFG when ω_{IR} matches the resonant frequency of a vibrational mode and ω_{VIS} matches the resonant frequency of an electronic excitation.

In contrast to the highest energy state in Figure C.1, the highest energy state in Figure C.2 is real as opposed to virtual. The real state is expected to have a significantly longer lifetime due to it being associated to an actually eigenstate of the molecule, allowing the molecule store the energy as an electronic and vibrational excitation. It is also expected to have a lower bandwidth for excitation than a virtual state due to the requirement of the visible light being resonant with the electronic excitation.